INFRARED CHEMICAL IMAGING OF GERMINATED WHEAT: EARLY NONDESTRUCTIVE DETECTION AND MICROSPECTROSCOPIC IMAGING OF KERNEL THIN CROSS SECTIONS *IN SITU*

by

HICRAN KOC

B.S., Istanbul Technical University, 2004

A THESIS

submitted in partial fulfillment of the requirements for the degree

MASTER OF SCIENCE

Department of Grain Science and Industry
College of Agriculture

KANSAS STATE UNIVERSITY
Manhattan, Kansas

2007

Approved:

Major Professor
David L. Wetzel

Abstract

During germination, biochemical changes occur in the wheat kernel by stimulation of enzymes and hormones, and the seed reserves are mobilized. Infrared microspectroscopy and imaging enables a localized chemical inventory, upon germination, to study the process. Frozen sections of germinated wheat mounted onto BaF_2 were mapped to produce functional group images for comparison with corresponding sections of ungerminated kernels. Relative functional group populations in the scutellum and embryonic axis were assessed before and after germination. An average 23% reduction in lipid to protein ratio was observed in the scutellum based on the comparison of 53,733 spectra. As a result of the early germination process, lipid in the scutellum was depleted to provide energy for the growing embryo.

Germination of the kernels while in the field before harvest due to high humidity is known as preharvest sprouting. Preharvest sprouting has detrimental effects on the end use quality of the wheat (sprout damage) and cause economic loses. Tolerance to preharvest sprouting is highly desirable. To assist breeding program, a nondestructive near-IR chemical imaging method has been developed to test new lines for resistance to preharvest sprouting. The higher sensitivity of subsurface chemical imaging, compared with visual detection, alpha amylase determination, or viscosity testing, permits germination detection at early stages. A near-IR chemical imaging system with an InGaAs focal plane array (FPA) detector in the 1100 nm-1700 nm range was used. Kernels from six different cultivars, including HRW and HWW wheat, were exposed to moist conditions for 6, 12, 24, 36, and 48 hours. Images of each 90 kernel group were examined; kernels exposed to moisture for 36 hours were compared with kernels treated for 3 hours as a control. Each kernel was classified as sprouted or not sprouted with the criteria of log 1/R intensity at select wavelengths or select factors of principle component analysis (PCA) treatment of reflectance intensity data. Imaging wavelength range was expanded beyond 1700 nm to 2400 nm with the use of InSb FPA. Study for the potential for unsupervised determination in nondestructive near-IR imaging with detection wavelengths 1200-2400 is ongoing. Some preliminary results presented are encouraging.

Table of Contents

List of Figures

List of Tables

Acknowledgements

First of all, I would like to thank my major professor David L. Wetzel for his valuable support and guidance in my research, education and experiences. I am thankful to him for the exposure he provided me regarding my academic career; I had many oral presentations in important conferences and had two publications which are important success for a MS student, and I had a chance to work in National Brookhaven Laboratory which is really unique to me. In addition to these, I can never forget Connie and David Wetzel's unlimited help while very far away from my family. They always treated me as a daughter, thank you Connie and Dr. Wetzel.

Without my committee member Virgil Smail none of these achievements could be possible. I would like to thank Dr. Smail for this support to our lab and research. I want to convey my thanks to Dr. Culberston for being my committee member.

Dear my parents, sisters, brother and my friends! I feel so lucky, you make my life meaningful. Thank you my parents Nekariye and Orhan Koc, my lovely sisters and best friends Umran and Kubra, my dear brother Gokhan. I would like to thank my friends from my home country Asli, Aysegul, Sema, Sevil and Bilgin for sharing the life including all aspects. I want to say thank you my good friends Maggie, Sreeram, Val, Ramakanth and Sibel whom I met in Manhattan, they all became a part of my life being sisters and brothers to me. And Dr. Dogan and her family always made me feel myself a member of them and remind me warmness, sincerity, happiness I had in my family. Thank you! Hulya, Huseyin and Duru Dogan. My lab mate Emily, thank you for being a partner in the lab for two years sharing all challenges and good time, and exposing me to your culture. I also thank our new member in the lab, Lauren for her help.

Dedication

I dedicated this work to my parents; my mother NEKARIYE KOC and my father ORHAN KOC for teaching me the importance of two values in the life, *honesty* and *education* which built my character and determined my way in the life and thank you for being with me, being behind me all the time wherever I am, whatever I am doing. Even tough you disagreed with my decisions many times, and I did not listen to you most of the time, you supported me without any expectations, without any limitations. You dedicated your life to me, and I hope I can do good things for you and for the community. I am so thankful to God that I am your daughter, you are just perfect….

PART 1 - MICROSPECTROSCOPIC IMAGING OF KERNEL THIN CROSS SECTIONS *IN SITU*: INVESTIGATION OF BIOCHEMICAL CHANGES IN WHEAT KERNELS DURING SPROUTING BY FT-IR

1. Introduction

1.1 The Wheat Kernel

Wheat is a member of the grass family, Gramineae, and the genus Triticum and a dry one seeded fruit (1). The wheat kernel, surrounded by the lemma and palea, is produced in the spikes at the top of the stems. The glume encloses the each spikelet. These parts of the plant; lemma, palea, and glume are called chaff. The wheat is threshed by separating the grains from the chaff mechanically (2).

Wheats are classified in different ways based on factors such as winter or spring habit of growth, time needed to mature, height, stem, spike, glume, and kernel characteristics (endosperm hardness, color). There are white or red wheat cultivars. The pigments of the seed coat are primarily responsible for the dark color of the red wheat. Moreover the color of the kernel can be affected by the endosperm texture and the vitreousness and transparency of the pericarp (3). Chromosomes are the primary control factor for the characteristics in the wheat. Common wheat has 21 chromosome pairs. Plant breeders develop wheat varieties with desired characteristics for special purposes (2).

1.1.2. Structure and Composition of the Wheat Kernel

The wheat kernels are from 8-10 mm in length. The dorsal side of the kernel is round and at the ventral side (opposite the germ) kernel has a longitudinal crease running almost entire length of the kernel (4).The structure of the wheat kernel is shown in figure 1.1 and it is

composed of three main parts including the endosperm, the bran with various protective skin and the germ.

Figure 1.1 Longitudinal and cross section of a wheat kernel showing different botanical parts; endosperm, bran and germ (reprinted from ref.1).

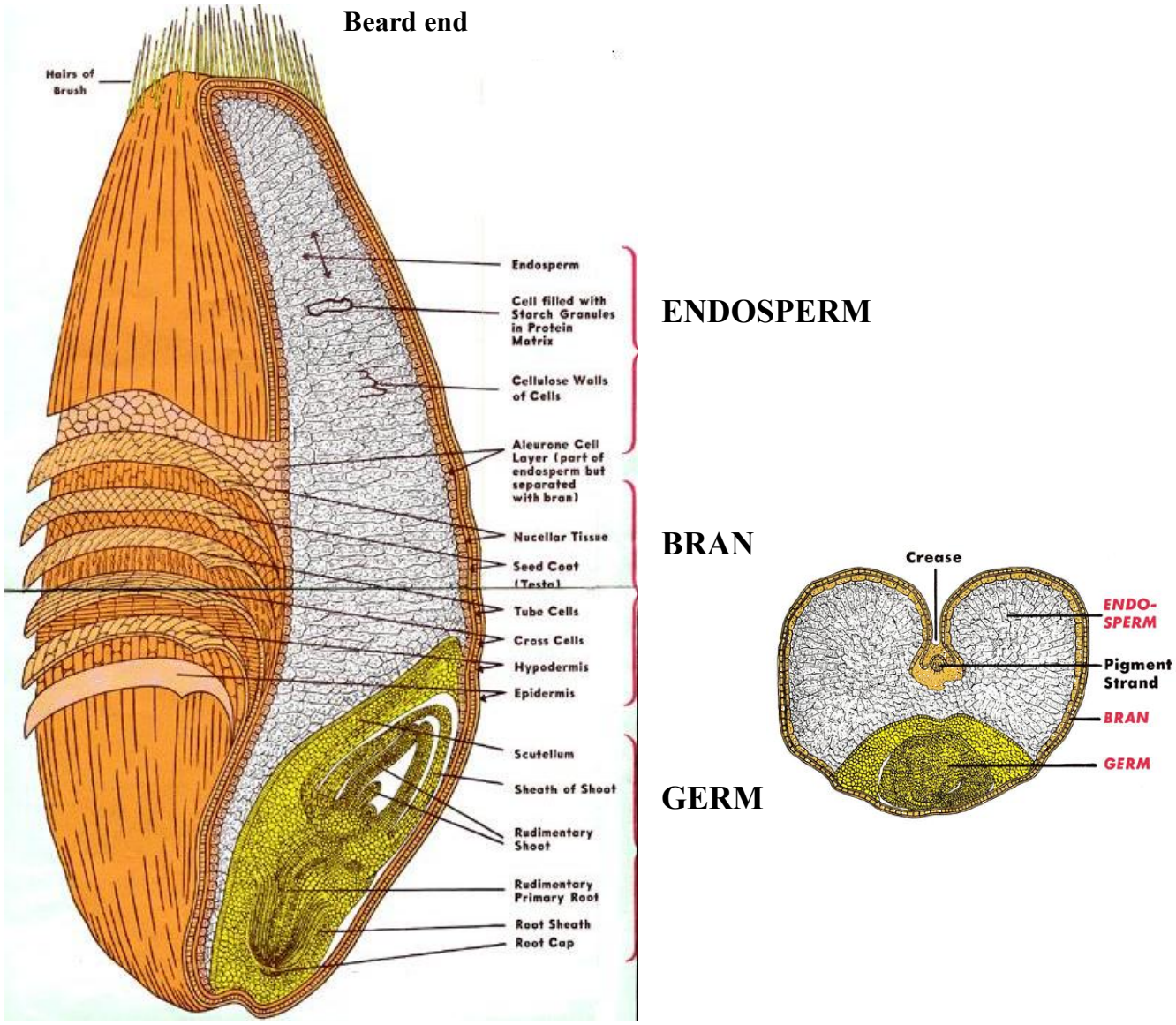

1.1.2.1. Endosperm

Endosperm, the food bag of the wheat grain, consists of starchy endosperm and the aleurone layer. The aleuorone layer is botanically outermost part of the endosperm, but during milling it is removed to form bran. Starchy endosperm yields flour during milling.

There are three types of cells in starchy endosperm; peripheral, prismatic, and central. The cells vary in size, shape, and composition of the starch granules and proteins depending on their location within the kernel. The cells have starch granules embedded in a protein matrix, mostly gluten (storage proteins) (1).There is less protein in the center with increasing levels thorough the bran coat (3).

The cell walls of endosperm contain pentosans, other hemicelluloses and beta-glucan. Depending on the variety, endosperm texture can be soft or hard. Hard wheat endosperm starch granules retain their shape during milling, whereas soft wheat endosperm starch granules fracture across the cells. The reason for this difference is that starch granules are less tightly adhered to the protein matrix in soft endosperm compared to hard wheat endosperm (1, 2). In addition to variation in hardness of wheat endosperm individual kernels can differ in vitreousness.

1.1.2.2. Bran

The bran consists of outer protective layers of the grain; pericarp (outer coating), seed coat (inner coating) and the adjacent layer aleurone. The pericarp encircles the seed and consists of several layers. The outer pericarp is composed of epidermis, hypodermis, and remnants of thin-walled cells (from the outside toward the center of the kernel) while the inner pericarp is composed of intermediate cells, cross cells, and tube cells. The total pericarp represent 5% of the kernel and consists of 6% protein, 2% minerals, 20% cellulose, 0.5% lipid, and the remaining part is nonstarch polysaccharides (1).

Underneath the pericarp, there is inner coating of the seed, seed coat, which is composed of testa (episperm), the pigment strand for the colored wheats, and the nucellar layers. The pericarp and seed coat are separated during flour milling; the adjacent aleurone layer also forms the bran although it is a part of endosperm. A one cell thick aleurone layer covers starch endosperm and germ. The composition of aleurone layer includes minerals, protein, phosphorus compounds, lipid, and niacin. In addition, it is rich in thiamin, riboflavin, and has high enzyme activity (1, 4).

All parts of the bran represent 14.5% of the whole wheat. The distribution is epidermis 3.9%, cross cell layers 0.9%, testa 0.6%, nucellar layers, and aleurone 9.0% (3).

1.1.2.3. Germ

The germ, which accounts for 2.5-3.5% of the kernel, is the reproductive organ. In figure 1.2 the structure of the germ is shown, it contains two major parts; embryonic axis and scutellum. An epithelial layer separates the wheat germ from the endosperm. During germination the embryonic axis develops as the beginning of a new seed and the scutellum provides nourishment. The embryonic axis is composed of the shoot (plumule) and the primary root. The shoot is oriented toward the brush end of the kernel and is covered by the coleoptile protective sheath. Whereas, the primary root is directed toward the base. The coleorhiza covers and protects it (3).

The germ is high in protein (25%). The embryonic axis contains 16% lipid and the scutellum 32%. In addition to lipid and protein, it has simple sugars (18%) mainly sucrose and raffinose. Its mineral content is 5%, and it is also rich in B vitamins, vitamin E, and enzymes (1, 4). The greatest part of the scutellum is parenchyma cell which contain lipid and protein.

Figure1.2 Structure of the germ of the wheat kernel, longitudinal and transverse sections showing different parts of the germ, the letters corresponding to each part are given (reprinted from ref. 2).

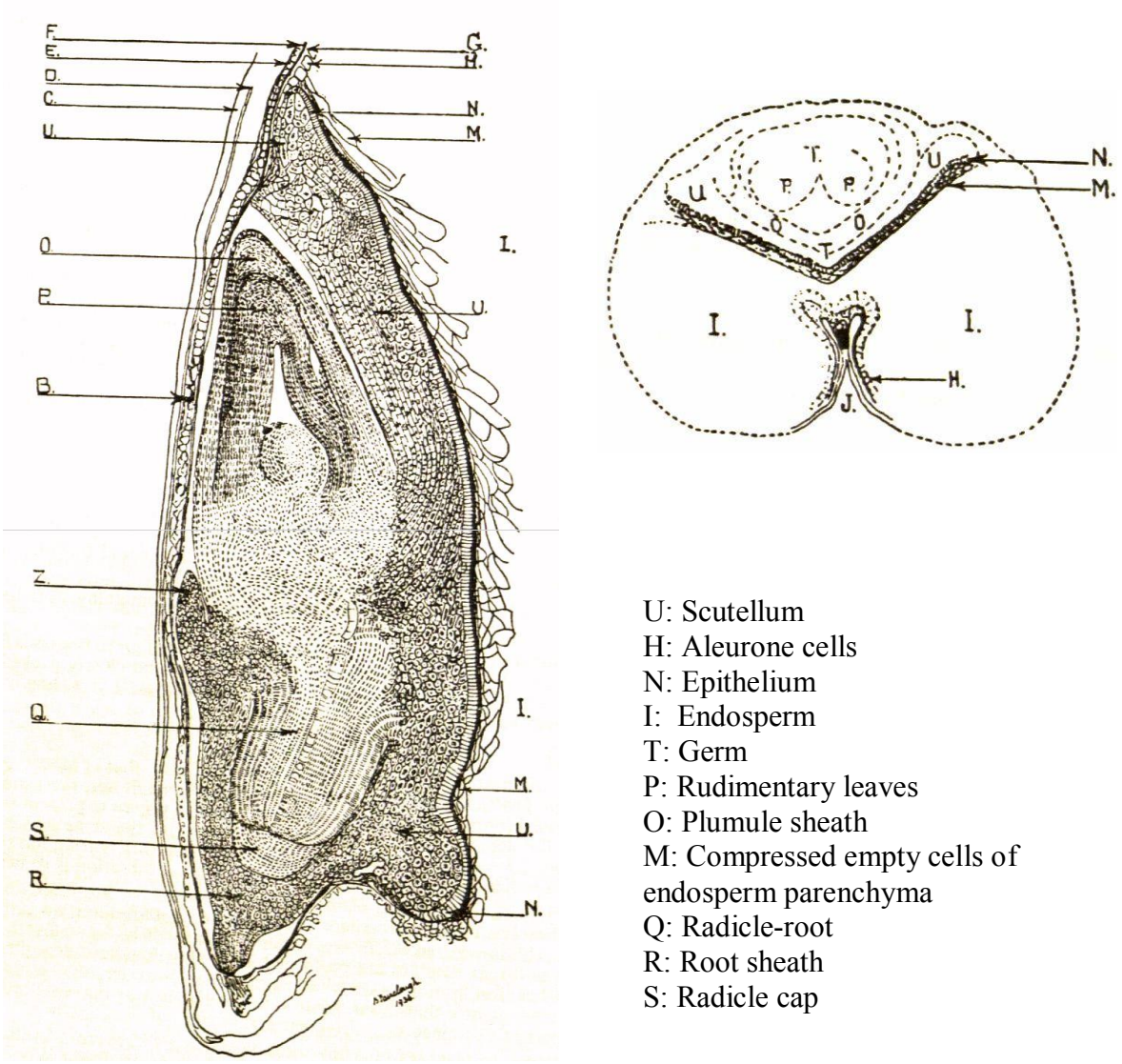

U: Scutellum
H: Aleurone cells
N: Epithelium
I: Endosperm
T: Germ
P: Rudimentary leaves
O: Plumule sheath
M: Compressed empty cells of endosperm parenchyma
Q: Radicle-root
R: Root sheath
S: Radicle cap

1.1.2.4. Brush (Beard) and Crease

The brush is a cluster of hairs located at the opposite end of the germ. The crease is an indent on the central side or the opposite side from the dorsal side of the kernel (2).

The distribution of different parts of the kernel is shown in the figure 1.3. Distribution of the protein within the kernel is 72% endosperm, 4.5% scutellum, 3.5% embryo, 15% aleurone layer, 4% pericarp & testa (4).

Figure 1.3 Distribution of different parts of the kernel (84 % endosperm, 13.5 % bran, and 2.5 % germ) (5).

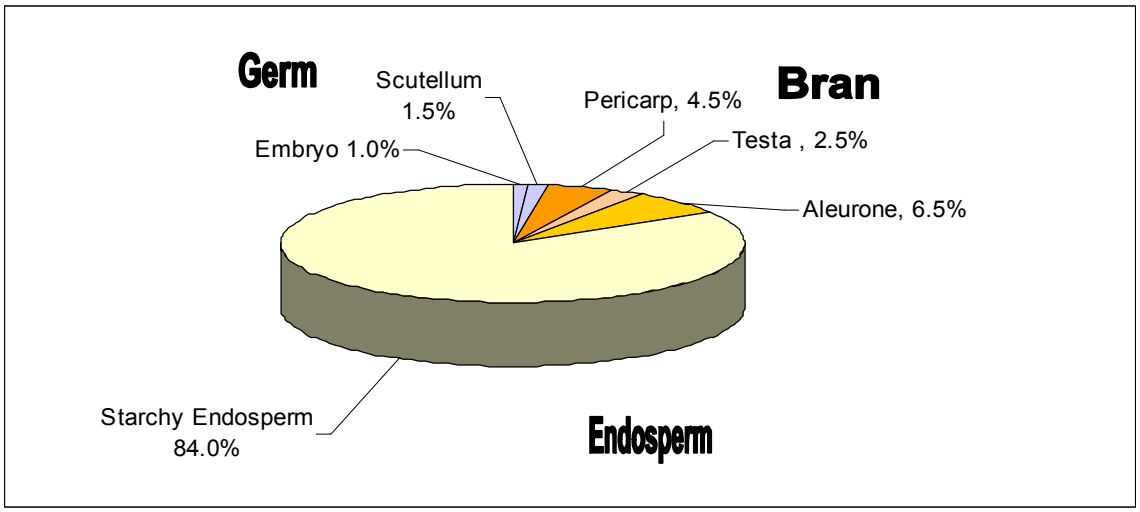

1.2. Germination and Preharvest Sprouting of Wheat

1.2.1. Introduction

The mature, dormant, air dried wheat kernel has a 9-12% moisture content, and it has low metabolic activity at these conditions. Exposure to moisture triggers germination. The three living tissues (embryo, scutellum and aleurone layer) play important roles during germination. In this process, the kernel is hydrated rapidly, enzymes are activated, the respiration rate increases rapidly, consumption of reserve materials is started, and protrusion of the radicle from the seed coat may occur within 24 to 48 hr. This is called as germination. By the production of the shoot and roots, a new plant is produced from the grain (5, 6). Germination of the kernels while still in the ear in the field before harvest because of the unfavorable conditions such as rain and high

humidity is known as preharvest sprouting. Cereal growing regions of the world where there is high probability of rain during harvest are liable to preharvest sprouting such as Eastern Europe, Chile, Argentina, Brazil, South Africa, Australia, and Manitoba in Canada. In the US, the Pacific Northwest states are examples of places that have suffered some years from this problem (7). The changes in chemical components of the wheat kernel with the germination process have detrimental effects on the end use of the wheat and cause important economic loses to the farmers because the value for fermentation is low compared to that for milling and baking. These detrimental changes are referred to as preharvest sprout damage (8). Usefulness of wheat for bread making purposes decreases rapidly after germination due to starch degradation by α-amylase. Preharvest sprouting results from the lack of dormancy. Tolerance to preharvest sprouting and embryo dormancy are highly desirable characteristics that plant breeders study (9).

1.2.2. Stages of Germination and the Factors Affecting the Process

The events take place during germination can be divided in three phases; imbibition, lag phase, and germination. First event in the sprouting is the movement of the water through the grain. Water uptake of the kernel is rapid since the kernel is dry, and tissues reach 30-50% moisture in one or two days. Next seeds enter a lag phase, when they swell and become heavier, and metabolism becomes active. If all the environmental conditions are appropriate, the seed enters the germination phase (10). During germination, the embryo takes in materials from endosperm through the epithelial layer for its growth. Exposure to moisture activates enzymes in the germ initiating germination. Starch in the vicinity of the germ is hydrolyzed into simple sugar by amylolytic enzymes and sugar is used to nourish the germ. Beside this enzymatic activity, hormones affect germination by influencing the formation of α-amylase in the endosperm (3). During germination, the scutellum functions as a digesting and absorbing organ for the

transference of the food from the endosperm to growing embryo (4). Sequences of the events in the sprouting are shown in figure 1. 4.

Figure 1.4 Sequences of the events in the sprouting starting from moisture exposure to rupture of the seed coat (adopted from ref.11 and 12).

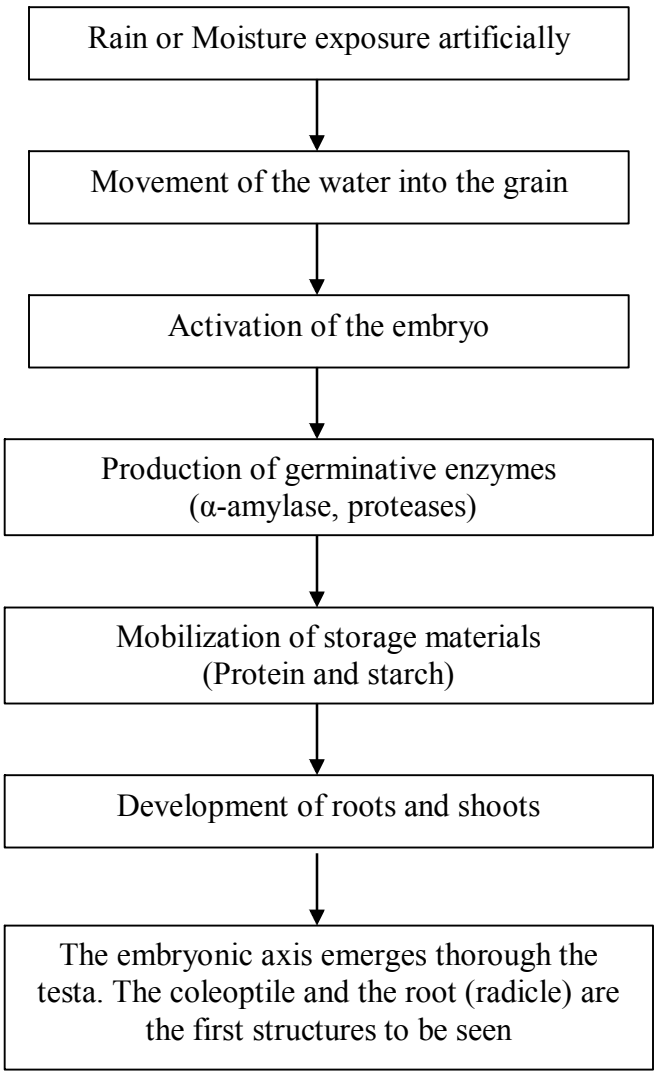

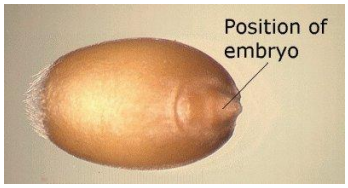

Fully imbibed grain, before embryo emerges.

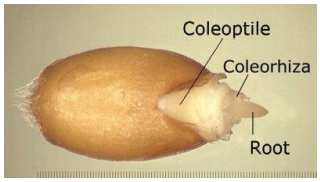

There are several factors affecting germination. These include kernel characteristics and environmental conditions such as moisture, temperature, and oxygen. Seed viability (ability to grow) and its dormancy are important for the germination process. The optimum temperature is

reportedly 20-25ºC (12a). Mares (8) reported that an optimum temperature for germinability was dependent on dormancy level of the individual varieties. The strongly dormant variety achieved germination at 10ºC. The non-dormant variety performed germination at 20ºC and the lag period varied with temperature.

1.2.3. Biochemical Changes during Sprouting

During the sprouting process, there are many changes in the molecular and cellular biology of the wheat kernel. Enzymes and hormones are stimulated and the seed reserves are regulated. In addition to these enzymatic and hormonal changes, the cytological changes are observed in the cells. The biochemical, cytological and hormonal changes during germination have been studied by Swift and O'Brien (13), Fincher (14), Bewley and Black (15,16,17), Simon (10), Ashford and Gubler (18), Corder and Henry (19), Tavener and Laidman (20,21) and Kruger (22). In this section, biochemical changes in germinated wheat associated with detrimental effects on end product quality will be discussed.

1.2.3.1. Enzymes in germinating wheat

Enzymes are the most important biochemical components that form during germination and affect the quality. There is a compartmentalization of the components in the kernel which is important for storage stability of it. The wheat kernel has degradation enzymes and substrates, but they are protected from coming into contact which provides the stability (1). The starch degrading enzyme, α-amylase, is considered to be the main enzyme. Proteolytic enzymes could also be important. The synthesis and the secretion of the enzymes that catalyze degradation of the macromolecules in starchy endosperm control the cellular activity in aleurone layer (14). The scutellar epithelium has a role in the production and secretion of the enzymes as well as absorbing the endosperm degradation products and translocation of them to the developing

embryo. Enzymes produced in the aleurone layer and scutellar epithelium can be divided into three groups: 1) enzymes involved in ongoing metabolism within the cell, 2) enzymes that mobilize reserves of scutellar and aleurone cells, and 3) enzymes synthesized *de novo* and secreted in endosperm (14, 23).

1.2.3.1.1. Carbohydrate-Degrading Enzymes

The carbohydrate-degrading enzymes in germinating wheat can be listed as α- and β-amylases, debranching enzymes, cellulases, and glucanases. Among these carbohydrases, α-amylases are known for their harmful effects in bread making process. This enzyme cleaves the α-(1→ 4) D-glucosidic bonds (Figure 1.5) in the starch components. With germination, this enzyme forms progressively, initially adjacent to the scutellum, and subsequently adjacent to the aleurone layer. More enzymes occur in the outer layers of the kernel. With severe sprouting, enzymes penetrate the endosperm. Corder and Henry (19) found that α-amylases activity was increased over the first four days of germination. MacGregor and Matsuo (24) observed that the enzyme synthesis was relatively slow up to 48 hr of germination of barley in Petri dishes. But after 48 hr, it increased rapidly.

Figure 1.5 The structure of amylase and the α-(1→ 4) D-glucosidic bonds which combines each glucose molecules in the amylase molecule (reprinted from ref. 24a).

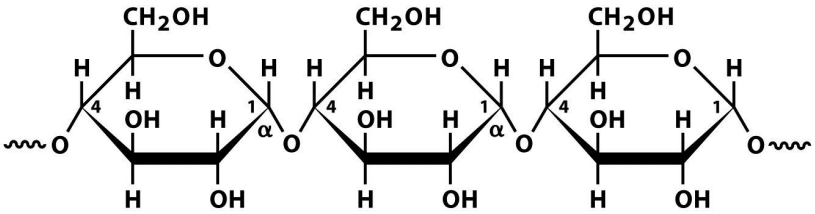

β- amylases hydrolyze the α-(1→ 4) D-glucosidic bonds from the nonreducing end of starch and yield maltose. Upon germination, the β- amylases levels increase several fold in the endosperm. Little attention is paid to debranching enzymes relative to preharvest sprouting. They cleave α-(1→ 6) D-glucosidic bonds in the amylopectin (Figure 1.6) (22, 15). Corder and Henry (19) also found some increase in other carbohydrate degrading enzymes such as glucanase, endo-xylanesse, during germination.

Figure 1.6 The structure of amylopectin and the α-(1→ 6) D-glucosidic bonds which forms branching (reprinted from ref. 24a).

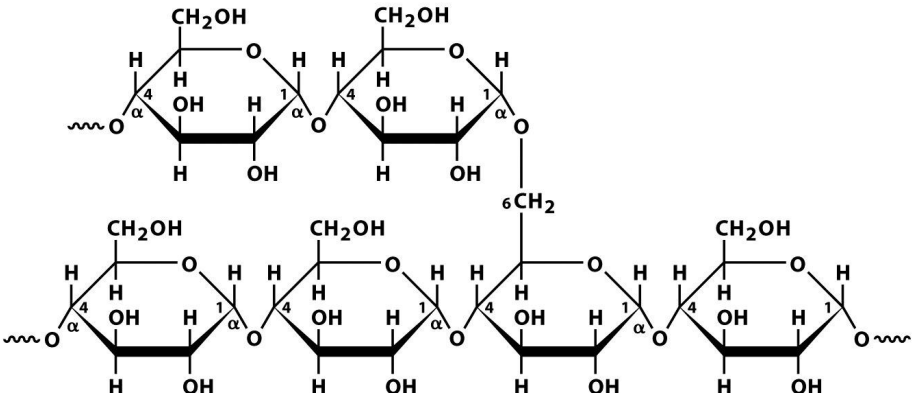

1.2.3.1.2. Protein-Degrading Enzymes

Proteolytic enzymes are of secondary importance relative to their effect on end product quality. These enzymes are very complex and difficult to purify. The main enzymes related to preharvest sprouting are acid endopeptidases and carboxypeptides. The endopeptidases are located in the pericarp, seed coat, and aleurone layer at early development, and then decrease with maturation. They are also present in the embryo and endosperm at maturity levels. In germinating kernels the level increases by the hormonally induced *de novo* synthesis. They cleave the internal peptide bonds to obtain smaller polypeptides. Carboxypeptides hydrolyze

proteins and peptides from C terminal amino acid end. Upon germination, they increase three fold and enzymes in endosperm are located largely adjacent to scutellar epithelium of the kernel (22, 14).

1.2.3.1.3. Other Enzymes Systems

There are some other enzymes that increase during germination, but their effect on quality requires elucidated via more research. Lipases are located mainly in the shoot and found to increase upon germination. Tavener and Laidman (20, 21) reported that triglyceride reserves in different tissues are mobilized and broken down progressively during germination. They found that lipase activity presents in the endosperm in 12 hr of imbitition, and the increase in lipase activity is resulted from the factors form the embryo which are not known.

In addition to the lipase, the 33-fold increase in phenoloxidases was observed. The gray color of the bread crumb made from sprouted wheat results from this enzyme complex. The peroxides and catalases also increase during the germination; they take role in the oxidative reactions affecting the rheological properties of dough and the pigment destruction (22).

1.2.3.2. Action of Hormones during Germination

After the water uptake, hormonal signals released from embryo cause synthesis of the hydrolytic and other enzymes. Gibberellic, abscisic acid, auxins, and cytokinins are the hormones that take place in the seed development and germination (17a). Gibberellic acid (GA) produced by the embryo diffuses to the aleurone layer and triggers the synthesis and the secretion of hydrolytic enzymes and the mobilization of reserve materials (14, 3). Also GA is released through the scutellum into the endosperm. Abscisic acid plays a regulatory role in germination. Cytokinins do not take any part at early stages of germination but they may be important for cell growth in embryo. Auxin affects the scutellum (25).

1.2.3.3. Mobilization of the Stored Reserves and Changes in the Kernel

Mobilization of the stored material in the kernel during germination can be studied in different ways. Using light or fluorescent microscopy and scanning electron microscopy, morphological changes can be investigated (Figure 1.7). This allows study of macroscopic changes such as damage of starch granules by α-amylase. Another approach is the extraction of biochemical constituents of the kernel at different stages of the germination and the investigation of the chemical changes of the reserves. In addition to these methods, model systems such as purified enzyme and substrate systems can be used, in which similar processes take place. All methods provide information on the mobilization from different aspects (22).

Figure 1.7 Fluoresce photomicrographs of transverse sections of endosperm embedded in glycol methacrylate / urea / glutaraldehyde and stained with Nile Blue A solution. Note: Starchy endosperm (end), starch (s), lipid deposits (big arrows) and scutellum (sc) parts in the section (reprinted from ref. 26).

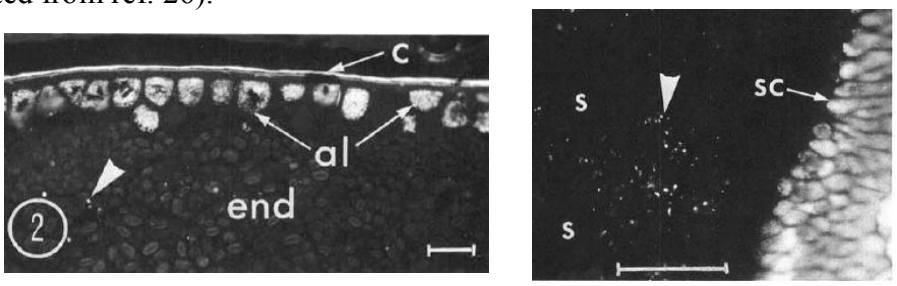

The major mobilization of reserves is initiated after radicle elongation, but some mobilization can occur before completion of the germination. High molecular weight molecules are mobilized and converted into smaller simple molecules in order to transfer nutrients to the growing embryo to support energy-producing events (16). Some microscopic studies showed that in the sprouted kernel starch granules adjacent to the embryo were degraded extensively and protein breakdown started adjacent to embryo within 24-48 hr of germination. In this part of the

kernel, starch granules were found to be free of their protein matrix, and breakdown increased progressively with increasing germination (22, 24).

In the endosperm, starch granules are hydrolyzed into glucose molecules by the enzymes. The process starts adjacent to scutellum and moves from the proximal end to the distal end of the kernel in parallel to the scutellum face, advancing faster adjacent to the aleurone layer (14). Following the degradation of starch granules, carbohydrates in cell walls of endosperm are also degraded. The degradation products (glucose and maltose) are absorbed by the scutellum. According to the proposed pathway in figure 1.8, the degradation products are converted into sucrose in the scutellum and used by the growing root and shoot. None of the sugar accumulates in the scutellum (16, 27).

Figure 1.8 Schematic model of sugar transport from the endosperm to the embryo in germinating wheat highlighting the potential location of sugar transporters. SPS, Suc phosphate synthase; hexose-P,hexose phosphate and conversion of glucose into sucrose (reprinted from ref. 27)

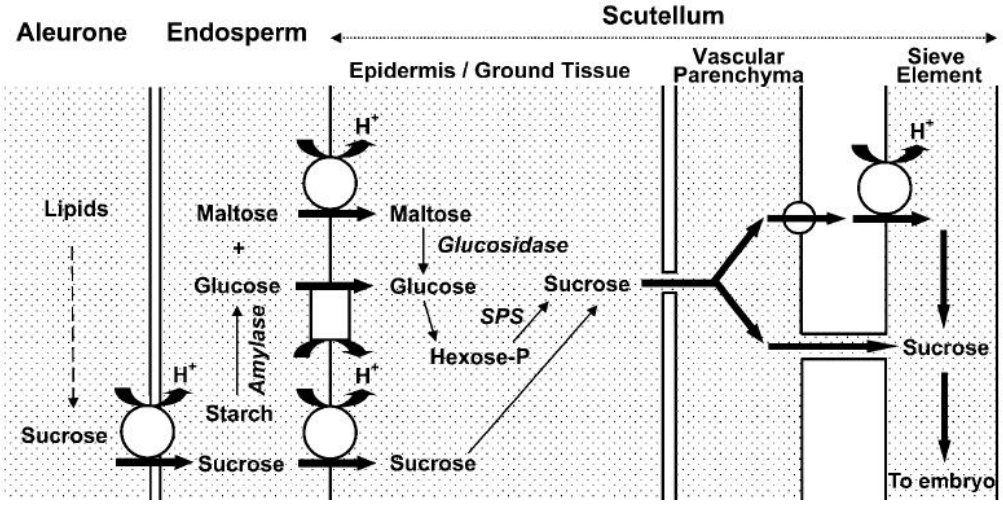

The most of the protein is stored mainly in the aleurone layer and in the protein bodies of the starchy endosperm. There is a minor amount of protein reserve in the scutellum and

embryonic axis. This may be degraded into amino acid and used by growing embryo before the major reserves in endosperm is mobilized (16). Proteolytic activity products in endosperm including amino acids, dipeptides, and small oligopeptides are transferred to embryo via scutellum after they are degraded into amino acids. These building blocks are used for protein synthesis of embryo growth (Figure 1.9).

Figure 1.9 Protein synthesis during germination showing amino acids produced from protein degradation function as building blocks for protein synthesis of the growing embryo (reprinted from ref. 25).

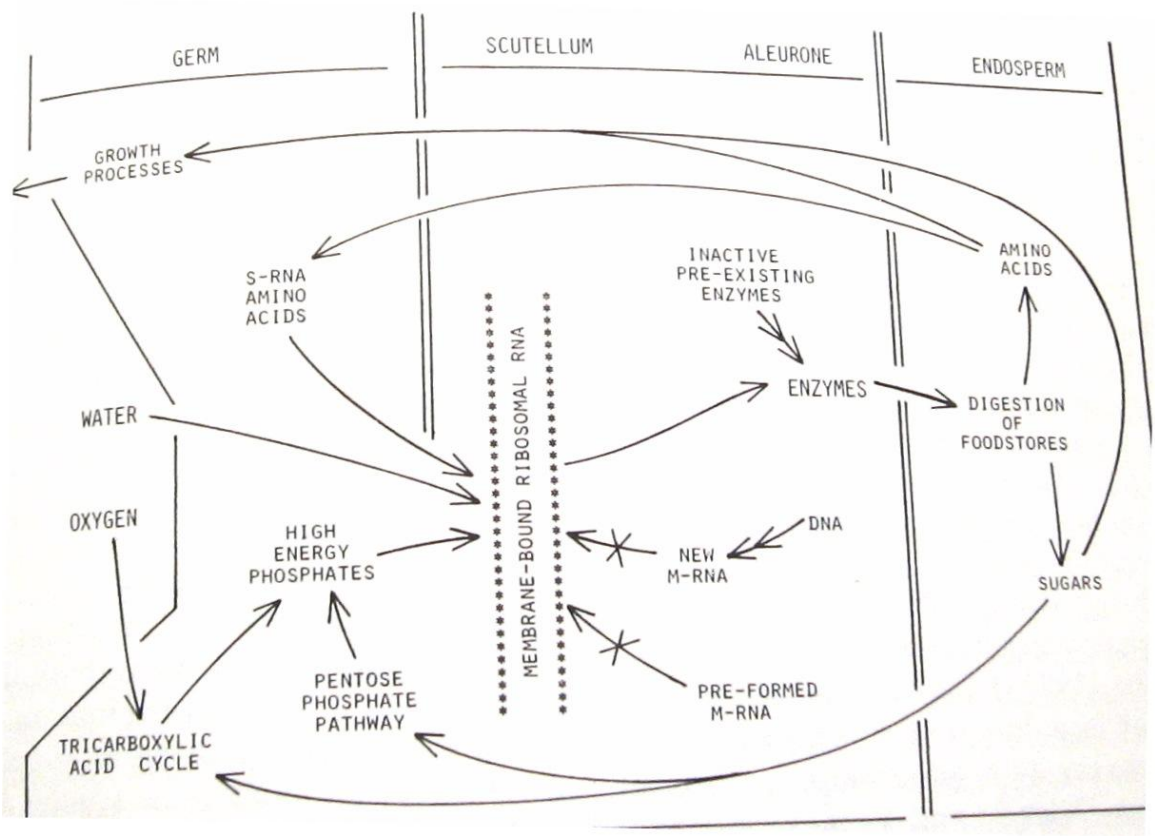

Wheat germ does not contain any native starch. But when the seed was kept 24 hr under moist conditions, starch had accumulated in the germ even though there was no change in endosperm. It was suggested that this starch might be produced by activity of the embryo. When the radicle emerges through the radicle cap and root sheath, starch granules are seen in the cells

of the scutellum. This is an indication of the transfer of the storage material from the endosperm to the germ. The dissolved reserve material is transferred from the endosperm and reforms as small granules in the scutellum. The aleurone cells do not show any changes until starch is almost consumed, then their cell walls collapse and dissolve (2, 13).

Swift and O'Brien (6, 13) studied the fine structure of scutellum before and during germination by light and electron microscopy. For studying the structure before germination, kernels are soaked 3 hr before fixation. By aqueous fixation of kernels, there can be some structural changes at the molecular level, but there are no gross structural changes after 3 hr of soaking. The scutellum is composed of storage parenchyma and vascular tissue. In dry kernels, there is an abundance of protein bodies in the epithelium and parenchyma of the scutellum. Protein and phytin are stored in these protein bodies. Lipid is abundant in the form of small droplets in the cytoplasm of epithelium and parenchyma cells. There are no starch and watery vacuoles in the scutellar cells. In the light photomicrographs of a transverse stained section of a dry kernel scutellum (Fig. 1.10), the abundance of protein bodies is obvious. Protein bodies in the epithelium are small and they are large in parenchyma. Arrowheads show unstained regions where phytate deposits have been lost from the section (6).

Figure 1.10 Light photomicrograph of the transverse section of the scutellum of a dry embryo (SE: cell of scutellar epithelium, SP: cell of scutellar parenchyma, n: nucleus, pb: protein body). The abundance of protein bodies can be seen. Protein bodies in the epithelium are small and large in parenchyma. Arrowheads show unstained regions where phytate deposits have been lost from the section (reprinted from ref. 6).

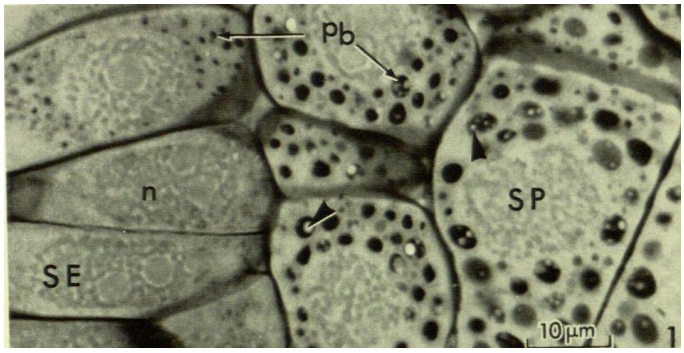

The only change in the scutellum after 3 hr soaking is the appearance and distribution of the nuclear chromatin. In addition, some mobilization of storage proteins in the epithelium appears. Nougarede and Pilet (1964) suggest that water uptake is very rapid in the epithelium and much slower in the parenchyma cells (6).

During germination, after 6 hr exposure very small starch grains appear in the epithelium and parenchyma cells (Figure 1.11a), and when the germination continues, the size and number of the starch grains increases. After 24 hr of germination, there are a large number of starch granules in the epithelium and they are bigger and more abundant in the parenchyma (Figure 1.11c). At this stage of germination, protein bodies in the epithelium have been degraded and small vacuoles are left. Breakdown of the protein in the parenchyma is slower and after 24 hr large masses of partly hydrolyzed proteins are formed by coalescence of the bodies. In the later stages of the germination, protein reserves are completely degraded and only big vacuoles are left in the cells (Figure 1.11).

Figure 1.11 Light micrographs of the scutellum during three stages; 6 hr (a), 12 hr (b) and 24 hr (c) of germination (reprinted from ref.13). Light micrographs of the scutellum during germination showing degradation of protein bodies in the epithelium. Small vacuoles are left after degradation .In the parenchyma large masses of partly hydrolyzed proteins are formed by coalescence of the bodies (dl: depleted layer of endosperm, n: nucleus, pb: protein body, se: scutellar epithelium, sp: scutellar parenchyma, v: vacuole, large arrowhead: starch grains in parenchyma, small arrowheads: starch grains in epithelial cells).

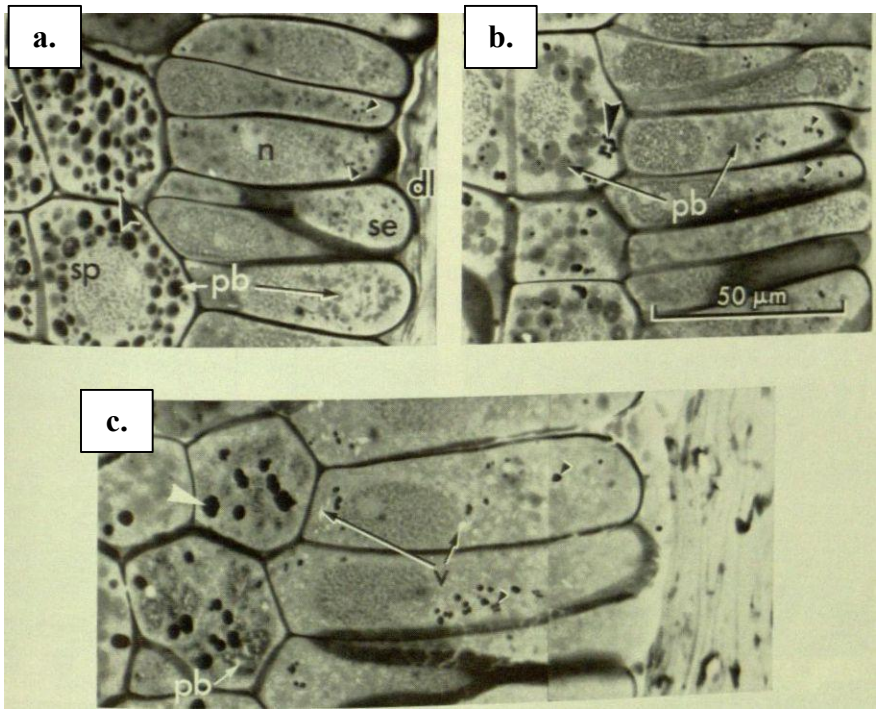

After 24 hr germination, there are some structural changes in epithelium cells. They become elongated and cell walls have been separated from each other. Also starch breakdown starts in the endosperm adjacent to epithelial layer. In addition to these changes, there are changes in organelles endoplasmic reticulum, mitochondria, nucleus, and plastids observed by electron microscopy which can be correlated with metabolic activity.

There is no detectable change in the lipid bodies after 12 hr soaking. After 24 hr; they became less common near the cell membranes of the epithelium cells. In the later stages of germination, there is a reduction in their number, however their utilization is slow. In some studies, it has been suggested that the starch in the scutellum is derived from the lipid bodies,

because starch can be seen in the scutellum before significant mobilization of the endosperm reserves (13).

Tavener and Laidman (20) studied on the triglyceride metabolism in the germinating wheat kernel. They observed that triglyceride reserves were degraded progressively. Breakdown starts within 12 hr imbibition in the embryonic axis and starchy endosperm. Since the germ does not contain carbohydrate reserves, the triglycerides may provide energy during early germination.

1.3. Infrared Spectroscopy

The infrared radiation includes wavelength range 13,000-50 cm^{-1} or 0.75-200 μm. The entire region is divided in three parts; near-IR 0.75-2.5 μm (11,000-4,000 cm^{-1}); mid-IR 2.5-20 μm (4,000-600 cm^{-1}), and far-IR 20-200 μm (28). IR spectroscopy has long been regarded the ideal technique for qualitative analysis and structural information of organic material. The same is true for far-IR. The near-IR region has found use for quantitative data analysis.

When infrared radiation is absorbed by a species, atoms in molecules vibrate. Vibration frequency is dependent on the masses of the atoms involved and the force of holding the atoms together. Only these frequencies that can cause the atom in molecules to vibrate are removed from IR transmittance radiation. Therefore the absorbance spectrum frequency is the fundamental vibrational frequency of the atom. The IR spectrum is obtained by the change in the dipole moment of the atoms by molecular vibrations and rotations. Information of the chemical compounds is based on the absorption intensities of the vibrational bands. There is a linear relation between the absorbance intensity and the concentration of the molecules. Relative amounts of various peaks based on absorbance peak height and ratios provide semi-quantitative information in mid-IR.

The mid-IR region (4000-600 cm^{-1}) involving the fundamental vibrations and fingerprint region has sharp and narrow peaks and the peaks are not necessarily overlapping. Stretching vibrations identify which atoms vibrate and the fingerprint region reveals the environment. The length of the hydrocarbon chain can be determined by comparing the CH_3 and CH_2 vibrations. Also the unsaturation levels can be detected by C=C-H or C=C vibrational bands. The relative population of lipids, proteins, and carbohydrates can be revealed by measuring the absorbance at certain frequencies for N-H to determine protein, O-H for moisture, and C-H for lipid. Shifts in the frequencies of the bands give an idea about the chemical environment of infrared active group (29, 30). There are of two types infrared spectrometers which can scan entire spectrum; dispersive prism (refraction) or grating (diffraction) spectrophotometers and interferometer (FT-IR) spectrometer. FT-IR has been widely used mostly in last 20 years.

One of the most important advances in the instrumentation of the vibrational spectroscopy is achieving microspectroscopy when radiant is sufficiently conserved to obtain a suitable S/N for spot sizes in a few micrometers. In addition, usage a motorized stage enables mapping of tissue. This new capability gives scientist the opportunity of linking the analytical chemical to the morphology of the material in the field of view. Following these, synchrotron radiation was used for FT-IR enabling high spatial resolution. Chemical imaging became successful with the development of cameras based on silicon charge-coupled device (CCD) arrays which are sensitive to near-IR and focal plane arrays indium gallium arsenide (InGaAs) or indium antominade (InSb), the mercury cadmium telluride (MCT) detectors sensitive to near and mid-IR respectively (31). The imaging applications developed with the vibrational spectroscopy provides the simultaneous combination of chemical and spatial information. Moreover, in some cases spectroscopic analytical information can be obtained nondestructively.

1.4. Fourier Transform Infrared (FT-IR) Microspectroscopy

In traditional microscopy, sample preparation includes several steps such as fixation of the tissue, embedding in a matrix, and microtoming. Histochemical information is obtained with the application of specific stains that selectively bind to different components and from these specimens it is very difficult to generate quantitative information. Vibrational spectroscopy makes it possible to obtain spectra of the microtomed sections of the tissues without the intrusive application of stains and chemical reagents like in conventional light and fluorescence microscopy (29, 31).

FT-IR microspectroscopy and imaging became valuable techniques to study the molecular chemistry of biological materials by allowing connection to morphology. FT-IR combines infrared spectroscopy with light microscopy in order to locate the area to be analyzed and thus molecular information is obtained with great spatial resolution or microscopic scale (32, 31). The FT-IR technique has been used to identify and determine the molecular chemistry of many different materials including forensic materials, plant and animal tissues, minerals, polymer films and pharmaceuticals.

1.4.1. Fouirer Transform Instrument

The Fourier transform instrument is based on a Michelson interferometer. In this system, the beam is divided in two pathways with a beam splitter. Two beams are combined after passing through the alternate pathways and reflected on the detector. The length of one pathway constant with a fixed positioned mirror whereas in the other pathway a movable mirror adjust the length as a function of time. When a certain frequency passes through, the movable mirror adjusts in order to obtain the right distance is combined with the same frequency of the fixed path (zero path length difference). A maximum response is obtained at that frequency by constructive

interference in this case. An interferogram is generated by holding the spectral information from sample in time domain as a cosine wave, intensity is recorded versus time based on the speed of the moving mirror. This time domain spectrum is converted into a frequency-domain spectrum with a Fourier transformation function (33, 29). There are important advantages of FT-IR over dispersive IR for microspectroscopy. The FT-IR spectroscopy utilizes an interferometer in which all frequencies of the radiation pass though the sample and are collected by the detector simultaneously (Fellget or multiplex advantage) with this optical scheme. An improved S/N ratio can be obtained in a short amount of time and high S/N enables dividing the signal into many channels, thus very good spectral resolution is obtained. In addition, it provides higher energy throughput due to the absence of the slits (Jacquinot advantage) (33, 28).

1.4.2. Advances in Infrared Microspectroscopic Instrumentation

The first IR microscope attachment to an IR spectrometry was proposed in the 1950's by Coates, Offner, and Siegler (34). Infrared microspectroscopy became more practical by combining FT-IR spectrometry with high sensitivity detectors (33). The first FT-IR microscope was introduced in 1986, patented in 1989 by Messerschmidt and Sting. It was equipped with reflecting optics and dual-mode imaging plane masks. The Spectra-Tech, IR-PLAN^{TM} microspectrometer became available in 1986 and has been used widely providing better optical efficiency to maintain S/N and dual projected image plane masking. The confocal term has been previously referred to as "double aperturing" by Robert Messerschmidt, who designed the Spectra Tech IR PLAN^{TM}. The specimen spectrum becomes contaminated with spectral features from the foreign material outside of the target spot size with single masking. This contamination is eliminated with dual mask, thus purer spectrum and better spatial resolution is obtained. In 1990, an integrated system consisting of an infrared microscope and interferometer bench was

introduced by SpectraTech/ IRμs™ (35). Number of the mirrors was eliminated from optical path improving throughput. Mapping capability is enhanced with a microprocessor controlled motorized stage.

Table 1.1 Major developments in infrared microspectroscopy instrumentation (reprinted from ref. 40)

Major developments in infrared microspectroscopy instrumentation	
1949	First papers combining infrared spectroscopy and microscopy R. Gore(*Science*), R. Barer (*Nature*)
1953	PerkinElmer developed the first commercial microscope for IR spectroscopy
1978	Nanometrics introduced the NanoSpec 20-IR microspectrometer
1983	Bio-Rad and Analect introduced FTIR microscopes
1986	Spectra-Tech invented the IR-Plan Research Microscope
1989	Spectra-Tech introduced the IRμs microspectrometer system with automated mapping
1989	Spectra-Tech invented the Grazing Angle Objective
1990	Spectra-Tech invented the micro-ATRobjective
1994	NIH (Lewis and Levin) invented an infrared spectral imaging system using an array detector
1998:	Spectra-Tech invented the Continuμm microscope (infinity corrected)
1999	SensIR invented an ATRvideo microscope
2000	SensIR introduced an ATR video FTIR microanalysis system

One of the next steps in advancement is the interfacing an infrared microspectrometer to synchrotron radiation in 1993 (37). The brightness of the synchrotron is 100-1000 times greater than globar sources providing a better spatial resolution and higher S/N ratios. The development of single detector instruments progressed significantly with the introduction of the first infinity corrected confocal infrared microscope by Reffner and Vogel (36). Infinity corrected mirrors

enabled the placing of a polorizer providing differential interference contrast (DIC) and it also extend the path length. FT-IR was developed with a conventional thermal infrared light source and single infrared detector (35). Infrared microscopes were customized for a small target size was achieved with dual 32X Schwarzschild mirror lens and liquid nitrogen cooled MCT detector with a 50 μm x 50 μm element (35).

Important progress in imaging with FT-IR microspectroscopy started with substitution of single element detector with a focal plane array (FPA) detector in 1994 (38, 39). The FPA detector has an array of infrared detector elements that provides collection of the spectra of different pixels on the sample area simultaneously by measuring the all frequencies with an interferometer. Initially, it had a liquid nitrogen cooled FPA camera with MCT photovoltaic detectors in a 64 x 64 array with a step-scan interferometer. With this initial FPA system, the spectral quality of the data is not as good as a single detector FT-IR microspectrometer due to operation at 16 cm^{-1} resolution with low S/N. However this problem was solved with some improvement in step scan. Later the quality was improved with some advances in FPA with rapid scan array instruments. MCT photovoltaic optical detector elements were replaced by photoconductive mechanism. FPA instruments and 16- element pushbroom linear array have been used recently.

1.4.3. Applications of FT-IR Microspectroscopy on Plant Material

FT-IR microspectroscopy has been widely used on plant material and wheat (39, 41, 42, 43). In a series of publications, Wetzel and coworkers examined biological tissues with FT-IR microspectroscopy. Their studies started with the first microscope accessories and followed by integrated FT-IR microscope. In addition their exploration included using a synchrotron source to increase the spatial resolution and finally FPA imaging systems. In 1987, early work was done

by Wetzel, Messerschmidt, and Fulcher by looking at isolated components from different parts of the wheat kernel (44). The pericarp, seed coat, aleurone cells, and endosperm were examined. Spectra for the isolated gluten, starch, lipid, and cellulose were also reported. Following of this study Wetzel and Fulcher (45) showed the local chemical differences within the same section from one kernel and characterized each different botanical part. The first mapping of a wheat kernel *in situ* was performed by Wetzel and Reffner (46). The mapping was done with a motorized stage. Later the microstructure of the wheat kernel was examined with different maps with a programming stage of IRus integrated FT-IR (44). The first FT-IR microspectroscopic imaging of wheat section by using a MCT FPA detector was reported in literature in 1999 (39).

1.4.4. Synchrotron Infrared Microspectroscopy

Synchrotron infrared microspectroscopy allows ultraspatial resolution. There are three important reasons making synchrotron infrared microspectroscopy more advantageous than the techniques using a conventional globar source. First, the synchrotron radiation is 100-1000 times brighter. In addition, it is free of thermal noise of hot filament and the light emitted is highly directional. Therefore maximum radiation flux on the smallest possible area provides high spatial resolution and high spectral resolution without excessive coaddition (47, 48). In the synchrotron, electrons from an electron source were accelerated with a linear accelerator. It produces an energy of 75 million electron milivolts (meV), these electrons enter a booster ring, here they are accelerated more, and enters a vacuum ultraviolet (VUV) storage ring (Figure 1.12). The VUV storage ring has eight bending magnets, and 176 radiation ports. When electron accelerates, they radiate energy in the form of electromagnetic waves. Synchrotron light consists of a continuous spectrum of electromagnetic radiation ranging from x-ray to infrared. Infrared beam from the beam line port is extracted and directed to microspectrometer (47).

Figure 1.12 Diagram of NSLS (A: electron source, B: linear accelerator, C: booster accelerator ring, VUV: Vacuum ultraviolet storage ring with associated beamlines. Electrons are accelerated from with a linear accelerator and produce an energy of 75 million electron milivolts (meV), and enter a booster ring, and are accelerated more and enter vacuum ultraviolet (VUV) storage ring (reprinted from ref. 29).

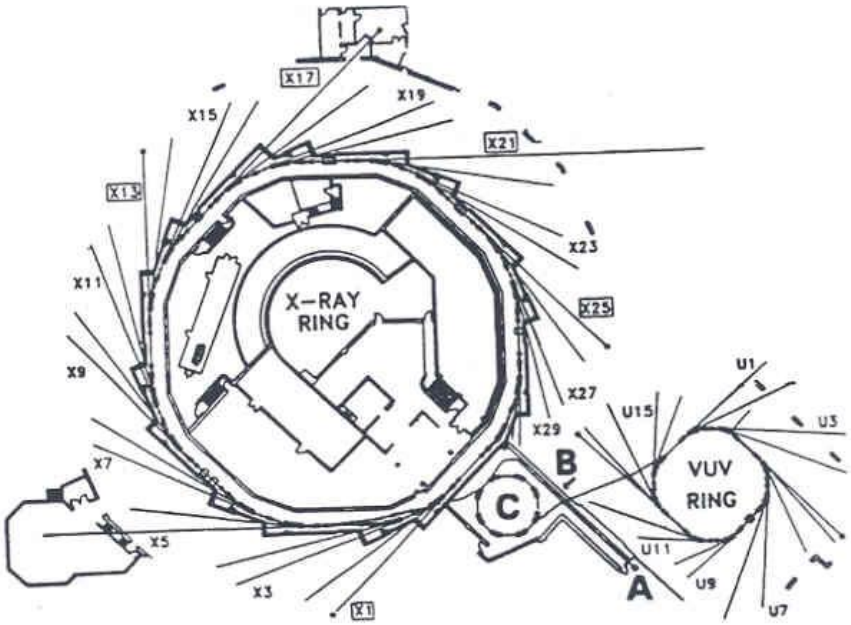

2. Experimental

2.1. Instrumentation

FT-IR microspectroscopy was carried out on U10b and U2b beamlines on the vacuum ultraviolet storage ring at the National Synchrotron Light Source (NSLS) of Brookhaven National Laboratory (BNL) Upton, NY. Initial experiments and first attempts for semiquantitation were achieved at NSLS. Subsequently, large data sets were acquired from three hard wheat varieties and mapped in the KSU Microbeam Molecular Spectroscopy Laboratory with the focal plane array instrument.

2.1.1. Instrumentation at Synchrotron

Beamline U10b was equipped with a Continμum^{TM} infrared microscope (Spectra Tech / Thermo, Madison WI) interfaced to a Magna 850 FT-IR spectrometer (Nicolet / Thermo,

Madison WI). Schwarzschild 32X objective and condenser mirror lenses were used on a double pass single mask beam path to project a 10 µm x 10 µm confocally targeted spot (Figure 1.13). A 50 µm x 50 µm liquid nitrogen cooled MCT detector essentially matched the beam from the image plane mask of the microscope. It allowed single real-time scanning of the spectrum while viewing. With the Continµum^{TM} infrared focus is adjusted from the single beam energy response at the wavenumber range of interest. A resolution of 8 cm^{-1} was used with 16 scans coadded unless otherwise stated.

Figure 1.13 Continµum^{TM} infrared microscope. Continµum^{TM} infrared microscope includes matched Schwarzschild 32X objective and condenser mirror lenses were used on a double pass single mask beam path, infinity corrected dual confocal operation (reprinted from ref.35).

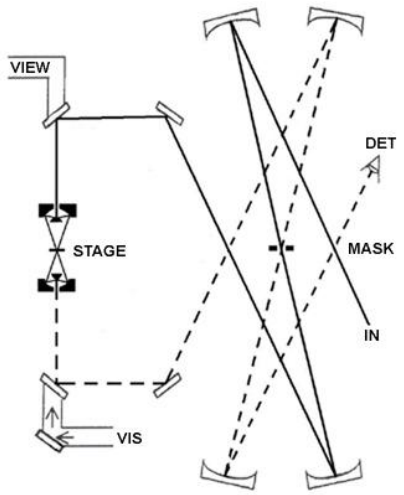

Beamline U2b was equipped with a NicPLAN^{TM} model infrared microscope (Nicolet / Thermo, Madison WI) interfaced to a Magna 850 FT-IR spectrometer (Nicolet / Thermo, Madison WI) (Figure 1.14). In NicPLAN^{TM} microscope Schwarzschild 32X objective and 10X condensers were used. A single mask positioned before objective, and a pinhole image plane mask placed after condenser to maintain purge. The infrared focus was adjusted to obtain the maximum count (signal) before spectra were recorded. Before data collection, visible focus was

used for image capture. For data collection on BaF_2, infrared focus was achieved based on the intensity of the detector response prior to automated mapping sequence. A resolution of 8 cm^{-1} was used with 16 scans coadded.

Figure 1.14 U2b beamline. Beam coming from the ring (1) enters FT-IR spectrometer (2) and from the beamsplitter of the interferometer it is directed towards the IR microscope (3), a computer (4) attached to the system controls the stage, microscope and spectrometer operation.

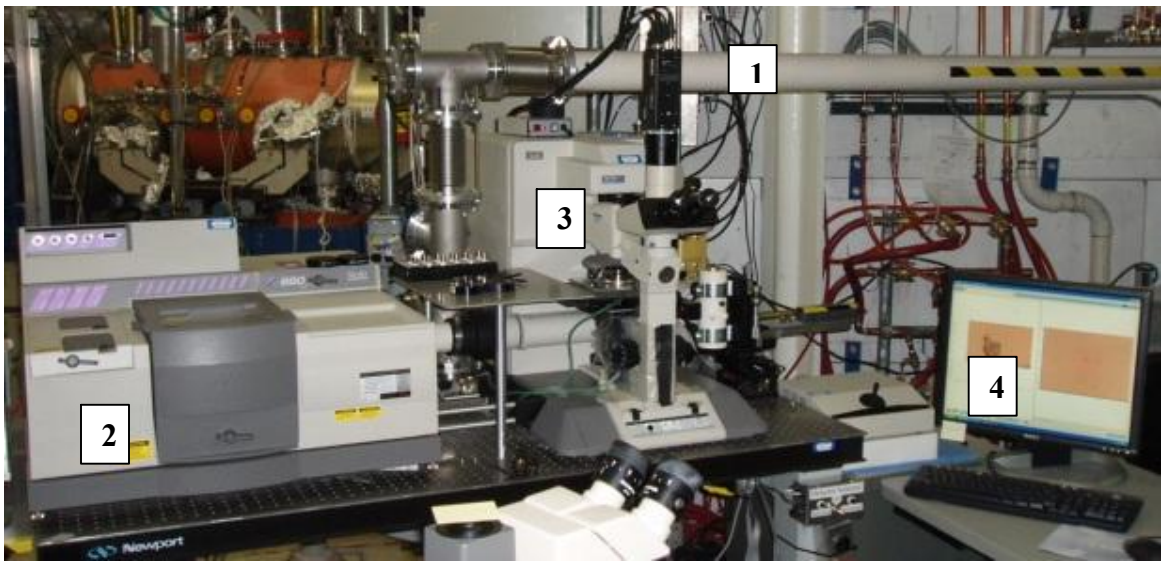

2.1.2 Instrumentation at KSU

Spotlight™ 300 Spectrum One instrument (Perkin-Elmer, Danbury, CT) was used in this quantitative phase of this project to map wheat sections of three hard wheat varieties in the transmission mode. This FT imaging microspectrometer equipped with a 16-element "pushbroom" array was operated with a nominal 6.25 μm x 6.25 μm pixel size. 8 cm^{-1} resolution was used and 64 scans were coadded. For the background spectrum, 240 scans were coadded. The images containing 1000-3000 pixels were mapped from each section. The Spectrum Spotlight imaging system, shown in figure 1.15, is composed of an infrared microscope, a Spectrum One FT-IR spectrometer and a stage controller that included a joystick

Figure 1.15 Spectrum Spotlight imaging system including a Spectrum One FT-IR spectrometer connected optically interfaced to a microscope, and electronics for microprocessor control of stage, microscope and spectrometer operation (reprinted from ref. 49).

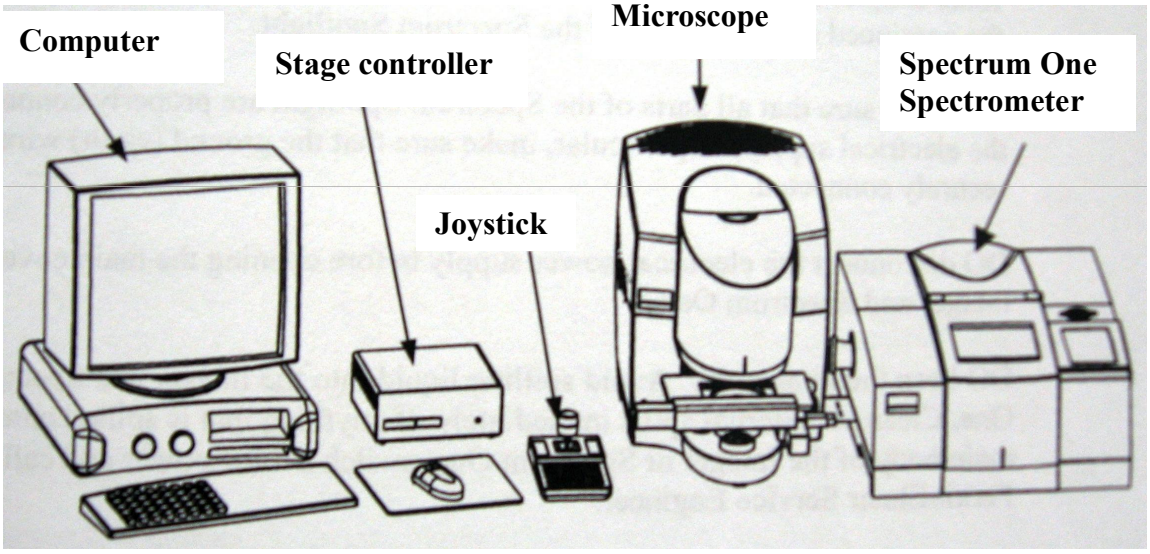

The microscope magnifies the visible light image of the sample and the Monitor Visible window of the Spotlight software displays the selected sample image as a mosaic. The data collection and processing is controlled by the Spotlight software. The infrared microscope has a motorized stage which is controlled either by joystick or the Spotlight software. Movement of this motorized stage is used to select points on the sample to be analyzed or mapped. Focusing can be performed by manual adjustment while viewing the live image. Both infrared radiation and visible light are sent to the remote aperture by the same cassegrain mirror lens (49).

Data collection can be done in a detector array image mode or a single detector point mode. IR microspectrometer with a FPA is shown in the figure 1.17. In point mode, a single MCT detector records the spectrum of each spot on the microscope stage one at a time. With single detector a remote image operating mask is used to restrict the spot size from which a spectrum is recorded. Operating in image mode, 16 MCT detector elements in a linear array record spectra simultaneously in parallel. As the motorized stage moves, mapping a particular

area of the sample produces spectra for many pixels from which multiple chemical images may be generated. This is done by selecting the area of interest by drawing a box around it and to program the scanning operation. From the data obtained, individual spectra can be extracted for any pixel (x, y) on the sample area. In this study, scutella of the each section were analyzed in image mode by selecting two or three rectangular areas containing between 1000-3000 pixels each. All the spectra were extracted from each of the maps and used for further examinations and calculations.

Figure 1.16 Schematic of IR microspectrometer with a single-element detector having the capability of confocal operation with apertures before and after sample. This is a generalized schematic consistent with the Continμum^{TM} and NicPLAN^{TM} instruments at beamlines U10b and U2b (reprinted from ref. 50).

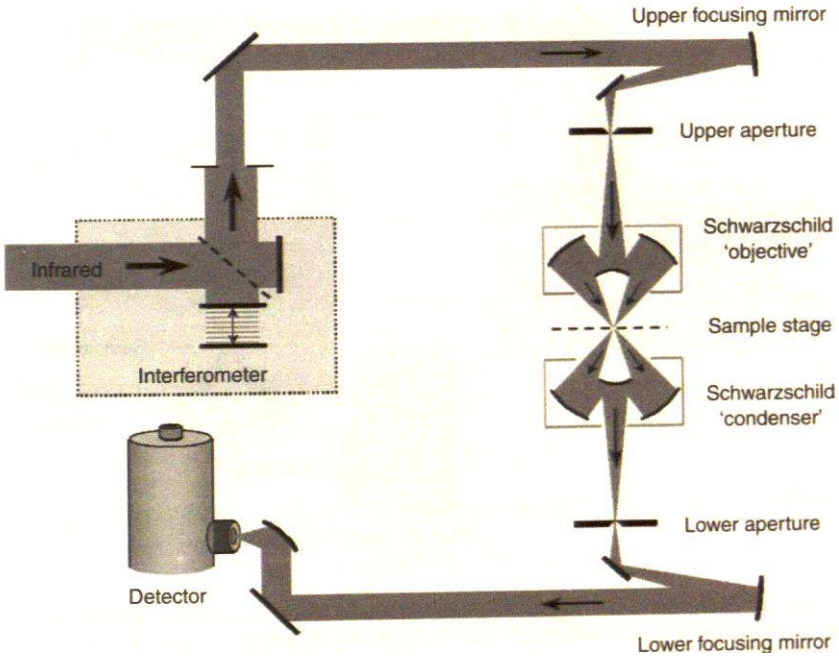

Figure 1.17 Schematic of IR microspectrometer with a FPA detection which has an array of IR detectors enabling whole spectrum scanning of the entire field of view with a single scan (reprinted from ref. 50).

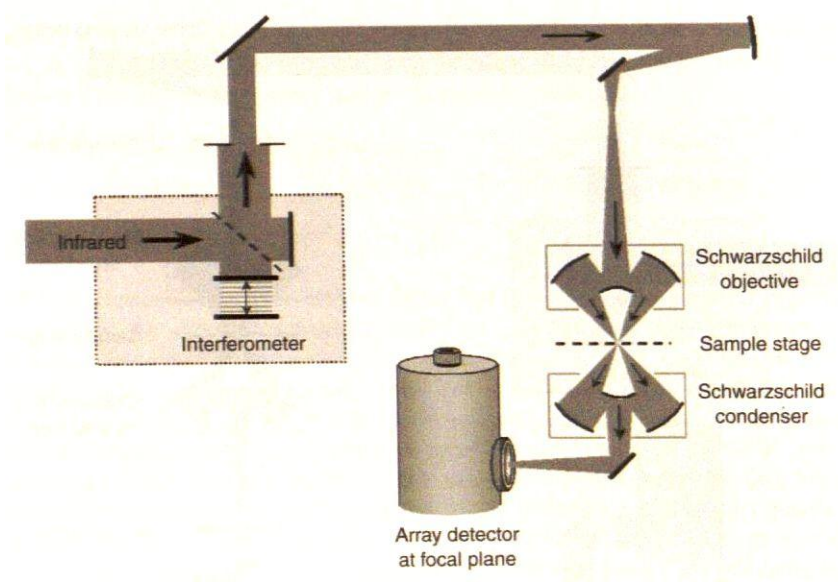

2.1.2.1 Optical system and mapping procedure of Spotlight:

Both infrared microspectroscopy and visible light optics exists in the microscope. These systems intersect at the aperture. Spotlight enables to work in transmittance and reflectance operations. Dichroic mirrors are used to reflect infrared and transmit the visible light alternatively. When a sample is viewed with the camera, a conjugate image of it is seen at the remote aperture. By moving the stage position up and down (Z-control) with the joystick, the optical image is focused. Viewing a sample in transmittance is illustrated in figure 1.18.

Figure 1.18 Path of the visible beam for viewing a sample in transmittance. Visible light from Light-emitting diode (LED) illuminator traverses the sample and is sent to the upper dichroic mirror (reprinted from ref. 49).

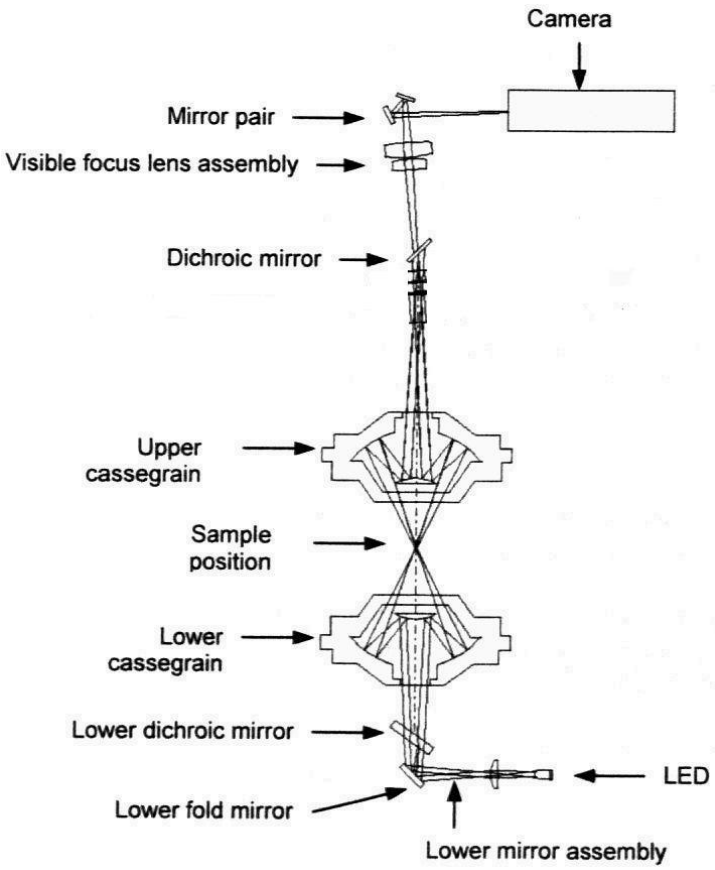

Visible light from Light-emitting diode (LED) illuminator is directed by the lower fold mirror to the lower dichroic mirror onto the lower cassegrain mirror lens. The beam is condensed and focused onto sample position by lower cassegrain. After the light traverses the sample, it is collected by upper cassegrain and sent upward through the image plane mask and the upper dichroic mirror.

After sample is viewed and an area is selected for analysis, the visible image is captured. The path followed by the infrared beam from the beam splitter during mapping is shown in figure 1.19.

Figure 1.19 Path of the infrared beam for collecting an image in transmittance. Infrared radiation from the beamsplitter of the spectrometer is reflected onto the lower dichroic mirror, at the end of the travel it is focused onto the MCT detector (reprinted from ref. 49).

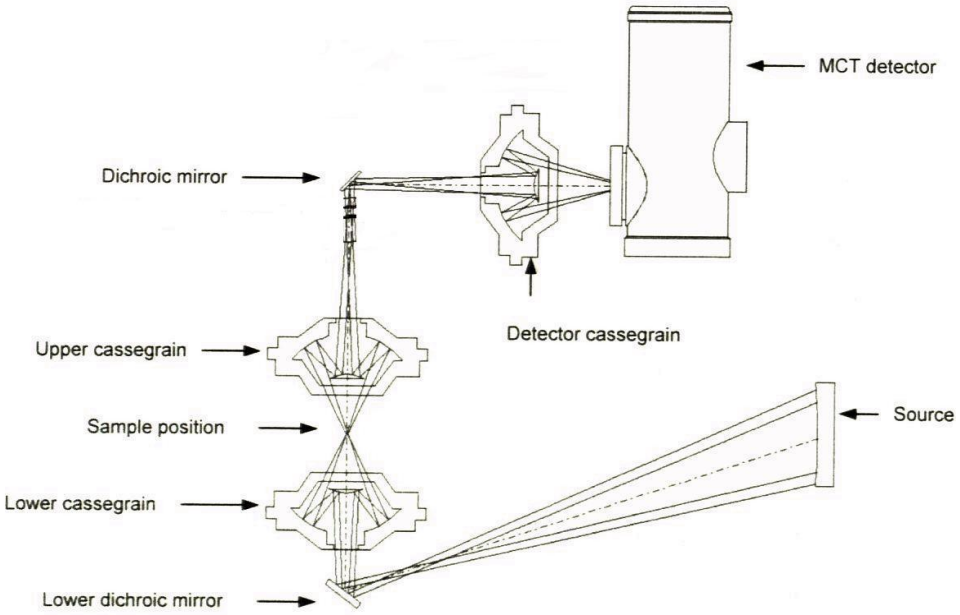

Since upper cassegrain is used for both visible light and infrared radiation, focusing the sample from visible image positiones it correctly for infrared imaging. The beam path in collecting data differs from that for viewing. Infrared radiation from the beamsplitter of the spectrometer is reflected onto the lower dichroic mirror that sends it to the lower cassegrain. The exiting the upper cassegrain is focused onto the MCT detector by the detector cassegrain.

IR magnification can be changed from low to high (25 μm to 6.25 μm) by a microprocessor controlled mechanism that rotates a series of magnifying mirrors into the IR beam.

2.1.2.2. MCT Detector

The mercury cadmium telluride (MCT) detector array in the infrared microscope is cooled to 77ºK to prior to collection of data. The dewar is carefully filled with liquid nitrogen. When full, the temperature of the detector is reduced and operating sensitivity is achieved. The

filled dewar keeps the MCT detector cool at the proper operating temperature for at least 6 hr. At the end of this time period, the dewar begins to return to room temperature and power is switched off to the MCT.

2.2. Sample preparation

The wheat kernels were soaked in distilled water at 4^{o}C for 6-8 hr in order to soften the seeds and prepare them to the cryogenic sectioning with a microtome. Keeping at refrigerator during soaking avoids sprouting in this preparation step. After soaking, surface moisture of the kernels were removed with Kim wipes and they were mounted on the sample plate (germ side up) via embedding in a supporting medium Tissue Tech (OCT) and frozen at -20^{o}C before microtome sectioning. The thin sections (4-6 μm) were produced to obtain good and undistorted absorption bands in the transmission mode. The sections were thaw mounted onto 1 mm thick x 13 mm Barium fluoride (BaF_2) disks. The frozen section of the tissue melts on the disk due to the temperature difference of the tissue and the disk. The BaF_2 is not hygroscopic and has a transmittance cutoff 800 cm^{-1}.The tissues mounted on BaF_2 were analyzed in the 4000 cm^{-1} and 800 cm^{-1} range by IR microspectroscopy.

Optimizing sectioning angle

Some preliminary sectioning experiments were done to determine the proper angle in order to obtain good sections having a high amount of the scutellum. In the first sectioning experiment, the angle of slicing was the smallest and it was gradually increased in successive trials. The successively prepared sections for the first small sectioning angle are shown below (Figure1.20).

Figure 1.20 The successive sections for the first small slicing angle. The scutellum areas are shown in the red boxes. Amount of the scutellum is decreasing gradually successive sections further into the kernel.

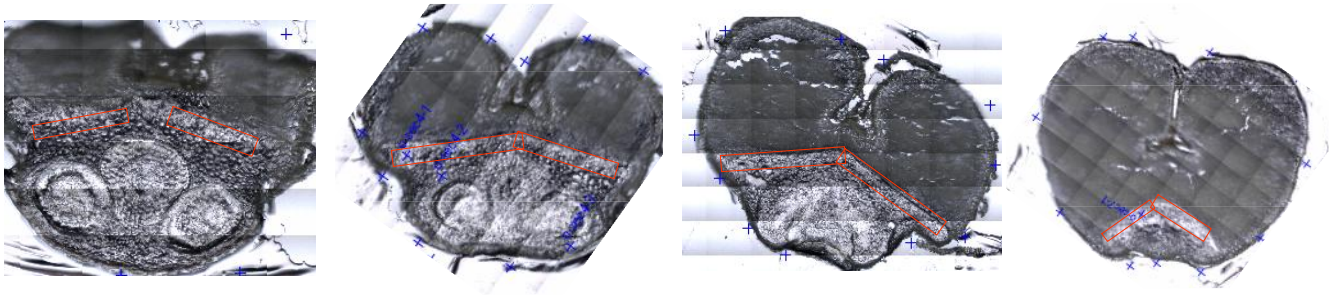

The areas shown in the red boxes are within the scutellum. In the first section, the embryonic axis is the highest quality part of the section, in the other three sections amount of the scutellum is decreasing gradually further into the kernel. It is difficult to distinguish between the coleorhiza and scutellum in the last section. The selected areas for mapping should not be very close to the embryonic axis in order to avoid the coleorhiza.

In the second sectioning experiment, an angle larger than the first was tried. As seen in the photograph the angle is more than 45°. 

Figure 1.21 The successive sections obtained at the larger angle. The scutellum areas are shown in the red boxes.

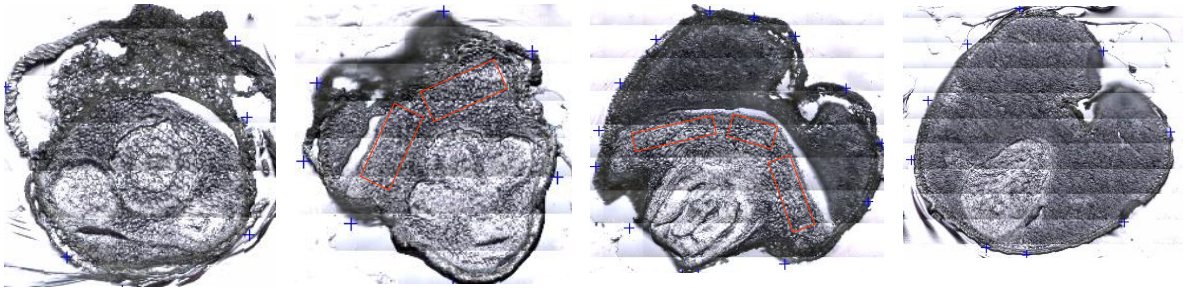

In the first and the last sections, it is very hard to make the distinction between the coleorhiza and the scutellum tissues, but in the middle sections the amount and the quality of the scutellum to work with is ideal.

In the next sectioning experiment, the angle was the widest used. Sectioning 3: 

Figure 1.22 The successive sections obtained with the widest angle. Not much scutellum is exposed in the sections.

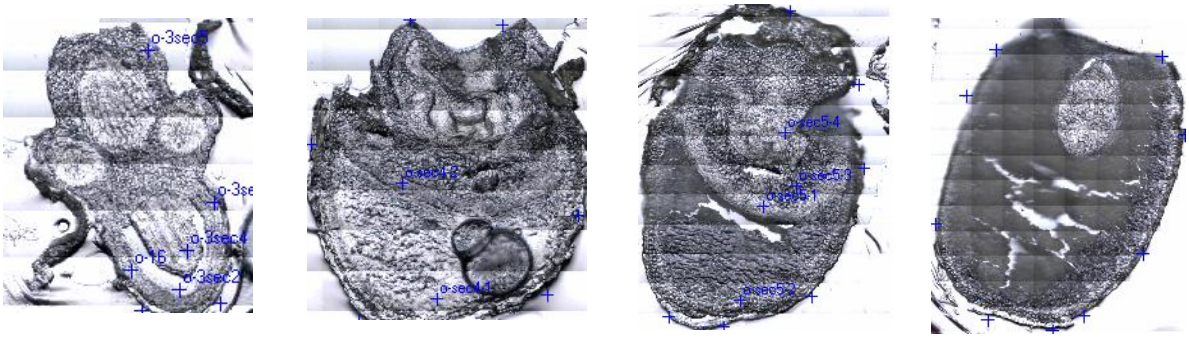

This angle was not good for the purpose of this study because not much scutellum is exposed in the sections that result.

The second angle used was chosen for all subsequent sectioning due to optimum the scutellum presentation. The kernels of the cultivars Trego, Danby and KS2174 were sectioned using this angle by adjusting either the blade angle or the seed mounting angle. The samples referred to as called as control were unsprouted (0 hr germination) and they were not exposed to moisture. Prior to sectioning, they were soaked at refrigerator temperature as previously stated. The laboratory sprouted kernels were allowed to germinate for either 24 hr or 36 hr based on evidence of the seed dormancy. The sprouted kernels were exposed to moisture on moist blotter paper in Petri dishes and they were sectioned immediately after the end of the germination duration. If the samples could not be sectioned immediately, then they were kept at -80^{o}C for 24 hr to terminate the germination process, and sectioned immediately after thawing. Sections

containing both germ and endosperm with an optimum scutellum area were produced and analyzed for the sprouted and the unsprouted kernels.

2.3. Microspectroscopic Procedure and Data Processing

Replicates of the hard wheat cultivars HW and Jagger were mapped in a raster grid in 10 µm steps resulting in a 10 µm pixel size using the Continµum^{TM} infrared microscope in preliminary experiments with sections from kernels that had been analyzed previously by near-IR nondestructive subsurface polychromatic contrast imaging to reveal the developing embryo. For each pixel in the grid an infrared spectrum in the range of 4,000 cm^{-1}–680 cm^{-1} was recorded. The same system with a NicPLAN^{TM} infrared microscope was used on another synchrotron visit to perform line mapping from the germ area. This enabled quantitative comparison of typical germinated vs. ungerminated populations on the basis of lipid to protein peak area ratios. With the Spotlight, scutella of the each section were analyzed in image mode by selecting two or three rectangular areas containing between 1000-3000 pixels each. All the spectra were extracted from each of the maps and used for further examinations and calculations.

From data collected in image mode functional group maps and peak area ratio maps were produced to compare the localized spectroscopic differences between of sprouted and unsprouted kernels (OMNIC, Atlµs software (Thermo Fisher Scientific, Madison, Wisconsin), and Spotlight software (PerkinElmer, Shelton, Connecticut) were used to control data acquisition. Malvern's ISys Imaging software was used to allow further data treatment). Initially the important peaks were selected and band assignments were made based on the previous studies on wheat done by Wetzel and coworkers. Peaks that are indicators of different compounds such as lipid, protein and starch in wheat are shown.

Background spectrum were obtained by mapping an area free of sample on BaF_2 disk was single beam scanned with 8 cm^{-1} resolution and 240 scans coadded to obtain a background spectrum. The spectrum shown in figure 1.23 was ratioed to the sample spectrum to produce a transmission spectrum from which an absorbance spectrum was calculated. Water vapor and CO_2 contributions were removed with this correction.

Figure 1.23 Background spectrum showing rotational bands of water vapor approximately at 4000-3800 cm^{-1} and $C0_2$ at 2360 cm^{-1}

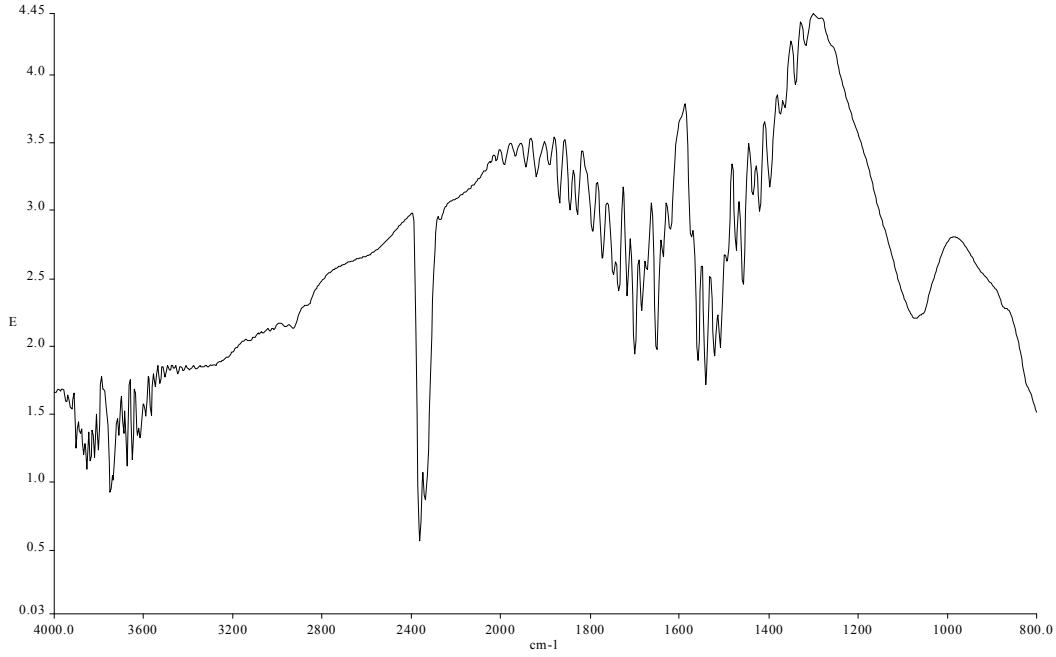

In the figure below (Figure 1.25), a spectrum obtained from scutellum area of an unsprouted kernel is shown. The fundamental vibrations seen in the spectrum include either O-H or N-H stretch vibrational bands at 3300 cm^{-1}. Note that the O-H band shape is round from starch or cellulose chemical structures, but the N-H stretching vibration produces a sharper peak and it is shifted slightly from the 3300 cm^{-1} O-H absorption band (Figure 1.24). The strong absorbance of the N-H stretch in the spectrum indicates that the tissue is rich in protein. C-H vibrational

bands at 2927 cm^{-1} (CH_2 stretch) and at 2850 cm^{-1} (CH_3 stretch) region are predominant for the lipid components. A small peak at approximately 3015 cm^{-1} shows unsaturation of the lipid by the stretching vibration of the C-H attached to a C=C.

Figure 1.24 A wheat cross section and total absorbance image. A spectrum extracted from endosperm side is showing O-H round peak at 3300 cm^{-1}.

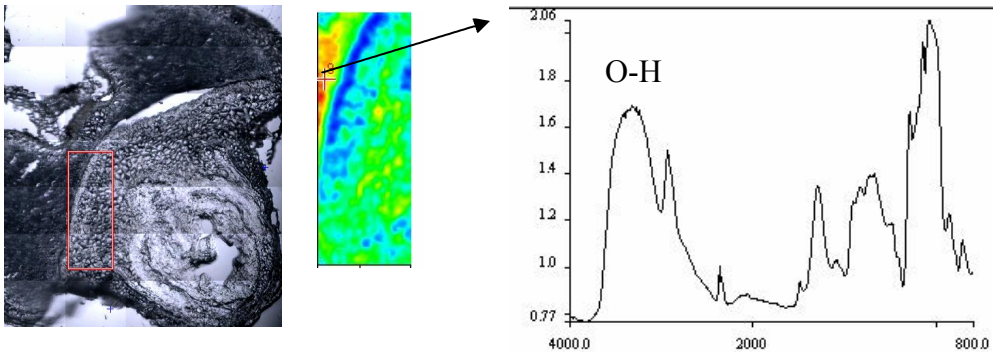

Figure 1.25 A spectrum representative of the scutellum part of an ungerminated kernel with assigned peaks superimposed.

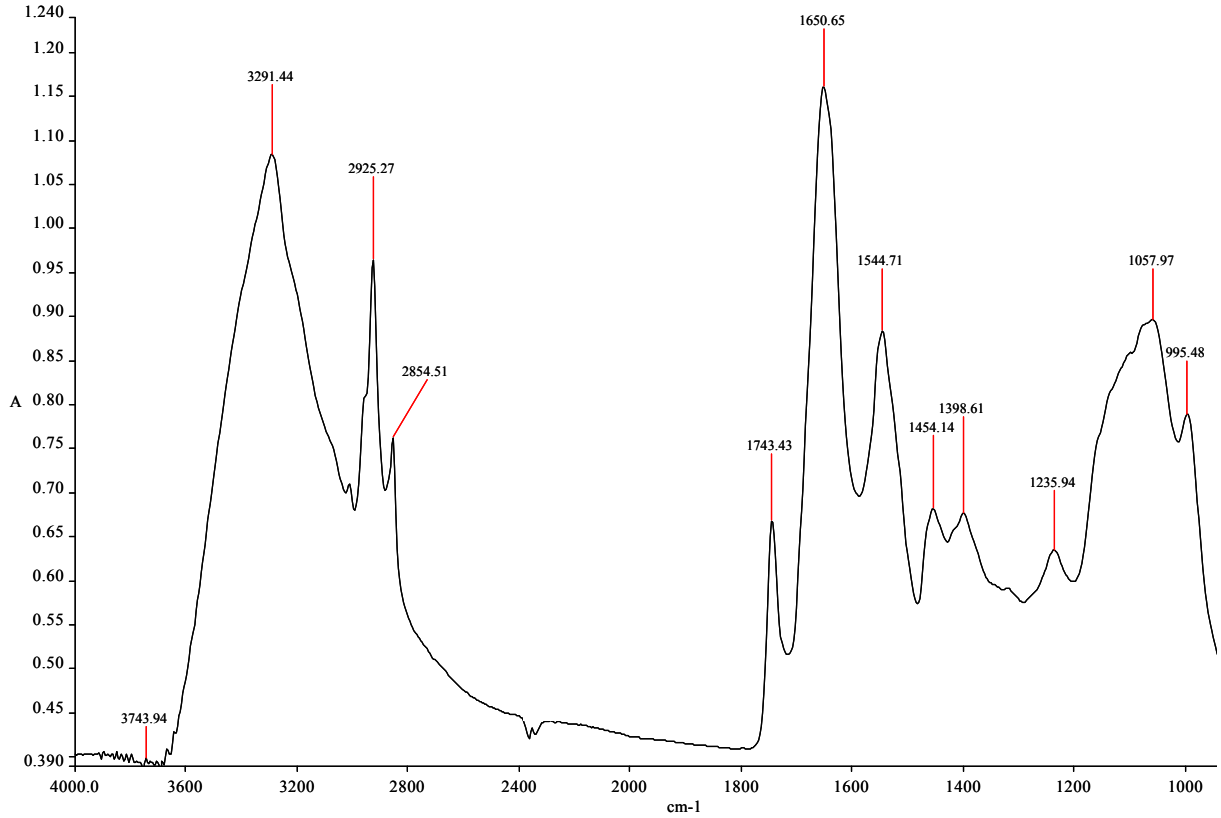

Upon examination of the region 1800-1500 cm^{-1} in the spectrum, first note that the strong band at 1740 cm-1 arises from the carbonyl (ester C=O group) which indicates the presence of lipid. The next two absorption bands that are two primary features of the protein, amide I and amide II bands at approximately 1660 cm^{-1} and 1550 cm^{-1}, respectively. Amide I arises from the stretch of C=O of the peptide group in the protein. The amide II band is mostly from the N-H bending and secondarily from the effect of C-N stretch. At approximately 1469 cm^{-1}, C-H bending vibrations occur. In biological specimens this may represent the carbon chains of the lipid. In the 1100-1025 cm^{-1} region of the spectrum strong carbohydrate bands of starch and cellulose are found. Absorption bands occurring at 1420 cm^{-1}, 1370 cm^{-1}, 1335 cm^{-1} are indicative of the cellulose or hemicellulose in the sample and P=O vibrations occurs at 1235 cm^{-1}.

Heterogeneity can be expected for biological materials. Plant tissue has voids which can increase the scattering losses. All of these effects contribute to baseline shift and slope. Figure1.26 shows a spectrum extracted from a map that has a seriously sloping baseline.

Figure 1.26 A spectrum showing baseline shift due to voids in the tissue.

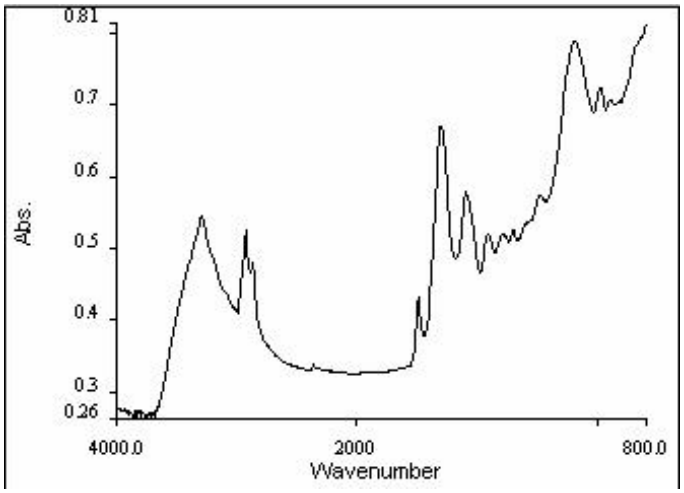

Assignment of the peaks allows us to know which peaks are important for the sample being analyzed. In the spectrum of the scutellum part of the kernel which is rich in lipid and protein, peaks for lipid and protein are predominant and significant for this study.

Figure 1.27 A visible image of wheat kernel cross section and the area mapped in red rectangular and enlarged.

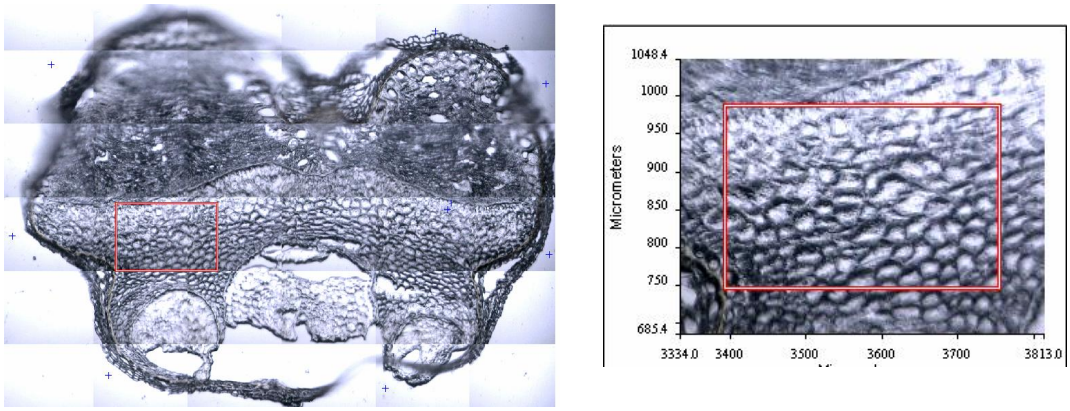

Functional group maps are produced by plotting the intensity of IR absorption bands as a function of the x, y position. These maps show the distribution of a particular constituent in the sections and help define the chemical differences within the specimen. Functional group maps were obtained by calculating the baseline corrected area under the peak.

Figure 1.28 An example of baseline corrected peak area calculation. Left figure shows setting the spectral ranges while right figure shows setting the baseline points.

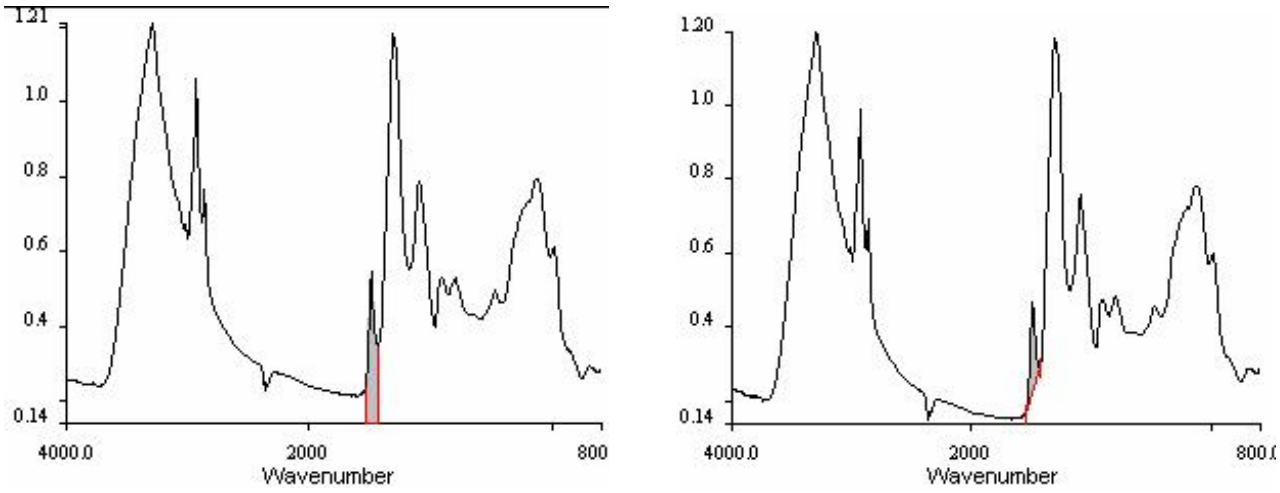

In the figure 1.28, an example of peak area calculation is shown. Firstly, the spectral range is determined. Next, the baseline points are inserted, and baseline corrected peak area is obtained. In the table 1.2 the integrated spectral region and baseline points used for particular peak are presented. These are used for the calculations in this study.

Table 1.2 The spectral region and baseline points used for particular peaks.

Peak (cm^{-1})	Spectral Range Integrated (cm^{-1})	Baseline Points (cm^{-1})
1025	1171-890	1171-890
1550	1583-1486	1593-1486
1650	1713-1605	1715-1592
1740	1767-1715	1773-1715
2927	2994-2842	2994-2817

When the baseline corrected peak areas under peaks at 1740 cm^{-1} and 1025 cm^{-1} were calculated, the functional group maps for the lipid and carbohydrate, respectively were obtained. The 1740 cm^{-1} functional group map shows the lipid distribution in the area previously displayed. The 1025 cm^{-1} functional group map indicates that there is little carbohydrate in the scutellum area.

Figure 1.29 The functional group maps for the lipid and carbohydrate which are obtained by functional group maps at 1740 and 1025 cm^{-1}. The 1025 cm^{-1} functional group map indicates that there is little carbohydrate in the scutellum area.

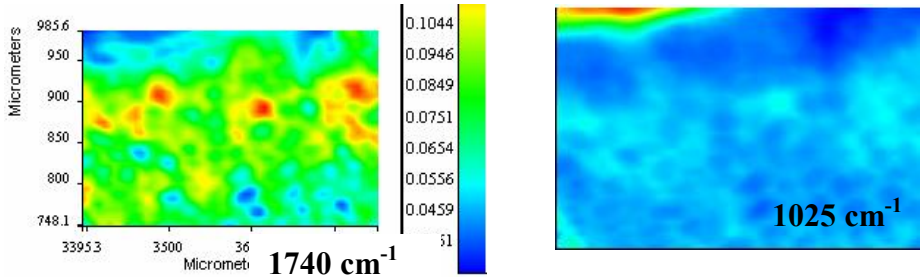

Another figure below shows the amide II protein peak area functional group map for the same section.

Figure 1.30 The functional group map for protein at 1550 cm^{-1} showing the distribution of protein in the scutellum and the spectrum showing the area under the peak .

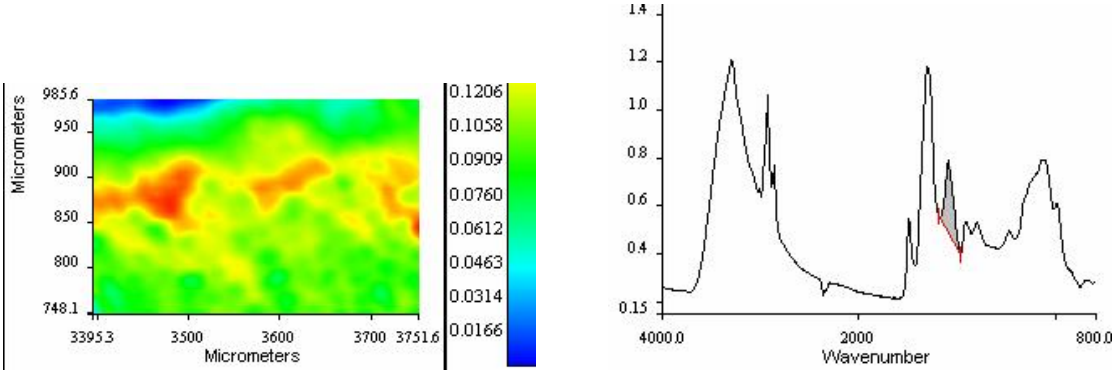

3. Results and Discussion

From data collected in image mode functional group maps and peak area ratio maps were produced to compare the localized spectroscopic differences between of sprouted and unsprouted kernels.

3.1. Results of the experiments performed at NSLS

Based on the assumption that the scutellum storehouse was consumed to provide nourishment for the embryo at initial stages of germination before endosperm reserves are mobilized, this part of the kernel was initially studied spectroscopically. Subsequently the endosperm, within the same sections being compared, was also examined. Change in the lipid storehouse in the vicinity of the embryonic axis was the focus of this study. Biochemical changes were revealed via the lipid/protein band ratio functional group maps within the scutellum (adjacent to the embryo) area.

Figure 1.31 3-D chemical images of the same wheat kernel cross section showing the relative population lipid (a), protein (b), and starch (c). The peak area maps of 1740 cm^{-1}, 1550 cm^{-1}, and 1025 cm^{-1}, respectively, result from peaks marked in red on the lipid, protein, and carbohydrate spectra extracted from the corresponding 3-D map.

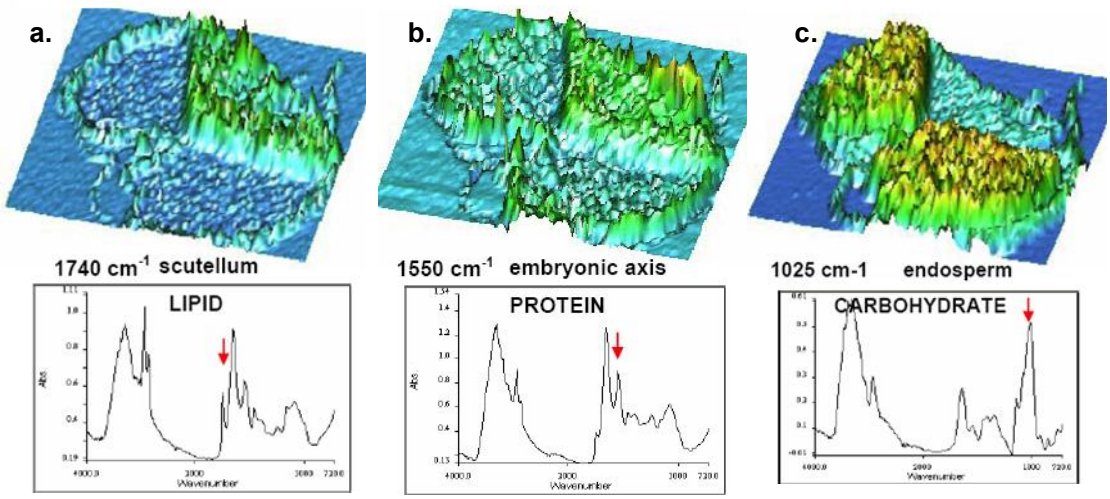

The chemical distribution of the each botanical part is shown with 3-D functional group maps in figure 1.31. Chemical images of unsprouted kernel functional groups are shown for the carbonyl, amide II, and carbohydrate bands respectively. (a) highlights lipid in the scutellum and aleurone cell walls, (b) shows the protein in scutellum and aleurone cells. The protein population is the highest in the embryonic axis. (c) the baseline corrected peak area at 1025 cm^{-1} highlights the carbohydrate in the endosperm. From functional group maps, the protein rich embryonic axis was clearly distinguished from the lipid rich scutellum and both of these botanical parts were readily distinguished from the carbohydrate of the endosperm.

Figure 1.32 Unsprouted kernel 3-D chemical functional group maps of a) the scutellum (lipid) b) embryonic axis (protein) c) endosperm (carbohydrate), also corresponding contrast for each botanical part from select PCA factor maps. All images are from the same imaging data cube.

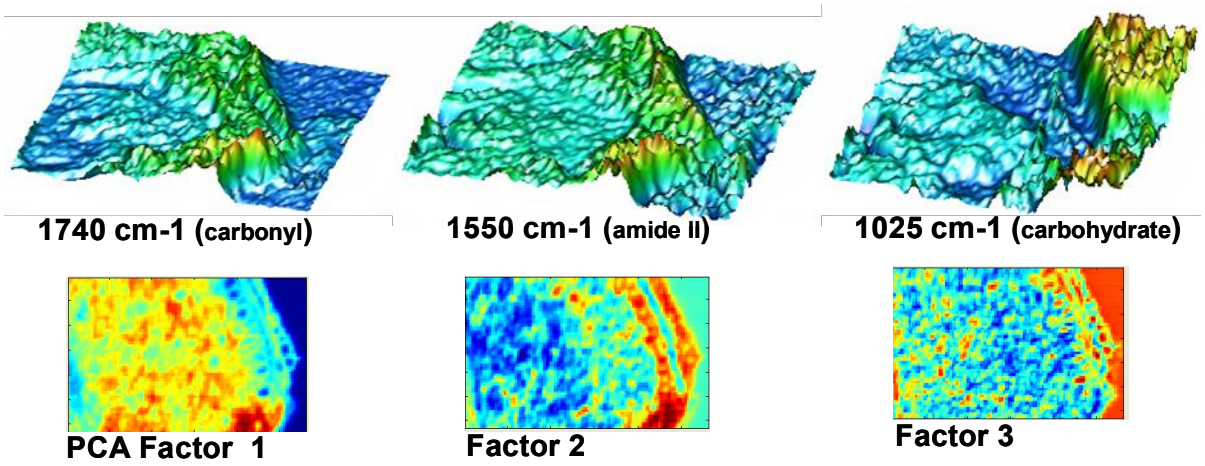

Figure1.33 Sprouted kernel 3-D chemical functional group maps of a) scutellum b) the developed proteinaceous embryo and c) the endosperm next to the embryo that is virtually void with respect to carbohydrate. Note contrast also in corresponding PCA factor images.

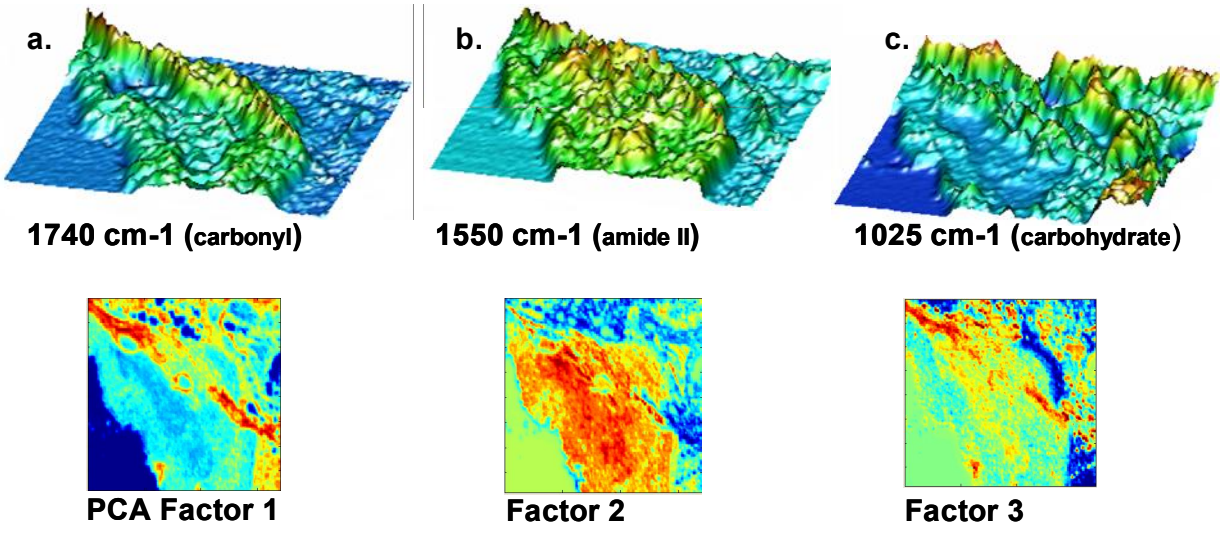

Data for sections of sprouted (36 hr) and unsprouted (3 hr) wheat mapped by mid-IR microspectroscopy are shown in 3-D functional group maps (figures 1.33 and 1.32) for lipid (1740 cm^{-1},carbonyl), protein (1550 cm^{-1},amide II), and carbohydrate (1025 cm^{-1}). False color

contrast for these same areas was obtained from the same raw data applying principle component analysis (PCA) to obtain factor images shown. Figure 1.32 is of the unsprouted kernel. Sprouted kernel functional group maps for the carbonyl, amide II, and carbohydrate peaks are shown in figure 1.33. Note readily the high amide II population in the embryonic axis of figure 1.33 b in comparison to the same corresponding map in the Figure 1.32b of the unsprouted kernel. This shows development of the embryo and the build up of protein as it is developing. The image Figure 1.33a to the left of that embryo exhibits a ridge of lipid that is between the embryo and the endosperm (carbohydrate). The 3-D carbohydrate functional group map (figure 1.33c) to the right of the amide map is a depression corresponding to the location of the embryo. In addition, map at 1025 cm^{-1} indicates a mobilization in the carbohydrate reserves. False color images in the corresponding principle component analysis factors of figure 1.33 show contrast corresponding to these same two botanical parts.

Figure 1.34 Graph showing the population of pixels with higher lipid/protein peak area ratios within the scutellum and embryo region. a) The ungerminated kernel has a higher percentage (66%) of pixels with spectra having a higher lipid/protein peak area ratio greater than 0.6. b) The kernel sprouted for 36 hr had reduced lipid in the scutellum (41% of spectra had a peak area ratio greater than 0.6).

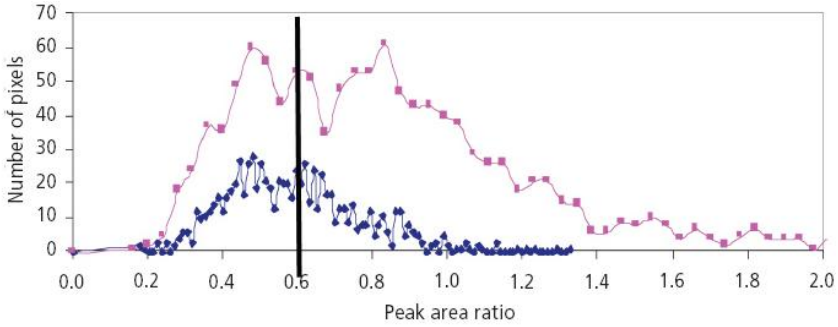

The lipid to protein (1740 cm^{-1} / 1550 cm^{-1}) ratios were calculated from spectra of the pixels extracted from the scutellum and embryo section images of ungerminated (3 hr) and

sprouted (36 hr) kernels of the same variety. Populations of these ratios are shown as graphs (Figure 1.34) for the unsprouted (control) and sprouted (36 hr) kernels, respectively. The ratio mean of 0.98 for pixels from the unsprouted scutellum was compared to a mean of 0.74 for corresponding pixels of the sprouted kernel. These results indicate a shift from the lipid population to a protein population. In the graph (upper) of the unsprouted kernel, 739 of 1160 pixels had absorbance peak area ratios greater than 0.6. The graph (lower) of the scutella from sprouted kernel had only 275 of 823 pixels beyond the peak area ratios of 0.6. These data represent our first attempt at semiquantitation of the change in the chemical balance between these two functional groups.

Figure 1.35 (a) and (b) have three columns each to compare images of sprouted and unsprouted kernels and sections from these kernels. The left columns contain the log 1/R near-IR image of that wheat kernel. Additional images in the same columns are from PCA factors that show developed embryo in contrast to the body of the kernel. In the center column are the mid-IR microspectroscopic images that show the curvature of the developed embryo and adjacent tissue outside of the arc and select PCA factor images. In figure b the geometric features of a developed embryo are absent in all three columns.

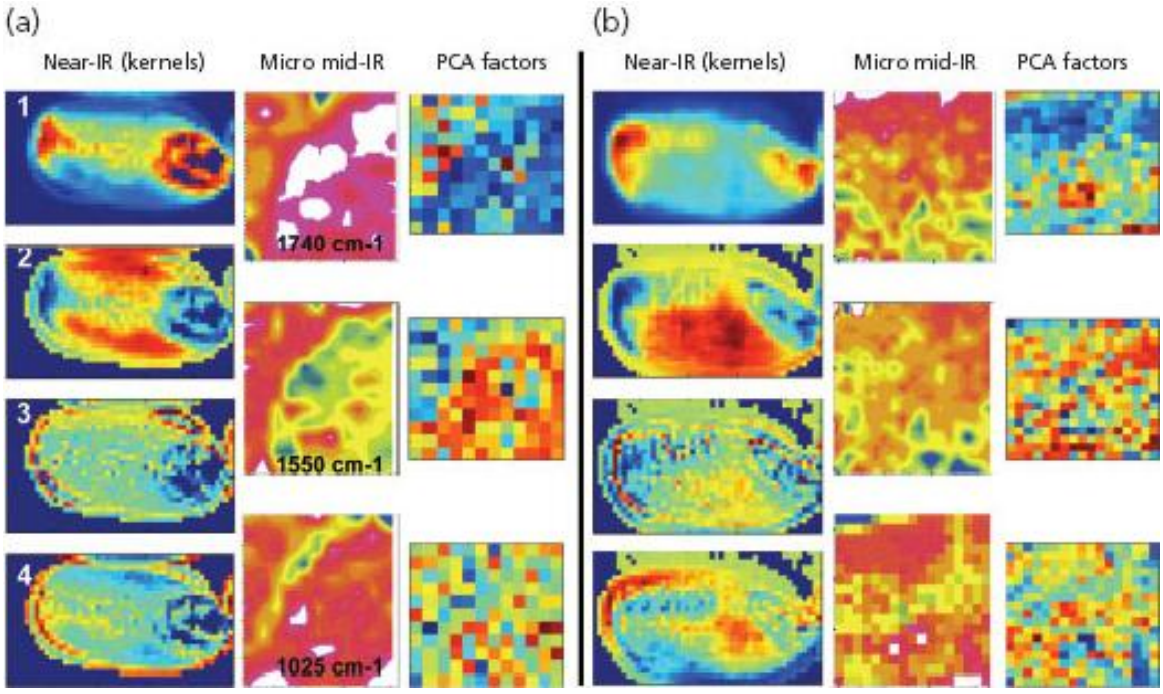

The kernel sections shown in figure 1.35 were produced from whole kernels that had been tested for germination in a separate study designed to nondestructively detect germination by subsurface polychromatic contrast**.** In figure 1.35 a of sprouted and b unsprouted kernels a column of near infrared whole kernel images is shown. In each column the top image is of log 1/R values at a single wavelength for each pixel. Note that the germ area on the right end of the kernel has prominent contrast in figure 1.35 a. In figure 1.35 b there is no evidence of a developed embryo. Whole kernel principle component factor images of the sprouted kernel clearly show evidence of a developed embryo. In contrast there is no such prominent feature in the whole kernel near infrared images of figure1.35b. In figure 1.35a and b to the right of the whole kernel near infrared image columns are shown another column of mid-IR microspectroscopic function group maps at 1740 cm^{-1}, 1550 cm^{-1}, and 1025 cm^{-1}. These images were obtained from sections produced from the previously nondestructively analyzed wheat kernels. The curvature shown in the microspectroscopic images reveal the line of demarcation between embryo (lower right) and the body of the kernel (upper left). This same curvature is observed with select principle component factor maps to the right of the actual mid-IR microspectroscopic images. In contrast, the mid-IR microspectroscopic functional group maps and PCA factor maps of the unsprouted kernel do not show the same degree of order or differentiation between the embryo and the adjacent tissue.

After the preliminary data shown in the preceding figures was obtained, the first attempt to measure the lipid to protein peak area ratios was done with a series of line maps across within the germ area at the National Synchrotron Light Source. To obtain the relative lipid population a number of line maps were carried out with the unsprouted and sprouted kernels representing

several hard wheat varieties. Figure 1.36 shows photomicrographs of two sections with the map lines superimposed.

Figure 1.36 Line map across the germ of unsprouted (a) and sprouted kernels (b). Average lipid/protein values plotted (1.1) are greater for the unsprouted scutellum than the average (0.6) of first five and last five on either side of the sprouted root.

a .

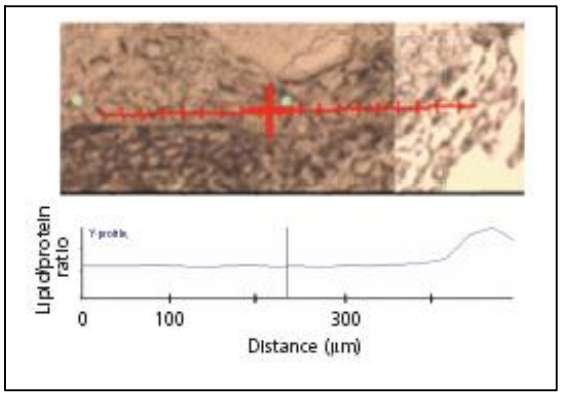

b.

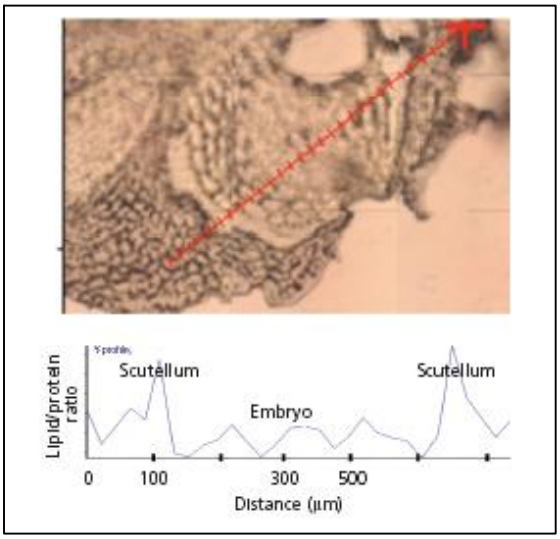

The 2927 cm^{-1} CH_2 stretching vibration peak area was used to represent the lipid, and the 1650 cm^{-1} (amide I band) was used to represent the protein. The ratio average from points 1–15 along the line map for the unsprouted section was 1.1. In contrast, for the sprouted kernel of the same variety, the first and last five points taken on either side of the embryo had an average ratio of 0.6. The early imaging evidence and subsequent line mapping are indicative of the relative population of scutellum lipid in the sprouted kernel to that of the unsprouted kernel. Following these experiments, a series of quantitative experiments was undertaken with scanning maps including 1000-3000 spectra.

3.2. Results of the quantitative experiments done at KSU

In the photomicrograph of a wheat kernel cross section figure 1.37 three rectangles (red) show the actual areas of the scutellum of this kernel from which spectra were collected. An

artist's sketch of a wheat kernel section is included to show the embryo and scutellum within the germ in relation to the other botanical parts.

Figure 1.37 Areas within the scutellum outlined in red on the photomicrograph are those mapped. Note the corresponding botanical parts from the sketch.

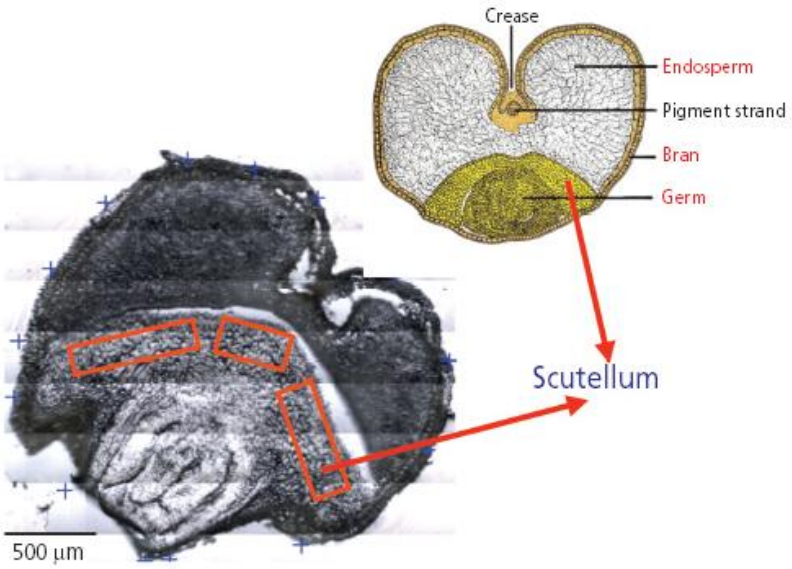

The three sections for sprouted and three sections for unsprouted kernels from each of the varieties Trego, KS2174, and Danby were mapped and lipid to protein band ratio maps were produced by calculating the ratio of the baseline corrected peak areas at the 1740 cm^{-1} and 1550 cm^{-1}. By computing the peak ratio (Figure 1.38) any variations due to thickness differences were eliminated.

Figure 1.38 Lipid to protein peak areas ratioed.

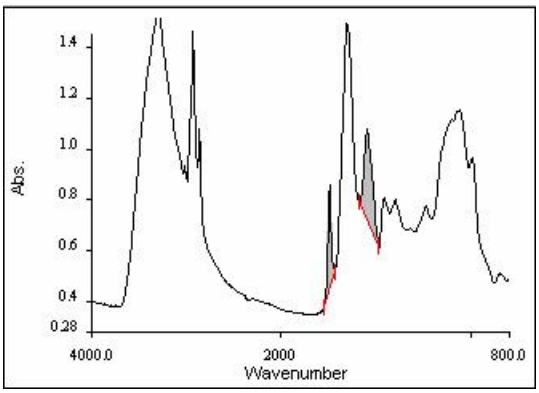

The numerical ratios were assembled in an excel file and basic statistical calculations were performed. The calculated results are reported below. Maximum, minimum and mean values were calculated. Also standard deviations and standard errors for each group were listed.

Table 1.3 Maximum, minimum, mean values, standard deviation, and standard error for Trego control sections.

section	map	area	max	min	mean	std	se	pixels
1	1	1	2.62	0.93	1.56	0.23	0.0078	910
	2	1	1.59	0.77	1.13	0.12	0.0027	2331
2	1	1	1.60	0.55	1.11	0.13	0.0030	1863
	2	2	1.59	0.63	1.06	0.15	0.0040	1300
	3	1	1.53	0.72	1.07	0.11	0.0030	1148
	3	2	1.44	0.56	1.04	0.12	0.0040	855
3	1	1	1.30	0.34	0.81	0.13	0.0030	1705
	1	2	1.44	0.52	0.92	0.16	0.0060	629
	2	1	1.58	0.59	1.01	0.14	0.0030	1716

Table 1.4 Maximum, minimum, mean values, standard deviation, and standard error for Trego germinated sections.

section	map	area	max	min	mean	std	se	pixels
1	1	1	1.03	0.33	0.81	0.09	0.0030	711
	1	2	1.22	0.48	0.87	0.10	0.0020	1512
	2	1	1.29	0.49	0.98	0.12	0.0050	529
2	1	1	1.02	0.50	0.74	0.07	0.0018	1552
	2	1	1.17	0.45	0.81	0.12	0.0050	500
	2	2	1.10	0.53	0.81	0.10	0.0030	896
3	1	1	1.54	0.48	0.84	0.12	0.0050	576

Table 1.5 Maximum, minimum, mean values, standard deviation, and standard error for KS2171 control sections.

section	map	area	max	min	mean	std	se	pixels
1	1	1	1.89	0.62	1.15	0.14	0.0036	1440
	1	2	1.61	0.54	1.14	0.18	0.0091	408
	2	1	2.1	0.62	1.20	0.18	0.0046	1543
	3	1	2.53	0.6	1.13	0.15	0.0039	1452
2	1	1	1.83	0.32	1.03	0.17	0.0028	3366
	2	1	1.82	0.36	1.00	0.16	0.0026	3975
3	1	1	1.25	0.65	1.00	0.08	0.0020	1586
	2	1	1.32	0.62	1.00	0.09	0.0022	1645
	2	2	1.22	0.61	0.95	0.12	0.0039	861

Table 1.6 Maximum, minimum, mean values, standard deviation, and standard error for KS2174 germinated sections.

section	map	area	max	min	mean	std	se	pixels
1	1	1	1.59	0.53	0.98	0.14	0.0029	2247
	2	1	1.50	0.48	0.92	0.14	0.0033	1632
	2	2	1.40	0.43	0.88	0.14	0.0044	936
2	1	1	1.32	0.42	0.86	0.12	0.0024	2448
	2	1	1.55	0.46	0.90	0.15	0.0027	2904

Table 1.7 Maximum, minimum, mean values, standard deviation, and standard error for Danby control sections.

section	map	area	max	min	mean	std	se	pixels
1	1	1	1.63	0.74	1.11	0.15	0.0083	345
	2	1	1.68	0.79	1.16	0.14	0.0079	314
2	1	1	1.17	0.67	0.94	0.10	0.0053	360
3	1	1	2.09	0.40	0.94	0.22	0.0080	774
	2	1	2.51	0.57	1.18	0.30	0.0120	636

Table 1.8 Maximum, minimum, mean values, standard deviation, and standard error for Danby germinated sections.

section	map	area	max	min	mean	std	se	pixels
1	1	1	1.03	0.43	0.71	0.080	0.0025	1008
	2	1	1.10	0.45	0.75	0.095	0.0032	861
2	1	1	1.12	0.45	0.76	0.085	0.0023	1302
3	2	1	1.18	0.40	0.82	0.126	0.0030	1760

Figure 1.39 Photomicrographs of sprouted and unsprouted cross-sections of the variety Trego with the corresponding spectra and 3-D maps. Red boxes indicate the area mapped in these sections.

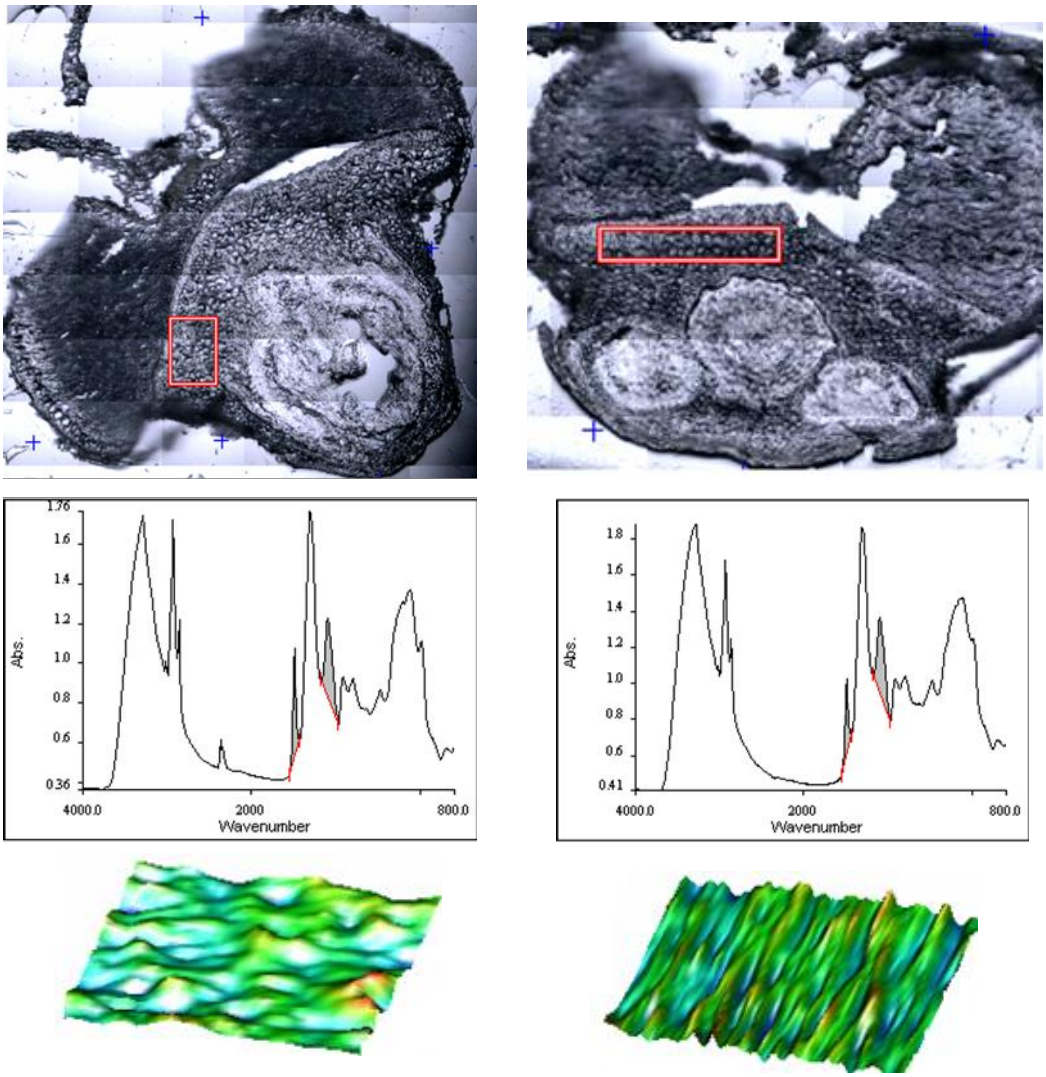

Figure 1.40 Photomicrographs of sprouted and unsprouted cross-sections of the variety KS2174 with the corresponding spectra and 3-D maps.

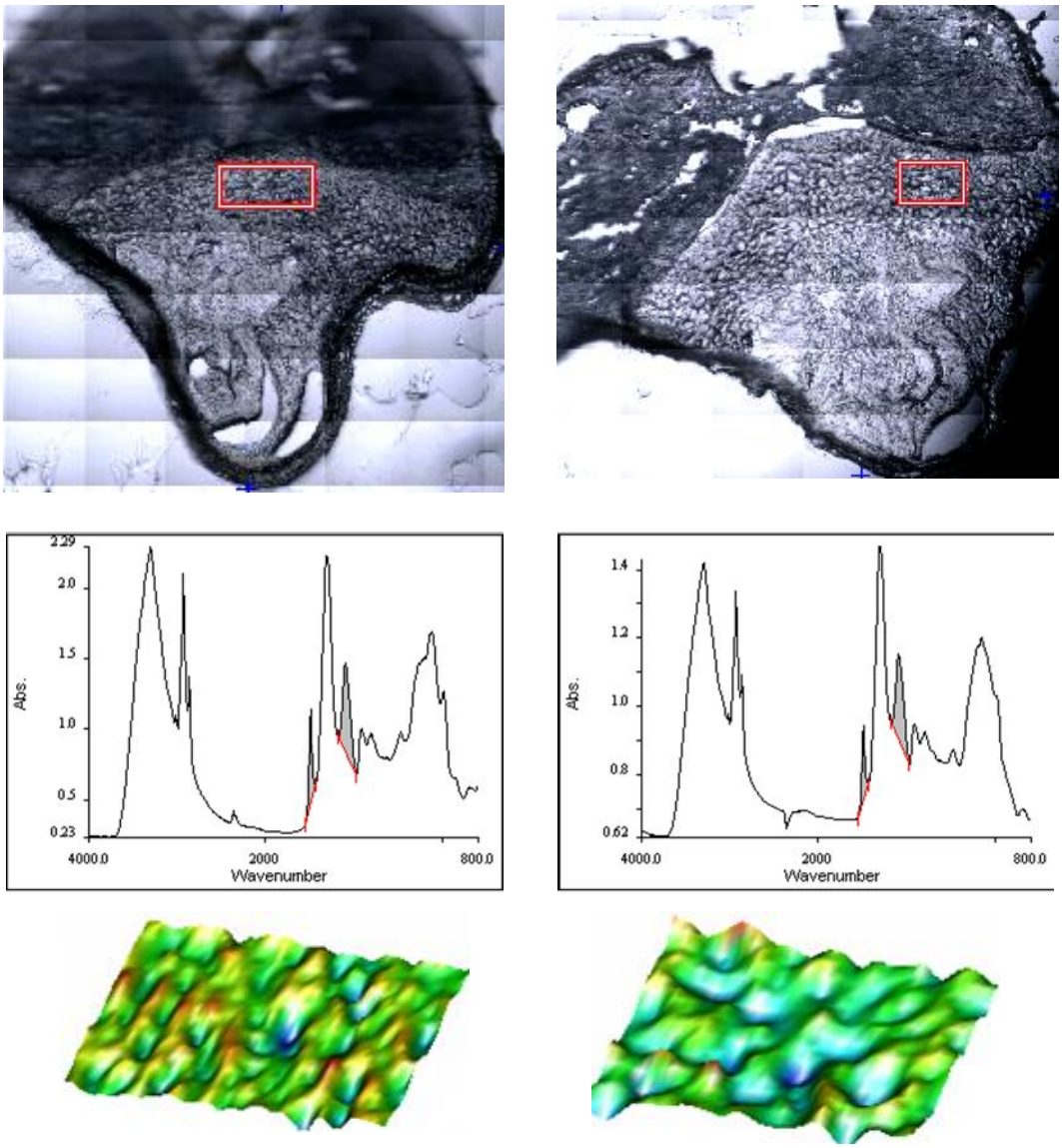

Figure 1.39 and 1.40 show photomicrographs of sprouted and unsprouted cross-sections of the varieties Trego and KS2174 respectively with the corresponding spectra and 3-D maps images, spectra, and maps. Note the difference in the mean ratios between the unsprouted and the sprouted samples. Figure 1.41 has photomicrograph images, spectra, and functional group maps of Danby for sprouted and unsprouted kernel. Quantitative values for the variety Danby appear in table.

Figure 1.41 Photomicrographs of sprouted and unsprouted cross-sections of the varieties Danby with the corresponding spectra and 3-D maps.

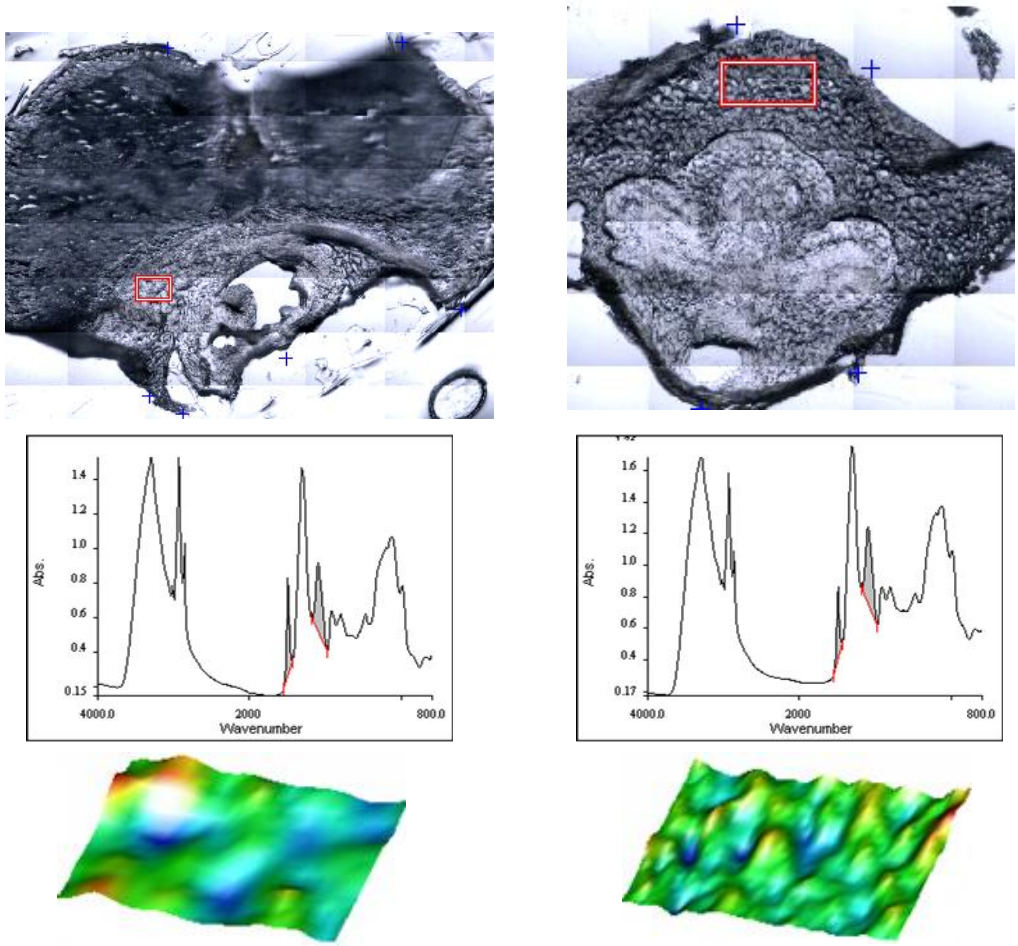

Table 1.9 Tabulated numbers of pixels and the lipid/protein ratio for unsprouted and sprouted scutelli of three different wheat cultivars. Results show averaged spectral differences between 21,374 sprouted and 32,359 unsprouted kernels.

Sample	pixels	max	min	mean	std	se
Trego-0	12,457	1.63	0.62	**1.08**	0.14	0.0041
Trego-24	6,276	1.20	0.47	**0.84**	0.10	0.0035
KS2174-0	17,473	1.82	0.55	**1.08**	0.15	0.0042
KS2174-24	10,167	1.47	0.46	**0.90**	0.14	0.0031
Danby-0	2,429	1.82	0.63	**1.07**	0.18	0.0083
Danby-24	4,931	1.11	0.43	**0.76**	0.09	0.0028

The data tables for three cultivars provide quantitation from 53,733 spectra obtained from 31 maps collected from 17 sections (Table 1.9). Each variety was represented by both sprouted and unsprouted kernels. In all cases, it was observed that the lipid to protein ratio is greater than 1.0 in the unsprouted and significantly lower than 1 in the sprouted kernel sections. A total of 32,359 spectra from the scutella of unsprouted wheat were compared to 21,374 spectra from sprouted wheat. From all these numerical data, the grand mean showed a 23% reduction of the lipid-to-protein ratio in the scutellum resulting from the germination process.

The reduction in the lipid to protein ratio can be caused by the depletion of the scutellum to provide energy for the growing embryo. Another reason, it may be due to increase in the starch and protein which are transferred from endosperm for the growing embryo. Swift and O'Brien (1972) found that after 24 hr large masses of partly hydrolyzed proteins are formed by coalescence of the bodies in the scutellum. There are controversy studies regarding the lipid consumption. Swift and O'Brien (1972) found that after 24 hr; they became less common near the cell membranes of the epithelium cells. In the later stages of germination, there is a reduction in their number, however their utilization is slow. In some studies, it has been suggested that the starch in the scutellum is derived from the lipid bodies. Tavener and Laidman (1972) observed that triglyceride reserves were degraded progressively. Further investigation is needed to explain the biochemical changes during germination. Other than scutellum, embryonic axis and endosperm of the kernel should be studied to explain the observations better.

4. Conclusion

The germinated kernels selected from nondestructive Near-IR imaging experiments were sectioned for synchrotron Mid-IR microspectroscopy. Mid-infrared functional group maps of sections highlighted kernel morphological structures in the germ area based on the predominance

of the embryo's protein chemical composition. PCA factor images also highlighted the select botanical parts including the scutellum, embryonic axis, and endosperm. Sprouted kernels were distinguished from unsprouted one of the same variety. A reduced lipid population was observed in the scutellum next to the developing embryo in the 1740 cm^{-1} (carbonyl) functional group 3-D image in comparison to that of the ungerminated (control) kernel. Semiquantitative comparison was made on a subsequent synchrotron line maps. This comparison was between pairs of sections of germinated and ungerminated kernels from the same lot representing multiple wheat cultivars. The lipid/amide I ratio was calculated for spectra of individual pixels from line maps across the germ area. These data supported previous observations from 3-D chemical images. Finally, based on the preliminary synchrotron work carefully prepared sections, representing three germinated cultivars and their ungerminated controls were imaged at the Kansas State University Microbeam Molecular Spectroscopy Laboratory with a Spectrum Spotlight 300 (Perkin Elmer, Shelton CT) with a 6.25 μm x 6.25 μm pixel size. Fifty three thousand spectra (32 K unsprouted and 21 K sprouted) were compared. An average 23% reduction in lipid/protein was observed. These data were obtained from 31 maps collected from 17 sections involving six different kernels. For each map the scutellum lipid population of the sprouted kernel was compared to that of a corresponding unsprouted (control) kernel. The numerical lipid/protein ratios were consistent. A reduction of scutellum lipid as a result of the early germination process can be caused by the depletion of the scutellum to provide energy for the growing embryo.

PART 2 - EARLY NONDESTRUCTIVE DETECTION: NEAR-INFRARED CHEMICAL IMAGING OF WHEAT GERMINATION TO ASSIST PLANT BREEDING

1. Introduction

Germination of the kernels in the ear before harvest that may occur when there are unfavorable humid conditions is known as preharvest sprouting. Cereal growing regions of the world where there is high probability of rain during harvest are liable to preharvest sprouting such as Eastern Europe, Chile, Argentina, Brazil, South Africa, Australia, and Manitoba in Canada. In the US, the Pacific Northwest states are examples of places that have suffered some years from this problem (Derera, 1989). The changes in chemical components of the wheat kernel with the germination process have detrimental effects on the end use of the wheat and cause important economic loses to the farmers. These detrimental changes are referred as preharvest sprout damage (8). Preharvest sprouting results from the lack of dormancy. Tolerance to preharvest sprouting and embryo dormancy are highly desirable characteristics that plant breeders study (9).

1.1. Sprout Damage

Rainfall during harvest may cause different degrees of damage depending on variety, maturity level, the temperature and the exposure time to unfavorable weather conditions (8). The harmful effect of the sprout damage can not be eliminated. Interest in white wheat is increasing in current breeding program because it gives the possibility of increasing flour yield without affecting the color, and offering health benefits from retained antioxidants. Wheat growers are reluctant to grow white wheat that is subject to sprout. Historically, white wheat was considered

highly susceptible to sprout damage (25). Current breeding programs strive to limit sprout susceptibility.

The preharvest sprouting damage affects the quality the cereal-based products such as bread, pasta, and beer adversely. With the increase of sprouting dough rheological properties measured by Farinograph are weakened and bread quality is degraded. Because of the excessive enzymatic hydrolysis of the starch, water absorption, gas retention, dough handling and texture of the product are affected, dough becomes stickier (damaged starch holds large water). In addition changes in gluten proteins by hydrolytic enzymes are effective (22). Bread prepared with spouted wheat has lower loaf volume and sticky crumb (51).

1.2. Sprout Tolerance

A significant agronomic objective of the breeding program is improving the resistance of a new variety to preharvest sprouting. Such resistance can originate from the grain itself or it can be caused by the non-grain ear components. Resistance associated with grain itself is generally due to the dormancy of the grain. Dormancy retards or delays germination of the seed under favorable conditions. There are two types of dormancy; it can be external which is seed coat imposed or internal embryo related dormancy. Seeds may develop with different levels of primary dormancy at harvest maturity. The relationship between dormancy and germination is shown in the figure 2.1 (52). Secondary dormancy which prevents germination after imbibititon of water can be induced by water stress, anoxia, or hypoxia (too much or too little oxygen) or temperature extremes (5, 7, 53).

When applying germination tests the viability should be verified. Kernels that fail to germinate for reasons other than dormancy may thus be excluded (11). Red wheat varieties have historically been more resistant than white wheats (54). Andreoli et al. (9) reported the two major

genes which control the dormancy and stated that there is no maternal tissue influence. Miura et al. (55) identified chromosomes carrying genes for seed dormancy. Mares (52) studied preservation of the dormancy of wheat after harvest. It was shown that during the post harvest storage of the freshly harvested grain in an air-conditioned seed room maintained at 12ºC, the dormancy disappeared in 10-14 days for the partially dormant varieties and in 2.5-3 months for the strongly dormant varieties. In contrast, when kernel was stored at -15ºC, dormancy was preserved and germination characteristic were the same as those of freshly harvested wheat.

Figure 2.1 Dormancy and germination (reprinted from ref. 17b)

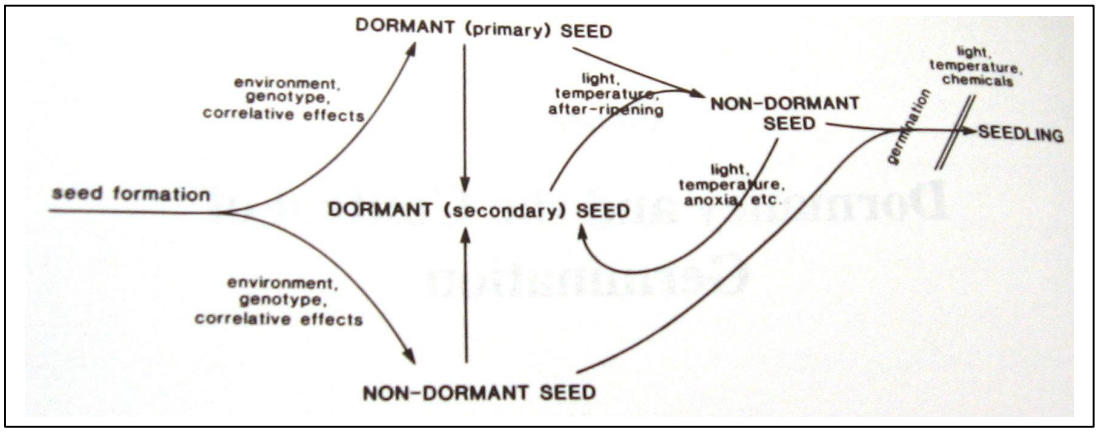

The breeding of dormant varieties requires the breaking of dormancy because they do not germinate if planted immediately after harvest. The application of gibberellic acid and chilling to 4ºC can be used to break the dormancy to breed wheats with preharvest resistance (54).

1.3. Determination of Sprout Damage

An objective, reliable, and reproducible test is a requirement to assess the spout damage for different purposes from the point of views of grain growers and grain buyers. Unreleased test lines should be tested for the tolerance to preharvest sprouting.

1.3.1. Visual assessment (naked eye)

Visual inspection is the only non destructive method among sprout damage tests. Visual inspection can be done on the kernels, and breeders and grain inspectors count the percentage of kernels which are visibly sprouted. This method has low sensitivity and discrimination power compared to objective methods (11, 56).

1.3.2. Viscosity methods

The viscosity methods are destructive and applied to ground wheat or flour. In these methods, instruments are used to measure thickening the starch-water suspension by heating to its gelatinization temperature during mixing. Enzyme action decreases the viscosity of the suspension. There are uncontrolled sources of variation due to natural differences in pasting properties of starches (57). Waxy wheat with higher amylopectin content has low Falling Number (FN) although enzyme level is not increased (58). All these methods are destructive and not applicable to single kernels, they require bulk of samples. In addition, they are not sensitive enough. Low FN in the absence of germination can be observed due to high enzyme level from improper development, late maturity alpha amylase (25, 11, 58).

Amylograph: The AACC approved Brabender amylograph method is most sensitive to the sprout damage compared to other viscosity tests. Amylograph is a viscometer that measures the α-amylase effect on flour paste viscosity as a function of temperature. Total test time is between 60-90 min (25, 11).

Falling Number: The AACC approved falling number method is developed by Hagberg (1960) and Perten (1964). After mixing of the suspension in the viscometer; plunger is raised and allowed to fall down. The time required to fall a certain distance is measured in seconds. The

falling number for a sound kernel is high (450-550 sec), with the sprout damage and accompanying increase of α-amylase levels, the falling number decreases (minimum 60 sec).

Rapid Visco Anayzer (RVA): This method was developed as a quick, simple test suitable for field. This method gives results equivalent to the falling number test. The slurry of milled grain and water is heated and stirred (58).

1.3.3. Enzymatic methods

Direct Assay of α-Amylase activity

The viscosity measurements show the extent of interaction between α-amylase activity and its substrate starch. Direct assays measure the α-amylase activity on a substrate; depend on the separation of the enzyme from the sample. Since an added substrate was used, the result is less dependent on the variations of endogenous starch properties (58).

Light Scattering: One of the techniques is nephelometry, where the rate of decrease in light scattering, nephelos (turbidity) of a β-limit dextrin solution is recorded (191 Grain Amylase Analyzer, Perkin Elmer). It increases linearly with the amount of the enzyme.

Colorimetric: A dye-labeled starch substrate can be used to determine the enzyme activity. Dye molecules are incorporated into starch by covalent bonding, during the starch digestion dye releases into solution and color is measured as an indication of α-amylase activity (25, 11).

Fluorescence Method: Fluorescent substances are used to determine the enzymatic reactions. A fluorochrome has been applied to study the germination of the cereals by Carlsberg Research Center, Denmark (11).

Other enzymes: In addition to alpha amylase, the other enzymes that are produced in germination can be used to determine sprout damage.

1.3.4. Immunological Field Test Method

The enzyme-linked immunosorbent essay (ELISA) test kit test was developed in order to determine sprout damage rapidly in the field. It is a colorimetric test based on the detection of α-amylase enzyme by specific antibodies. In the test, the extract of the grain is mixed with the anti-amylase reagent and a color-developing antibody. The degree of the damage is determined by the intensity of the developed color in a few minutes by the sandwiching the extracted enzyme between labeled and immobilized antibodies. This test determines the presence of the α-amylase, not the activity (58, 59, 60).

1.3.5. Other methods

Density: Donelson et al. (57) developed a detection method for preharvest spouting by using a pregelatinized starch substrate and centrifugation. In the method, increased alpha amylase activity hydrolyses the pregelatinized starch causing a reduction in the weight of centrifugate. It is a microtest, 0.3 g of sample and 0.2 g pregelatinized starch are used. Method is more sensitive to low levels of α-amylase.

Near-IR Analysis: There have been attempts to destructively predict sprout damage with near-infrared (51, 61, 23, 62) correlated to standard enzymatic or viscosity tests (for details see appendix)

Note:

Even in the absence of visible spouting in some cases, the production of α-amylase due to early stages of sprouting, may cause processing problems. Therefore a sensitive test method is needed. Until now, the methods for determination of sprout damage have been destructive and not necessarily sensitive (63).The only previous nondestructive way has been visual assessment which cannot detect the germination before 36 hr. The nondestructive and sensitive chemical

imaging approach to detection of germination in intact wheat kernels was recently introduced, in a 2006 article entitled "Chemical imaging of intact seeds with near-IR focal plane array assists plant breeding" (63).

1.4. Near-IR Spectroscopy and Imaging

Near-IR (750-2500 nm) region of the spectrum are composed of combination and overtones of the fundamental stretching and bending vibrations which are not intense and sharp in comparison to mid-IR region with sharp, strong fundamental vibrations. Bands are broad and weak, they occur at higher frequencies than fundamental vibrations. Molar absorptivities are low, reasonably linear, and follow Beer's law; therefore near-IR is more suitable for the quantitative analysis. The near-IR technique is rapid and nondestructive. It is very suitable for online applications and has many applications in a number of industries because there is no requirement of sample preparation.

Low absorption bands provide a better penetration below the surface. Near-IR imaging with deeper penetration of shorter wavelengths provides subsurface polychromatic contrast (35). Near-IR imaging gives answers to the questions "What", "How much", and "Where" by quantitative and spatial distribution identification of the chemical species in a sample. Near-IR imaging can be applied in various areas such as non-destructive determination of pharmaceutical tablet component distribution and concentration, determination of particle size and uniformity, and distribution of components in mixtures.

At present, there are scanning and discrete wavelength instruments. Initially, several interference filter based instrument were commonly used. Slow scan, grating monochromators, and rapid vibrating grating instruments were built. Random wavelength access and rapid response photodiode detectors (InGaAs) have been introduced and enhanced the data acquisition

speed. Electronic wavelength switching instruments include acuosto-optic tunable filter (AOTF) (64, 64a), liquid crystal tunable filter (LCTF) (65), Hadamard Transfer (HT-IR) (66), and diode array spectrographs (67) (67a).

Common Near-IR imaging systems are recently available in 1100-2400 nm region with FPA detectors and with a liquid crystal tunable filter (LCTF) or a FT spectrometer. Budevska (31) reported studies on near-IR imaging. Very near-IR imaging studies were carried out in the silicon photoconductive region of 700-1100 nm by Taylor and McClure (1992) with a CCD camera and narrow band interference filters. The distribution of the chlorophyll and moisture in plant material was examined. Sugiyama (68) accomplished the visualization of sugar content of melon with a CCD camera and a single interference band pass filter. Near-imaging of the insect detection inside wheat kernel was reported at two wavelengths (Ridgeway and Chambers, 1998) by using with photoconductive vidicon camera.

A liquid crystal tunable filter based instrument was introduced by Spectral Dimensions / Malvern (Columbia, MD). It can operate with either InGaAS or InSb photovoltaic detectors. The InGaAs operated in the 1100-1700 nm wavelength range while InSb operates in the 1200-2400 nm range. This technique was applied to detect germination of wheat kernels nondestructively (63), for bacterial identification (69), and for analysis of pharmaceutical tablets (70, 71). In addition to the liquid crystal tunable filter based instrument of Spectral Dimensions / Malvern (Columbia, MD), a FT-Near IR instrument with fast-recovery NIR deuterated triglycine sulphate (FR-NIR-DTGS) detector for transmission and indium gallium arsenide for reflection FPA is produced by Perkin–Elmer (Danbury, CT). The Microbeam Molecular Spectroscopy Laboratory at KSU work is ongoing near-IR in imaging of the cereals and other biological materials.

Bands in the Near-IR region of the spectrum are overlapping and it is therefore more difficult to interpret and assign the bands than in the mid-IR region. The vibrations of light atoms with strong molecular bonds are predominantly seen in this region (72). When the atoms are heavy and the bonds are weak, then the frequencies will be low, and overtones are not detectable above baseline in the near-IR. Because of this reason, mainly bonds containing hydrogen atoms attached to O, N, and C atoms can be observed. In near-IR spectroscopy of the solids, the analysis is based on mostly diffuse reflectance (73, 74). When the light bounces off a smooth polished surface, the angle of reflection will be equal to angle of incident. This type of reflectance is called as specular reflectance. The specular reflectance is increases with the absorption. The objects in the life are not very flat or polished; they have rough surfaces and show diffuse reflectance. The angle of the reflection is not equal to angle of incident; there is a change in the direction of the reflection. When light enters through a sample, it is scattered within the body and incident light interacts with sample in several modes. The succession of events scatter-absorbs, scatter-absorb, scatter-absorb takes place, and finally a portion of it scatters back from the body of the sample. This is called diffusely reflected light and diffusely reflected light is picked up by the detector (Figure 2.2).

In diffuse reflectance the path length is not well defined. It changes inversely with the absorptivity of the sample. In classical DRIFT spectroscopy, a Kubelka-Munk function is used the make the spectral response linear with concentration. $f(R_\infty) = (1- R_\infty)^2 / 2 R_\infty = K'C$

Where R_∞ is sample reflectance at infinite depth (nonabsorbing matrix), K' is proportionality constant, C is concentration, $f(R_\infty)$ is pseudoabsorbance. This equation gives a reflection inverse log function. K' is based on the ratio of absorption coefficient to scattering coefficient.

If absorption is strong compared to scattering as it is in the mid-IR region, then a nonlinear relation between reflectance and sample concentration is obtained. In such case the specimens are diluted with KCl and the K-M function is plotted. When the diffuse reflectance mode is applied to near-IR where the scattering is very strong and the absorbance is relatively weak, quantitative measurements are obtained without K-M function. In this case, empirical relationship and multivariate statistics eliminate the need for dilution and K-M function offer no benefit.

Figure 2.2 Various pathways of diffuse reflectance (reprinted from ref. 72)

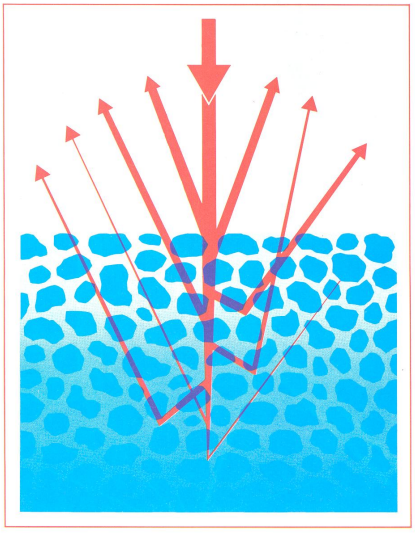

2. Experimental

2.1. Instrumentation

The data in this study were collected with the commercially available chemical imaging system Matrix^{TM}NIR and Sapphire™ NIR of Spectral Dimensions/Malvern (Columbia, MD, USA) which was equipped with a 320 x 256 pixel indium gallium arsenide (InGaAs) and indium antominade (InSb) focal plane array (FPA) detection systems, respectively. With the lens used,

each detector element produced a nominal pixel size of 38 µm x 38 µm. The imaging system include a liquid crystal tunable filter (65) for electronic wavelength switching and appropriate optics to preferentially capture diffusely reflected light from each specimen (Figure 2.3). Kernels on the polished mounting plate were illuminated with four tungsten source lamps and background of specularly reflected radiation was directed away from the collecting lenses. Optical design of the instrument allows changing the magnification with different lenses. ISys™ chemical imaging software package version 4.1.1, provided by Spectral Dimensions/Malvern, enabled simultaneous processing of spectra of 81,920 pixels in a single field of view. The sample mounting plates were designed specifically for the nondestructive testing of multiple kernels and were locally custom-made for prepositioning the thirty kernels in the field of view of the commercial imaging system used.

Figure 2.3 Schematic of near-IR imaging system

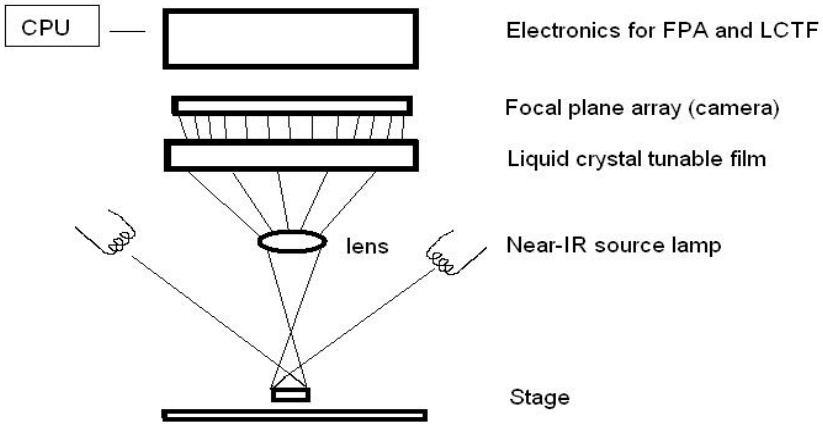

Immediately after instrument start-up, the program performs an initialization step during which the instrument was checked and fine tuned for the best quality and reproducible data. Data collection was carried out with the data acquisition program (SapphireGo) provided with

the system. Data were acquired in the spectral range 1200-2400 nm at 10-nm intervals and 16 images were co-added per wavelength. The field of view (FOV) of 46mm x 35mm providing a magnification of 125µm / pixel was used in this experiment to image 20 kernels simultaneously. With a different lens in the system, a FOV of 12.8 mm x 10.2 mm, corresponding to a nominal of 40 µm x 40 µm pixel size, was used in preliminary experiments to analyze with greater detail two kernels in the same field. The data were collected in the diffuse reflection mode. In diffuse reflection, the radiation from the near-IR source incident on the sample surface, enter the specimen and is diffusely reflected from the sample in all directions. The lenses of the FPA imaging spectrometer collect the scattered radiation. After the initialization step, firstly, dark and bright background data cubes were collected, and then samples in the field of view were focused and scanned. A dark data cube is obtained by scanning a high specular reflectance material (a metal mirror) and a background cube is acquired by a high diffuse reflectance material (an appropriate size of white ceramic plate covering the FOV completely). Each data cube contains 81,920 spectra and is acquired in 4-5 min. These data cubes are three dimensional images which combines the spectral and the spatial dimensions. Two axes represent horizontal (x) and vertical (y) are spatial dimensions and the third z axis contains the spectral dimension (wavelength) (Figure 2.4). These 3D image data cubes enable us to access the complete spectrum of each pixels as well as spatially resolved intensities for all pixels at selected discrete wavelengths.

Figure 2.4 Representation of 3D image data cube with three axes (from ref. 75).

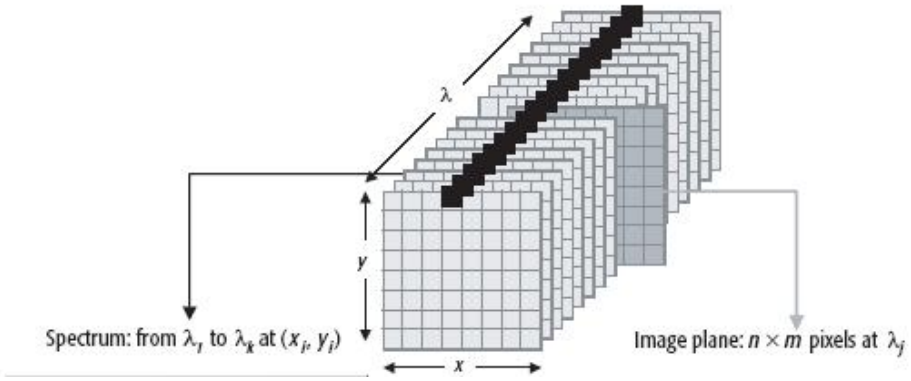

Figure 2.5 An example image of wheat kernels at 2100 nm and spectra representing the germ and the endosperm areas.

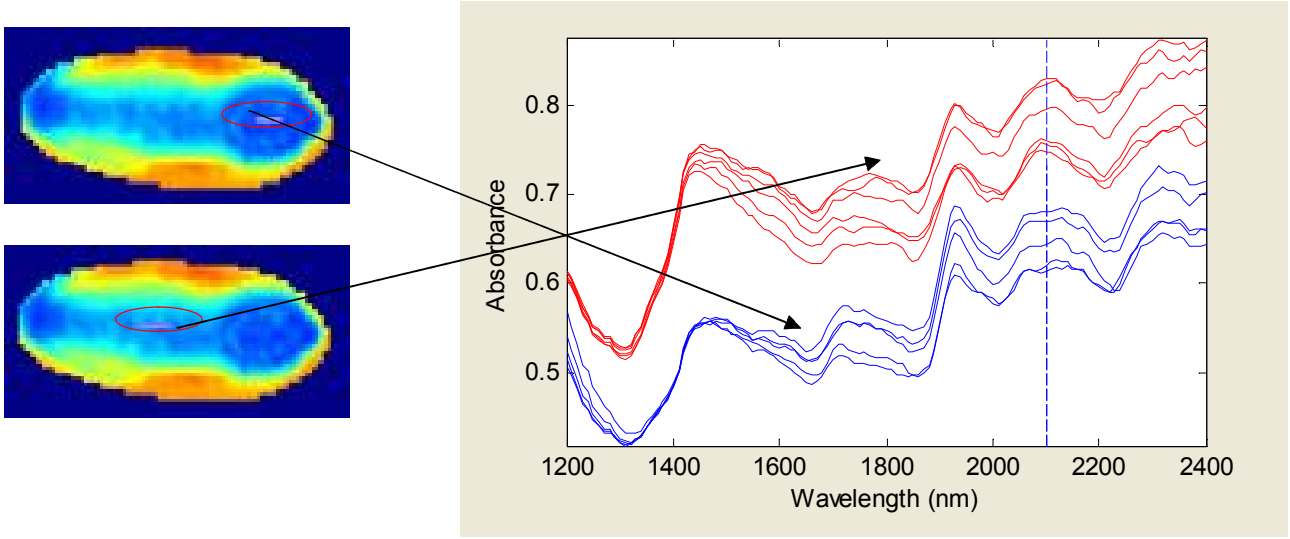

2.2. Sample preparation

The previous experiments were performed with the MatrixNIR™ Chemical imaging system (Spectral Dimensions/Malvern, Columbia, MD) which has an InGaAs FPA. Six 100-g replicates of seed of each variety were germinated for 3, 6, 12, 24, 36, and 48 hr on soaked blotter paper in petri dishes. The kernels were frozen at -80°C for 24 hr to stop all germination processes. The kernels were subsequently freeze dried (48 hr to remove all moisture and to stabilize the kernels) until no weight change could be detected in order to reduce moisture

specifically to avoid further germination at ambient temperature prior to near-IR imaging. The procedure was described in our earlier paper (63). Kernels were manually placed on a grid sample plate for imaging. Each plate had a 5 x 6 grid of slots (Figure 2.6). A set of three such plates was used to image 90 kernels of each lot.

The following experiments were done with Sapphire NIR™ of Spectral Dimensions/Malvern (Columbia, MD, USA**)** which was equipped with indium antominade (InSb) FPA. Wheat kernels of each variety (Danby, Betty, Jagelene, Overley) were germinated for 3, 12, 24, and 36 hr on moist blotter paper (moistened with 6-7 ml distilled water) in Petri dishes. After germination, the kernels were removed from Petri dishes; surface moisture was removed with paper towel. Kernels were mounted onto plates and this step allowed them to dry for 30 min-45 min. After mounting, they were scanned. Kernels were frozen at -80°C for 24 hr to stop all germination processes. Following termination of the germination process, the kernels were dried under vacuum at 55ºC for 3 hr to reduce moisture. Drying was done specifically to avoid further germination at ambient temperature prior to near-IR imaging and also to avoid the masking effect of the water peak on the starch and protein bands. For these experiments, 20 seeds were mounted on each plate (Figure 2.6). A set of three plates was used to image 60 kernels of sample for each time period of exposure to moisture.

Figure 2.6 Sample plate

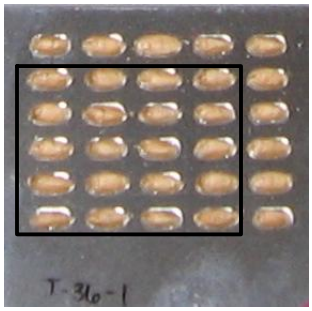

Experiments with InGaAs Focal Plane Array

Reflectance data was obtained from collected raw image data (Reflectance = (Sample-Dark)/ (Bright-Dark)). The reflectance sample data cube was converted in absorbance units by A =log 1/R. It was spatially masked to separate kernels from nonsample area by removing the pixels of radiation specularly reflected off the polished stainless steel plate, on which seeds had been mounted with the germ up. From the remaining pixels, optical parameters such as log 1/R images, as well as principle component analysis (PCA) factors were selected to produce best image contrast. The main objective in imaging was to produce contrast that would distinguish the embryo developing within the germ of each individual kernel from the response of the same factor within the bulk of the kernel. A GO/NOGO determination was made for individual kernels, and the summation of the GO kernels of the germinated group indicated the sensitivity of the test.

Near-IR rays in the 1000 nm-1700 nm range detected by the InGaAs focal plane array penetrated below surface of the kernel to enable probing of the developing embryo and its surrounding scutellum within the germ. Visible light rays can not penetrate below the surface of the germ; therefore naked eyes can not see internal biological development during the process before the emergence of a sprout.

From the mounted seeds, a model germinated kernel (36-hr treatment) and ungerminated (3 hr) was selected. Each model image was masked spatially to remove adjacent background pixels so the remaining pixels would exclusively represent diffuse reflectance off of the individual kernel. To obtain log 1/R, it was necessary to invert the raw reflection intensity values and apply a log function to achieve an image of the kernel for each pixel represented by a value of log 1/R. In the new data cube, each pixel has an individual whole range spectrum. The

response summation of all the pixels in that data cube is shown as a histogram, in which log 1/R appears on the X axis (Figure 2.7). In order to remove most of the background, those pixels having a log 1/R of more than 0.7 were deleted. These represent specularly reflected light that is not directed toward the camera, but reaches there as stray light. At the low end of the log 1/R scale, spurious results of lone pixels that are detached on the histogram from the bulk of the pixels were also removed.

Figure 2.7 Histogram showing the pixel population of various intensities at 1680 nm

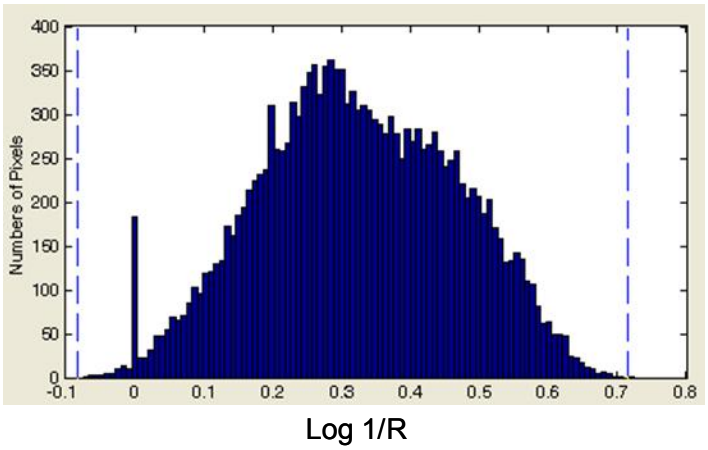

From the typical spectra taken from the data cube of log 1/R, different wavelengths were selected while observing the image in order to optimize wavelength choice for the maximum contrast. In working with the InGaAs array, the C-H near-IR band at 1680 nm was chosen to represent the region where organic material showed a maximum density and gave the highest contrast.

Processing reflection intensity raw data cubes without inversion or producing a log function was accomplished as follows: after cropping the background pixels so that the major image was of the kernel, a histogram was produced in which the axis represented reflection intensity. In this case pixels with reflection intensity below 0.08-0.10 were deleted, and

spurious, highly intense pixels separated from the body of the histogram were also deleted. Principle component analysis (PCA) was applied to reflection intensity values of the resultant new data cube with ISys^{TM} software. PCA, images of individual factors were displayed. Factor 1 was usually the most revealing, however, other factors, including 3, 4, 6, etc., showed the embryo in contrast to the rest of the body of the kernel. In general, when judging multivariate evidence of germination, three images were considered. Contrast between the intensity of diffusely reflected radiation from the germ was compared to that from the bulk of the kernel. Second, the more-or-less round shape indicating an embryo was examined as an intact internal feature. Third, the size of the internal round portion was an indication of the extent of development of the growing embryo. In all instances, false colors were used to show contrast.

In all cases the imaging data cube of the model unsprouted kernel and of the model sprouted kernel were treated in an identical way. Thus, the maximum contrast between the embryo and the sprouted kernel was achieved. Also, a difference was observed between the kernel that was sprouted and the kernel known to be unsprouted by using the same imaging parameters. The parameters for the log 1/R spectroscopic image and the parameters used for the PCA factors were identical to allow a direct comparison between a sprouted kernel and an unsprouted kernel.

Experiments with InSb Focal Plane Array

In addition to data processing mentioned in previous section, in further studies, some other preprocessing steps were used such as baseline correction, normalization or derivatives to distinct the sprouted kernel from unsprouted one more efficiently. With preprocessing steps, variations other than chemical components such as physical effects including different seed morphology, illumination were removed from the spectral information. Further data evaluation

was performed with comparison of PCA factors, lipid/protein ratios, or wavelength selective intensity.

3. Results and Discussion

Experiments with InGaAs

Figure 2.8 shows image selected from recent article (Smail et al., 2006) on chemical imaging of germinated wheat. The images of a model unsprouted kernel are on the left column while images of a model sprouted kernel appear in the right column. The first image in each column is a spectroscopic response in which each pixel displays a value for log 1/R at 1680 nm wavelength. Following the spectroscopic log 1/R image is the first factor of PCA factor maps that also shows contrast. Images that best revealed the developing embryo were from PCA factors 1, 3, 4 and 6. First factor in PCA represents 99% variance in the single wheat kernel image.

Figure 2.8 Spectroscopic images and PCA factor of a single wheat kernel of sprouted (right) and unsprouted (left) indicate embryo development on the germ side (right end) of sprouted kernel by contrast in the images.

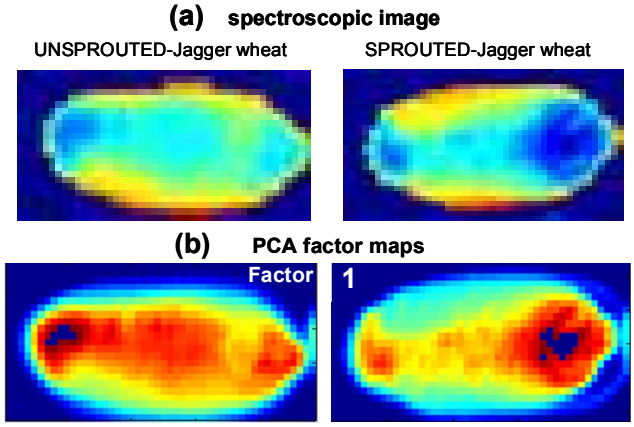

All different factors indicate the size, geometry, and density of developed embryo in the sprouted kernel. Note in the sprouted kernel that false color images (right column) in a more or

less circular shape contrast are considered evidence of the existence of a developing embryo below the surface.

In Figure 2.9, kernel images of the variety 'Trego' are shown. A group of 15 unsprouted kernels are on the top three rows and a group of 30 kernels that sprouted after moisture exposure for 36 hr are on the bottom six rows. Note among the images of sprouted kernels that both round shape and intensity are shown by the false color, and that different sizes of the embryo represent differing stages of development.

Figure 2.9 PCA factor 1 images of 15 unsprouted (top) and 30 sprouted kernels (bottom) represent a comparison between the sprouted kernels and unsprouted kernels. While 30 kernels of 30 are sprouted in 36 hr moisture exposure, germinated kernels in 3 hr moisture exposure is less than 10%.

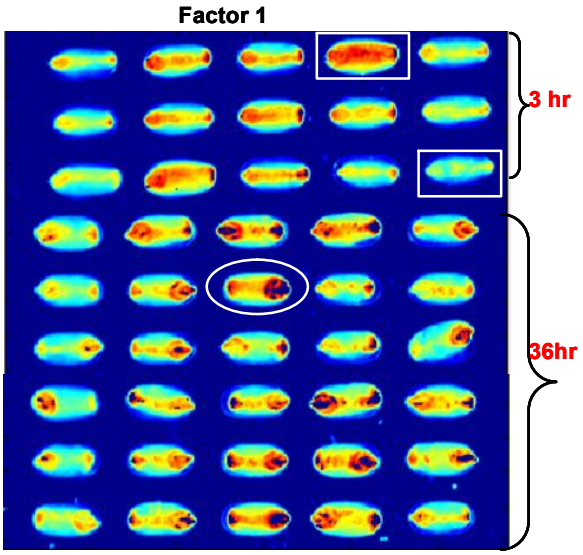

Figure 2.10 also shows PCA factor 4 kernel images of the same 15 unsprouted kernels at the top and the same 30 sprouted kernels at the bottom. On both figures 3 and 4, two examples of unsprouted kernels are shown with rectangles. Ellipses highlight sprouted images for factor 1 and factor 4. From the images of the kernels shown in Figures 3 and 4, it was determined that 30

out of 30 kernels were sprouted on the basis of the PCA factors 1 and 4. In contrast, by using the same criteria on kernels exposed to moisture for 3 hr, less than 10% were identified as being sprouted.

Figure 2.10 PCA factor 4 images of 15 unsprouted (top) exposed to 36 hr germination and 30 sprouted kernels (bottom) exposed to 3 hr germination shown in figure 2 gives the same evaluation as factor 1.

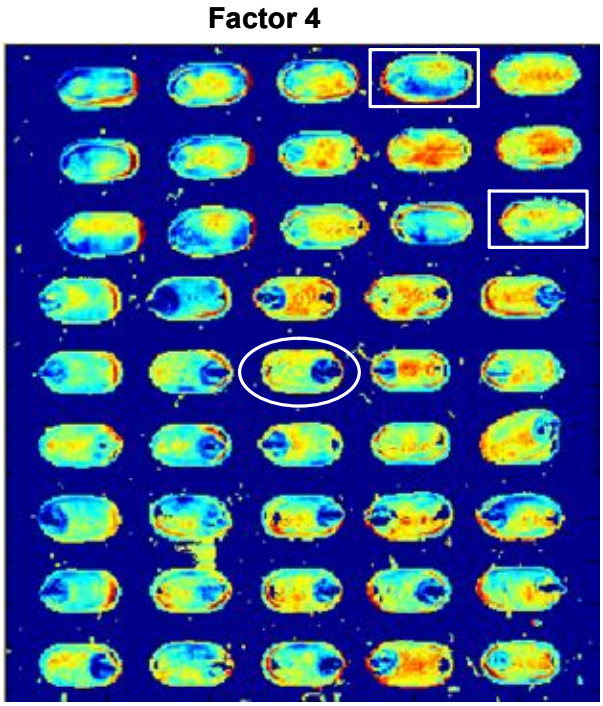

The germination response to 36 hr moisture exposure is shown in Figure 2.11 based on a GO/NO GO classification of 90 kernels for each of six cultivars by using two PCA factors. Note that the shaded portions of the bar graph show the number of sprouted kernels from the field of 90. The unshaded portion of the graph represents the difference between those sprouted and the 90 that were present. For these results no attempt was made to reexamine the specimen plates to look for nonviable (dead) kernels. A correction of these data by deleting the nonviable ones would increase the percentage considerably. Among cultivars shown on the bar graph in Fig.2.9, in order left to right, Betty, Trego, Danby, Jagger, KS-89180, KS-2174 it is noted that the Betty,

Trego, Jagger, and KS-89180 have a high percentage of sprouted kernels. In contrast, Danby and experimental line KS-2174 show a much lower percentage of germinated kernels out of the 90 presented. This numerical revelation of the nonsprouted characteristic, even at 36 hr, indicatives that KS-2174 is relatively sprout resistant in comparison with the other cultivars tested. This is precisely the type of data that can assist plant breeders in selection of sprout resistance lines. The numbers of sprouted kernels in each one are Betty *80*, Trego *85*, Danby *70*, Jagger *74*, KS-89180 *87*, KS-2174 *48*. Figure 2.11 shows the tally of kernels classified as sprouted at the 36-hr period for each of the six cultivars examined.

Figure 2.11 Germination responses of 90 kernels of six cultivars at 36 hr are represented as bar graphs. Among the six cultivars, Trego, KS89180, and Betty have more than 85% germination. While Danby and KS2174 are relatively more resistant to germination.

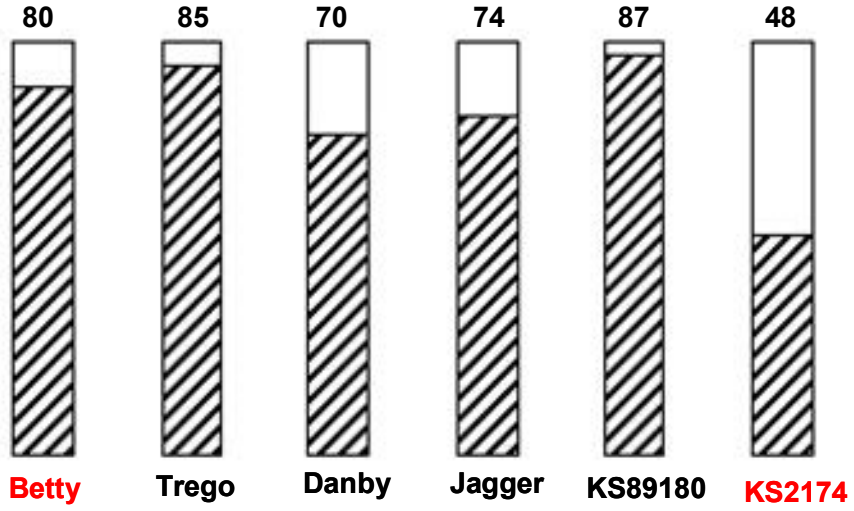

Figure 2.12 shows the germination response to different moisture exposure times for two different cultivars. Betty at 36 hr showed that 80 out of 90 kernels had sprouted. Betty is a white wheat that is currently being grown throughout Kansas. Note that the progression from 48-hr exposure with 83 kernels, to 80 at 36-hr, 73 at 24-hr, 58 at 12 hr, and 52 even at 6-hr

exposure. In contrast to those values, note the shaded bars with a much lower tally at 48 hr of 58 down to 31 out of 90 at 6 hr. Between these two cultivars, there is a bias towards sprout resistance at all time periods for KS-2174, compared with Betty. It is noteworthy that the same number of sprouted kernels 58 that was produced with Betty at 12 hr required 48 hr for KS-2174. Thus, it took a four times longer exposure to moist conditions to produce the same germination level. It is this type of dramatic difference that should be exploited to assist our Kansas Agricultural Experiment Station plant breeders producing new varieties of Hard White Winter wheats. Research in nondestructive near-IR imaging is ongoing at present with detection wavelengths 1200-2400 with InSb FPA for the potential for unsupervised GO/NO GO determination

Figure 2.12 Germination responses of 90 kernels of Betty and KS2174 to moisture exposure times 6, 12, 24, 36, and 48 hr are represented as bar graphs, open and shaded, respectively. KS 2174 is more resistant to germination and has approximately 40% less sprouted kernels than the Betty in all moisture exposure times.

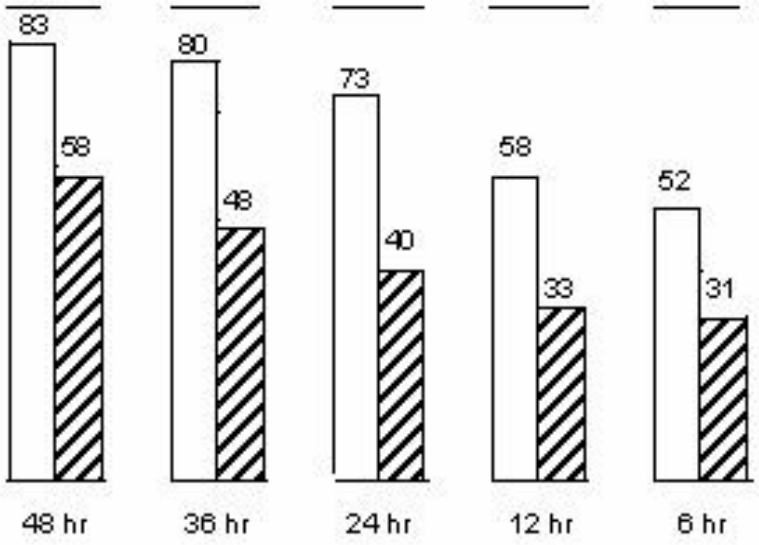

Experiments with InSb

Spectroscopic effect of drying and treatment optimization

Wheat kernels were analyzed wet immediately after germination and dry after being freeze-dried or oven dried. This revealed the effect of drying on the spectra. Without drying the water peak at 1940 nm strongly masked the region 2000-2200 nm which includes starch and protein bands. This effect of the water peak is more predominant on spectra of germ (Figure 2.13b). After drying (Figure 2.13), the masking effect was removed.

Figure 2.13 Spectra selected from germ and endosperm side of the a) Unsprouted samples, b) germinated wet samples, and c) dried germinated samples, d) showing a spectra from each sample in same panel. Note the differences of red spectrum (for wet sample) than control and dried spouted sample. Also note, figure b highlights huge water peaks at 1940 masking protein and starch bands in spectrum.

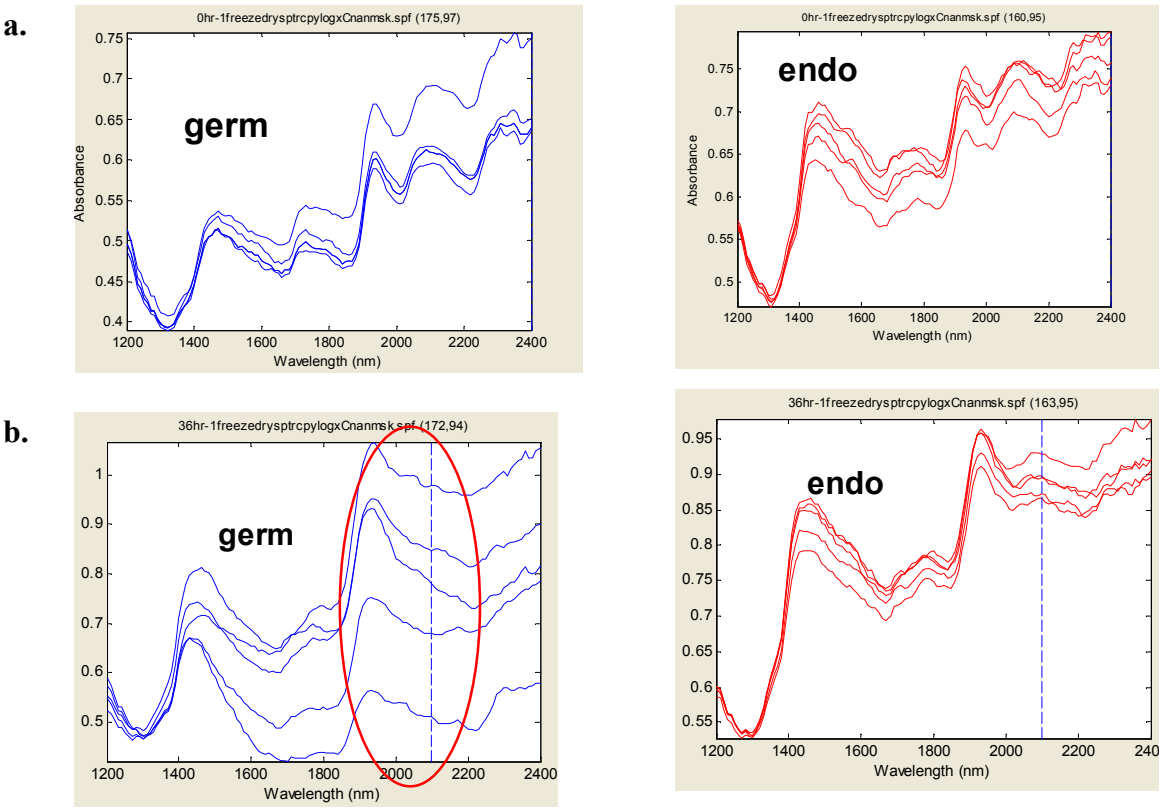

c.

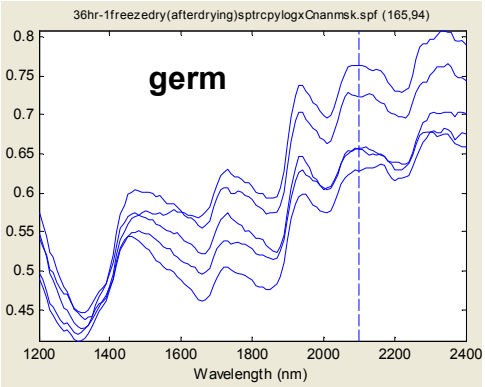

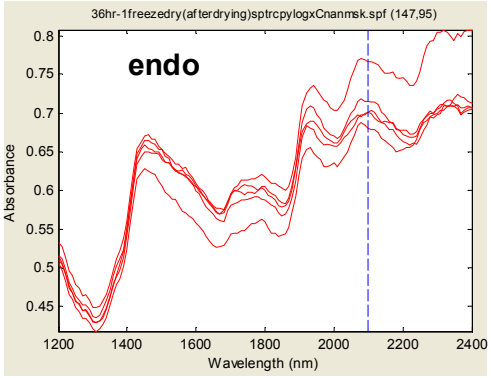

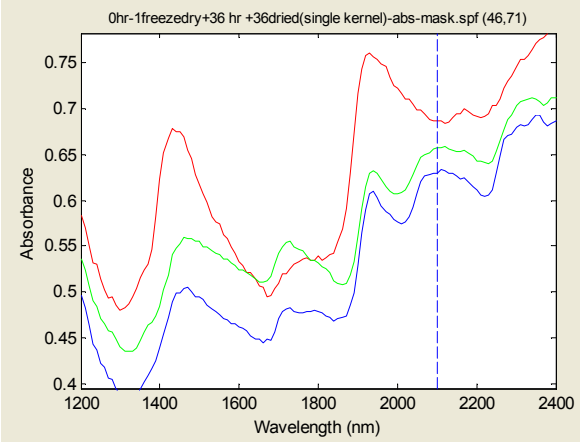

Blue: unsprouted samples

Red: germinated wet samples

Green: dried germinated samples

PCA analysis is a good starting point in data analysis providing the information how variation is distributed between factors, which factors are important and indicating the possible important peaks can cause the variation. The spatial distribution of water can be seen from PCA factor 5 (Figure 2.14). It was concentrated in germ area of the kernel.

Figure 2.14 Effect of water peak can be seen in PCA factor 5 loading of wet samples indicating a very definite peak at 1940 nm with a high PCA score.

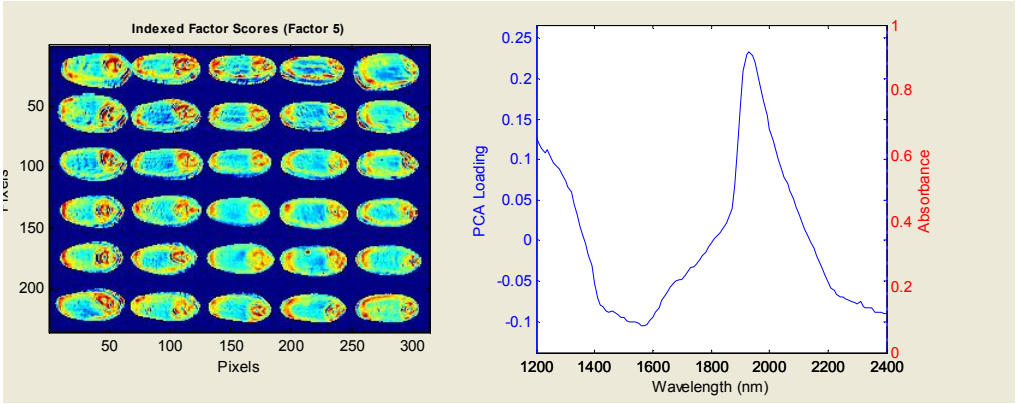

When the effect of the water was understood, different drying methods including freeze drying, vacuum oven drying, forced drift air drying were compared from peak heights at 1940 nm baseline corrected spectra. It was observed that forced air drying was not effective, other two methods gave similar results. Vacuum oven drying was selected because of the simplicity and less time requirement (see Appendix B for this optimization step). However it was observed that there is a big shrinkage in the size of the kernel after drying in vacuum oven while the texture, size were remained same for the freeze dried samples. Oven drying under vacuum did not cause a chemical changes within the kernels, thus it can be used safely.

Preliminary experiments for the purpose of understanding bands in the spectrum

Two main components of the wheat are starch and gluten. The mean spectrum of starch and gluten were shown. For starch 2100 nm is characteristic wavelength while 2050 and 2180 nm are characteristic for protein.

Figure 2.15 Average of 18,000 spectra from the data cube of starch and assigned peaks

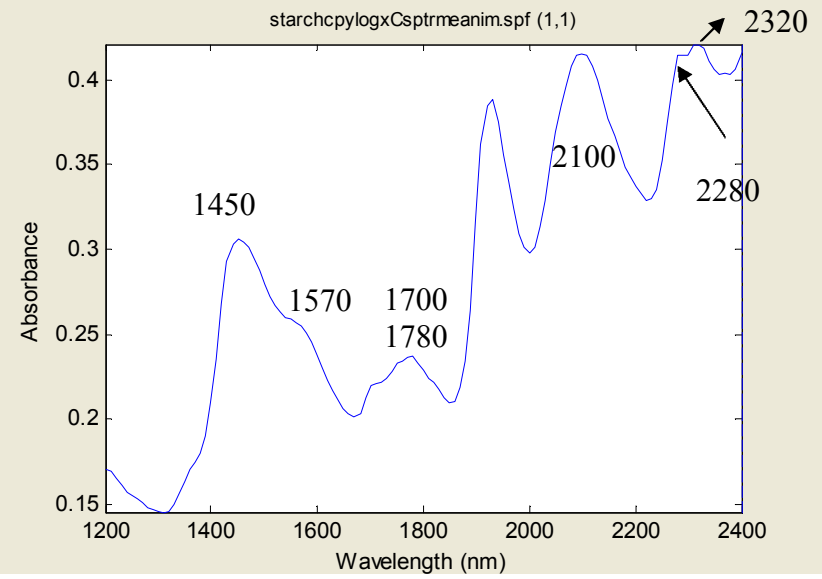

Figure 2.16 Average of 24,000 spectra from the data cube of gluten

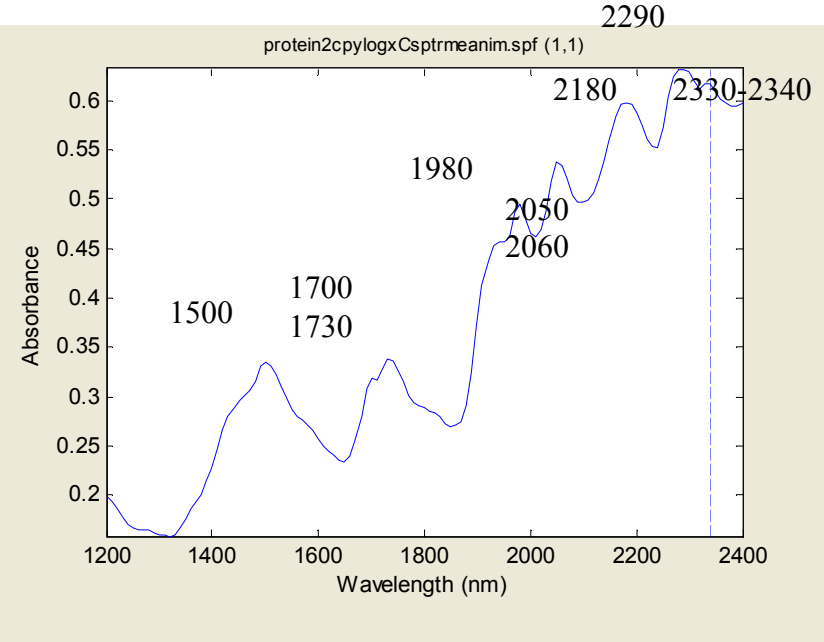

Figure 2.17 Spectra of lipid extracted from whole wheat and pentosans (reprinted from ref 76.)

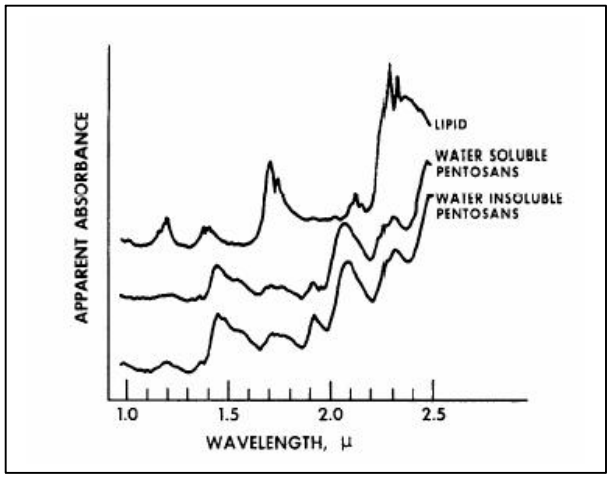

In the studies by Wetzel (72) and Law and (77), 2100 nm is assigned for starch, 2180, 2050 nm for protein, 2310, 2348 nm for lipid, 2336 and 2350 for cellulose. In lipid spectrum (Figure 2.17), peaks are at 1170, 2140, 2170 nm (C-H vibrations). Peaks and assignments of

wheat and wheat components were done in detail by Law and Thachuk (77), the peaks at 1700, 1730, 1760 nm is due to CH_2 group, C-H 1st overtone. 2180 and 2050 nm are C=O + Amide III combination, N-H+ amide II combinations, respectively. For starch 2100nm is by O-H combination, starch and pentosan have peaks at 2280 and 2320nm (C-H combinations) and 1540 and 1450 nm (O-H combination and O-H 1st overtone. For lipid 2310 and 2340 nm are from CH_2, C-H combination. Also peaks at 1720 and 1760 nm are due to CH_2 group, C-H 1st overtone (76, 77). As seen in the figure 2.18, the spectrum of the wheat is determined largely by the carbohydrate components. Starch band at 2100 nm is overlapping with the protein bands and masking them.

Figure 2.18 Mean spectrum of a wheat kernel indicating the spectrum of the wheat is determined largely by the carbohydrate components.

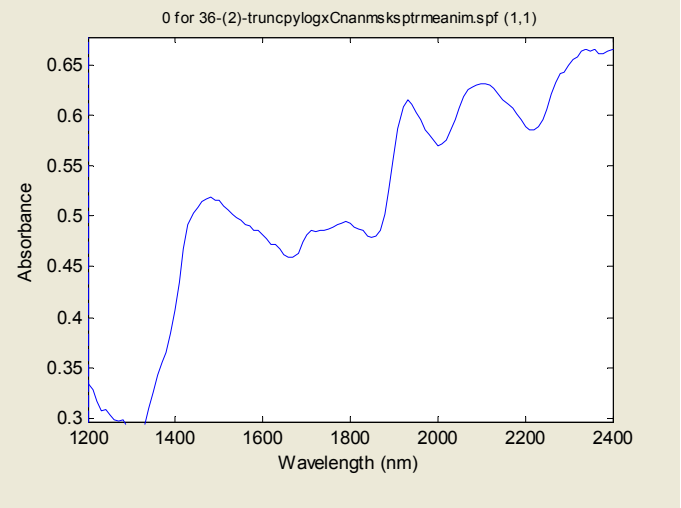

Comparison of sprouted and unsprouted kernels of variety Betty by different data treatments:

There are different ways to discriminate sprouted kernel from unsprouted kernel. In the figures below some of them will be explained. This data represent an attempt in nondestructive

near-IR imaging with detection wavelengths 1200-2400 with InSb FPA for the potential for unsupervised GO/NO GO determination.

In figure 2.19 a, embryo development can be observed by wavelength discrimination at 2310 nm but it was not very distinctive. When data were baseline corrected, a better contrast was obtained between (Figure 2.19 b) sprouted and unsprouted kernels. And developing embryo was separated from rest of the kernel body.

Figure 2.19 Comparison of sprouted (36 hr) and unsprouted (3hr) kernels at 2310 nm. Image (a) is absorbance intensity at 2310 nm while (b) is baseline corrected intensity at 2310 nm and (c) normalized intensity at 2310 nm .Left three kernels represent unsprouted (3hr) and right three represent sprouted (36 hr) in figures.

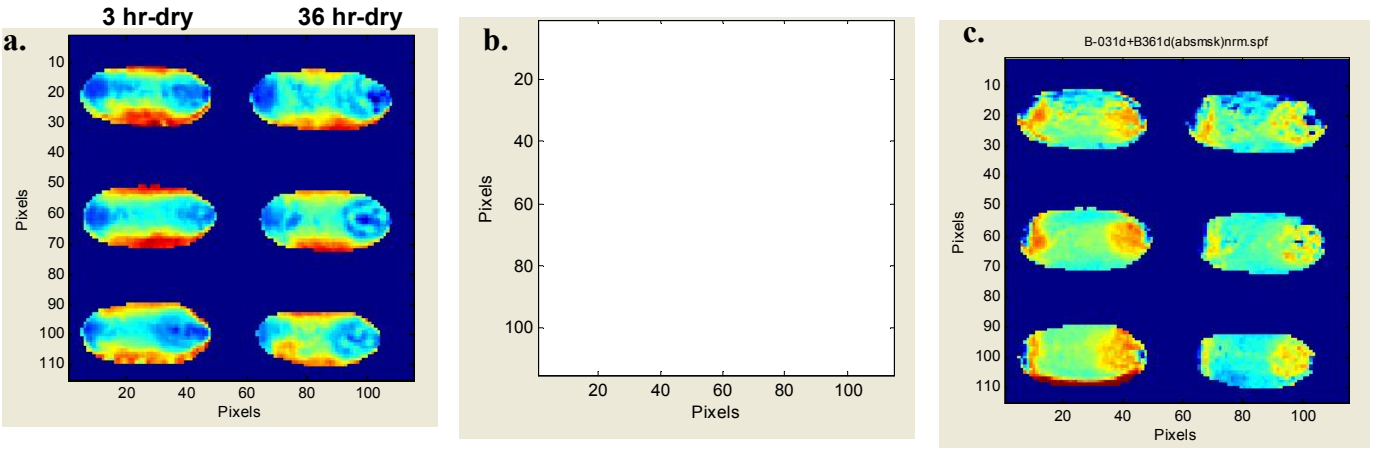

In addition to wavelength selective discrimination, comparison of peak height ratios was used for discrimination. In figure 2.20 peak height (2310 / 2060) image was obtained and 42 spectra of germ area was averaged to find a mean ratio. Average ratio values for the germ side of each kernel are represented (Figure 2.20). A reduction in the lipid / protein ratio was observed with germination which is consistent with the results reported in part one this thesis.

Figure 2.20 Peak height ratio (2310/2060) image and average ratio values for the germ side of each kernel. Note the differences in ratios and reduction with sprouting.

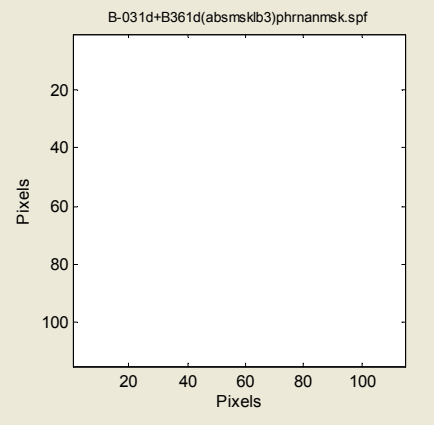

Ratio average of 42 spectra (pixels) from germ side

Unsprouted	**Sprouted**
0.42	0.31
0.52	0.36
0.49	0.40

If second derivative is performed, and PCA is applied, we can obtain similar discrimination and Factor 2 (Figure 2.21) loading indicates a peak at 2310 nm which can be the source of variation.

Figure 2.21 PCA factor 2 of second derivative data

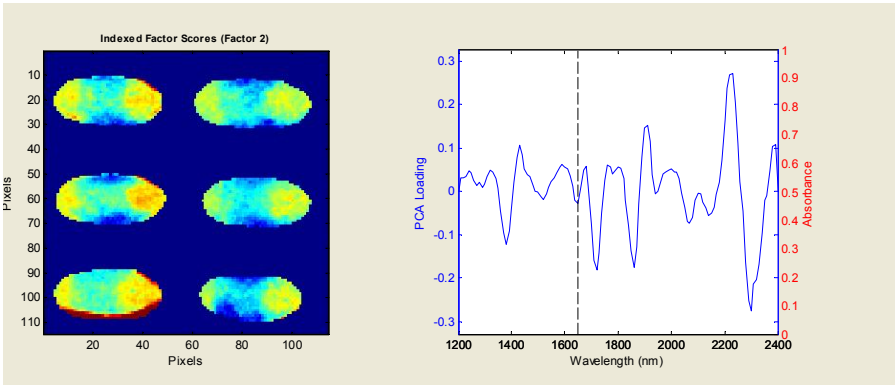

Potential for future unsupervised multikernel testing

With one of the procedures explained above, preliminary experiments were done for the potential an unsupervised discrimination. A macro was written to process all the plates including 20 seeds in identical way and rapidly. In this macro, first the image was spatially truncated and

converted in log 1/R (Absorbance) units. Next, it was spatially masked between 0.2-0.75 intensity values in histogram to remove pixels from nonsample area. After masking, the image was baseline corrected with a polynomial drawn with points at valleys of 1320, 1850, 2220 and 2380 nm and peak height ratio was calculated with baseline corrected spectra. Next, 40-50 pixels selected from germ and endosperm parts of each 20 kernels and the average ratio was calculated for this group of pixels (total 9600 pixels for each cultivar) .Then the gross mean of these ratios for 20 kernels was obtained (Table 2.1). Note the reduction was observed for all kernels in this data set.

Table 2.1 The gross mean of the results for Betty

	Germ area
3 hr	0.445
36 hr	0.382

When similar process was applied to normalized or baseline corrected peak intensity at 2310, same result could be obtained. The mean ratio for 20 kernels of unsprouted was found 1.70 while for the sprouted kernels (36 hr) it was reduced to 1.34 (normalized data intensity). For 12 hr sprouted kernel it was reduced to 1.46.

4. Conclusion

From the Sprouted / Nonsprouted multivariate classification of 90 moisture treated wheat kernels, it was evident that a single hard wheat cultivar had a higher sprouting resistance than five other cultivars examined. This was based on 48 of 90 germinated after a 36 hr treatment. In comparison a completely germinated 36 hr cultivar that had 80 of 90 kernels classified by multiple image data as germinated. Excluding the presence of non viable (dead) kernels, the correct classification would actually be higher. For both the cultivar with the highest germination

and the one with the highest sprout resistance at intermediate treatment times of 24 hr, 12 hr, and 6 hr, differentiation was evident. The less resistant cultivar had significant germination even at short exposure times.

Study for the potential for unsupervised GO/NO GO determination in nondestructive near-IR imaging with detection wavelengths 1200-2400 with InSb FPA is ongoing. Some preliminary results were presented which are encouraging.

References

1 Hoseney, R.C. Structure of cereals. In: Principles of Cereal Science and Technology; American Association of Cereal Chemists Inc: Minnesota, 1998; pp 1-11.

2 Anon. The practice of flour milling; National Association of British and Irish Millers Limited Inc.: London, 1979; Vol. 1, pp.13-27.

3 Posner, E.S.; Hibbs, A.N. Wheat: the raw material. In: Wheat Flour Milling; American Association of Cereal Chemists Inc: Minnesota, 1997; pp 2-10.

4 MacMasters M.M.; Hinton, J.J.C.; Bradbury, D. Microscopic structure and composition of the wheat kernel. In: Wheat Chemistry and Technology; Pomeranz, Y., Ed.; American Association of Cereal Chemists Inc: Minnesota, 1971; Vol.7, pp. 51-114.

5 King, R.W. Physiology of sprouting resistance. In: Preharvest Field Sprouting in Cereals; Derera, N.F.,Ed.; CRC Press, Inc: Baco Raton, Florida, 1989; pp. 28-55.

6 Swift, J.G.; O'Brien, T.P.The fine structure of the wheat scutellum before germination. *Aust. J. Biol. Sci.* **1972**, *25*, 9-22.

7 Derera, N.F. 1989. The effects of preharvest rain. In: Preharvest Field Sprouting in Cereals; Derera, N.F.,Ed.; CRC Press, Inc: Baco Raton, Florida, 1989; pp.2-14.

8 Mares, D.J. Temperature dependence of germinability of wheat (Triticum aestivum L.) grain in relation to pre-harvest sprouting. *Aust. J. Agric. Res.* **1984**, *35*, 115-128.

9 Andreoli, C.; Bassoi, M.C.; Brunetta, D.Genetic control of seed dormancy and pre-harvest sprouting in wheat. *Sci. Agric.* **2006**, *63(6),* 564-566.

10 Simon, E.W. Early events in germination. In: Seed Physiology, Germination and Seed Mobilization; Murray D.R.,Ed.; Academic Press: Australia, 1984; Vol. 2, pp.77-111

11 Mares, D.J. 1989. Preharvest sprouting damage and sprouting tolerance: assay methods and instrumentation. In: Preharvest Field Sprouting in Cereals; Derera, N.F., Ed.; CRC Press, Inc: Baco Raton, Florida, 1989; pp. 129-170.

12 Anon. Germiantion.http://www.wheatbp.net/cgi-bin/grain2.pl?topic=Germination

12a Anon. Dormancy http://en.wikipedia.org/wiki/Dormancy

13 Swift, J.G.; O'Brien, T.P. The fine structure of the wheat scutellum during germination. *Aust. J. Biol. Sci*.**1972**, *25*, 469-486.

14 Fincher, G.B. Molecular and cellular biology associated with endosperm in germinating cereal grains. *Annu. Rev. Plant Physiol. Plant Mol. Biol.***1989**, *40,* 305-346.

15 Bewley, J.D.; Black. M. Cellular events during germination and seedling growth. In: Seeds: Physiology of Development and Germination; Plenum Press: New York, 1994; pp. 147-191.

16 Bewley, J.D.; Black. M. Mobilization of stored seed reserves. In: Seeds: Physiology of Development and Germination; Plenum Press: New York, 1994; pp. 293-341.

17 Bewley, J.D.; Black. M. Seeds and germination: some agricultural and industrial aspects In: Seeds: Physiology of Development and Germination; Plenum Press: New York, 1994; pp 377-421.

17a Bewley, J.D.; Black. M. Seed development and maturation. In: Seeds: Physiology of Development and Germination; Plenum Press: New York, 1994; pp. 35-110.

17b Bewley, J.D.; Black. M. Dormancy and control of germination. In: Seeds: Physiology of Development and Germination; Plenum Press: New York, 1994; pp. 199-267.

18 Ashford, A.E.; Gubler, F. Mobilization of polysaccharide reserves from endosperm. In: Seed Physiology, Germination and Seed mobilization; Murray D.R., Ed.; Academic Press: Australia, 1984; Vol. 2, pp117-157.

19 Corder, A.M.; Henry, R.J. Carbohydrate-degrading enzymes in germinating wheat. *Cereal Chem.* **1989**, 66(5), 435-439.

20 Tavener, R.J.A.; Laidman, D.L. The induction of triglyceride metabolism in the germinating wheat grain. *Phytochemistry.* **1972**, *11*, 981-987.

21 Tavener, R.J.A.; Laidman, D.L. The induction of lipase activity in the germinating wheat grain. *Phytochemistry*. **1972**, *11*, 989-997.

22 Kruger, J.E. Biochemistry of preharvest sprouting in cereals. In: Preharvest Field Sprouting in Cereals; Derera, N.F., Ed.; CRC Press, Inc: Baco Raton, Florida, 1989; pp. 61-85.

23 Juhasz, R.; Gergerly, S.; Gelencser, T; Salgo, A. Relationship between NIR spectra and RVA paramaters during wheat germination. *Cereal Chem*. **2005**, *82(5),* 488-493.

24 MacGregor, A.W.; Matsuo, R.R. Starch degradation in endosperms of barley and wheat kernels during initial stages of germination. *Cereal Chem*. **1982**, *59(3),* 210-216

24a Horton, H.R. Carbohydrates. In: Principles of Biochemistry. Upper Saddle River, NJ : Pearson Prentice Hall, 2006; pp. 223-249.

25 Meredith, P.; Pomeranz, Y. 1985. Sprouted Grain. In: Wheat Chemistry and Technology; Pomeranz, Y., Ed.; American Association of Cereal Chemists Inc: Minnesota, 1971; Vol.7, pp. 239-320.

26 Hargin, K.D.; Morrison W.D.; Fulcher R.G. Triglyceride Deposits in the Starchy Endosperm of Wheat. Cereal Chem. **1980**, *57(5),* 320-325.

27 Aoki, N; Scofield, G.N.; Wang, X.; Offler, C.E.; Partick, J.W.; Furbank, R.T. Pathway of sugar transport in germinating wheat seeds. *Plant Physiol*. **2006**,*141*, 1255-1263.

28 Robinson, J.W; Frame, A.M.S.; Frame II, G.M. Infrared Spectroscopy. In: Undergraduate Instrumental Analysis; Marcel Decker: New York, 2005; pp.213-310.

29 Wetzel, D.L. Microbeam molecular spectroscopy of biological materials. In: Food Flavors: Generation, Analysis and Process Influence; Charalambous, G., Ed.; Elsevier Press, 1995; pp 2039-2108.

30 Wetzel, D.L. Molecular methods in control of breeding for end use quality. *Proc. International Cereal Chem. Conf.* 2002, Budapest University of Technology and Economics, Budapest, Hungary; pp. 81-88.

31 Budevska, B.O. Vibrational spectroscopy imaging of agricultural products. In: Handbook of Vibrational Spectroscopy; Chalmers, J.M and Griffiths, P.R., Eds.; John Wiley & Sons Ltd: Chichester, 2002; Vol.1, pp. 1-13.

32 Wetzel, D.L; Levine, S.M. Microspectroscopy: imaging molecular chemistry with infrared microscopy. *Science*.**1999,** *285(5431),* 1224-1225.

33 Griffths, P.R.; deHaseth, J.A. The Michelson interferometer. In: Fourier Transform infrared spectrometry; John Wiley & Sons Ltd: New York, 1986; pp.1-55.

34 Kwiatkoski, J.M.; Reffner, J.A. FT-IR microspectrometry advances. *Nature.* **1987**, *328(27),* 837-838.

35 Wetzel, D.L. Biomedical applications of infrared microspectroscopy and imaging by various means. In: Modern Concepts in Biomedical Infrared Microspectroscopy; Lasch, P and Kneipp, J., Eds.; John Wiley & Sons, Inc:UK, 2008; pp. 39-78. In Press.

36 Reffner, J.A.; Vogel, S.H. Confocal microspectometry system. U.S. Patent 5,864. 1999

37 Carr, G.L.; Reffner, J.A.; Williams, G.P. Performance of an infrared microspectrometer at the NSLS, *Rev. Sci. Instr.* **1995**, *66*, 1490-1492

38 Lewis, E.N.; Treado, P.J.; Reeder. R.C.; Story, G.M.;Dowrey, A.E.; Marcott, C.; Levin, I.W. Fourier Transform Spectroscopic Imaging Using an Infrared Focal-Plane Array Detector. *Anal. Chem.* **1995**, *67,* 3377-3381.

39 Marcott, C.; Reeder, R.C.; Sweat, J.A.; Panzer, D.D.; Wetzel, D.L. FT-IR spectroscopic imaging microscopy of wheat kernels using a Mercury-Cadmium-Telluride focal plane array detector. *Vibr. Spectrosc.* **1999,** *19*, 123-129.

40 Reffner, J.A. Uniting microscopy and spectroscopy. *Am. Lab.*. **2000**, *June*, 36-40

41 Budevska, B.O.; Sum, S.T.; Jones, T.J. Application of multivariate curve resolution for analysis of FT-IR microspectroscopic images of *in situ* plant tissue. *Appl. Spectrosc.* **2003,** *57(2),* 124-131.

42 Barron, C; Parker, M.L.; Mills, E.N.C.; Rouau, X.; Wilson, R.H. FTIR imaging of wheat endosperm cell walls in situ reveals compositional and architectural heterogeneity related to grain hardness. *Planta*. **2005**, *220,* 667-677.

43 Philippe, S.; Robert, P.; Barron, C.; Saulnier, L., Guillon, F. Deposition of cell wall polysaccharides in wheat endosperm during grain development: FT-IR microspectroscopy study. *J. Agric. Food Chem*. **2006**, *54*, 2303-2308.

44 Wetzel, D.L.; Reffner, J.A. Using spatially resolved fourier transform infrared microbeam spectoroscopy to examine the microstructure of wheat kernels. *Cereal Foods World.* **1993**, *38(1),* 9-20

45 Wetzel, D.L.; Fulcher R. G. FT-IR microspectroscopy of food ingredients. In: *Flavors and Off-Flavors*; Charalambous, G., Ed.; Elsevier Press: Amsterdam, 1990; pp. 485-510.

46 Wetzel, D.L.; Reffner, J.A. Compositional profile in grain thin sections by fourier transform infrared microspectrometry. In: Proceedings of the International Cereal Chemistry Symposium; Lasztity, R., Ed.; Budapest, Hungary, 1991; pp.47-52

47 Wetzel, D.L.; Srivarin, P.; Finney, J.R. Revealing Protein Infrared Spectral Detail in a Heterogeneous Matrix Dominated by Starch. *Vibr. Spectrosc.,* **2003,** *31*, 109-114.

48 Miller, L.M.; Dumas, P. Chemical imaging of biological tissue with synchrotron infrared light. *Biochimica et Biophysica Acta.* **2006**, *1758*, 846–857.

49 Spectrum Spotlight, User's guide. Perkin Elmer 2001.

50 Carr, G.L.; Chubar, O.; Dumas, P. In: Spectrochemical Analysis Using Infrared Multichannel Detectors; Bhargava, R. and Levin, I.W., Eds.; Blackwell Publishing: Oxford UK, 2006; pp. 56–84.

51 Shashikumar, K; Hazelton, J.L.; Ryu, G.H and Walker, C.E. Predicting wheat sprout by near-infrared reflectance analysis. *Cereal Food World.* **1993**, *38(5),* 364-366

52 Mares, D.J. Preservation of dormancy in freshly harvested wheat grain. *Aust. J. Agric. Res.* **1983**, *34*, 33-38.

53 Tran, V.N.; Cavanagh, A.K. Structural aspects of dormancy. In: Seed Physiology, Germination and Seed Mobilization; Murray D.R., Ed.; Academic Press: Australia, 1984; Vol. 2, pp. 1-40.

54 Henry, R.J.; Brennan, P.S. Dormancy breaking procedures and the breeding of white-grained wheat resistance to preharvest sprouting. *Euphytica.* **1988**. *39*, 161-166.

55 Miura, H; Sato, N.; Kato, K.; Amano, Y. Detection of chromosomes carrying genes for seed dormancy of wheat using the backcross reciprocal monosomic method. *Plant Breed.* **2002**, 121, 394-399.

56 Wu, J.; Carver, B.F. Sprout damage and preharvest sprout resistance in hard white wheat. *Crop. Sci.* **1999**, *39*, 441-447.

57 Donelson, J.R.; Gaines, C.S.; Donelson, T.S.; Finney, P.L. Detection of wheat preharvest sprouting using a pregelatinized starch substrate and centrifugation. *Cereal Chem*. **2001**, *78(3),* 282-285.

58 Wrigley, C. Sprouted grain: detection and aberrant results. *Cereals Food World.* **2004**, *49(3),* 169-171

59 Skerritt, J.H.; Heywood, R.; Lindahl, L.; Psotka, J.J.; Wrigley, C.W. Rapid determination of sprout damage. *Cereal Foods World*. **2001**, *46(2),* 55-58.

60 Verity, J.C.K.; Hac, L.; Skerritt, J.H. Development of a field enzyme-linked immunosorbent assay (ELISA) for detection of α-amylase in pre-harvest spouted wheat. *Cereal Chem*. **1999**, *76(5),* 673-681.

61 Finney, P.L; Kinney J.E., Donelson, J.R.. Prediction of damages starch in straight-grade flour by near-infrared reflectance analysis of whole ground wheat. *Cereal Chem.* **1988**, *65(6),* 449-452

62 Juhasz, R., Gergely, S.; Szaboki, A.; Salgo, A. Correlation Between NIR Spectra and RVA Parameters During Germination of Maize *Cereal Chem.* **2007**, *84(1),* 97–101.

63 Smail, V.W.; Fritz, A.K; Wetzel, D.L. Chemical imaging of intact seeds with NIR focal assists plant breeding. *Vibr. Spectrosc*. **2006**, *42*, 215–221.

64 Kemeny, G. J.; Wetzel,D. L. Optical analysis method and apparatus having programmable rapid random wavelength access. U.S. Patent 4,883,963 28, 1989.

64a Sweat, J.A. and Wetzel, D.L. Near Infrared Acousto-Optic Tunable Filter Based Instrumentation for the Measurement of Dynamic Spectra of Polymers. *Rev. Sci. Instrum.,* **2001**, *72(4),* 2153-2158.

65 Wetzel, D.L.**,** Eilert, A.J.; Sweat, J.A. Tunable Filter and Discrete Filter Near-IR Spectrometers. In: Handbook of Vibrational Spectroscopy; Chalmers, J. M. and Griffiths P.R.,Eds.; John Wiley & Sons Ltd: Chichester, U.K., 2002; pp. 436-452.

66 Hammaker, R.M.; DeVerse, R.A.; Asunskis, D.J.; Fateley, W.G. Hadamard Transform Near-infrared Spectrometer. In: Handbook of Vibrational Spectroscopy; Chalmers, J. M. and Griffiths P.R., Eds.; John Wiley & Sons Ltd: Chichester, West Sussex, UK, 2002; Vol.1, pp. 453-460

67 Stark, E.W.2002. Near-infrared array spectrometers. In: Handbook of Vibrational Spectroscopy; Chalmers, J. M. and Griffiths P.R., Eds.; John Wiley & Sons Ltd: Chichester, West Sussex, UK, 2002; Vol.1, pp. 1-30

67a Wetzel, D.L. Contemporary near infrared instrumentation. In: Near Infrared Technology in the Agricultural and Food Industries; Williams, P.C and Norris, K.,Eds.; Am.Assoc.Cereal.Chem: St. Paul, Mn., 1999.

68 Sugiyama,J. Visualization of sugar content in the flesh of a melon by near-infrared imaging. *J. Agric. Food Chem.* **1999**, *47,* 2715-2718.

69 Dubois,J.; Lewis,E.N;Fry Jr.,F.S.; M. Calvey, E.M. Bacterial identification by near-infrared chemical imaging of food-specific cards. *Food Microbiology*. **2005**, *22*, 577–583

70 Lee, E.;Huang, W.X.; Chen, P.; Lewis, E.N.; Vivilecchia, R.V. High-Throughput Analysis of Pharmaceutical Tablet Content Uniformity by Near-Infrared Chemical Imaging. *Spectrosc.* **2006**, *November*

71 Dubois, J.; Wolff, J, warrack, J.K; Schoppelelrei, J; Lewis, E.N. NIR Chemical Imaging for Counterfeit Pharmaceutical Products Analysis. *Spectrosc.* **2007**, *February*

72 Wetzel, D.L. Near-infrared reflectance analysis sleeper among spectroscopic techniques. *Anal. Chem*. **1983**, *55(12),* 1165A-1175A

73 Wetzel,D.L.Reflectance. In: Analytical Near-IR Spectroscopy. 1989

74 Wetzel, D.L. Analytical Near-IR Spectroscopy. In: Instrumental Methods in food and Beverage Analysis; Wetzel, D.L.B. and Charalambous, G.; Eds.; Elsevier Science: B.V. 1998.

75 Lewis, E.N.; Schoppelrei, J.; Lee, E. Near-infrared Chemical Imaging and the PAT Initiative. *The Role of Spectroscopy in Process Analytical Technologies*. **2005**, *January,* 28-34

76 McClure, W.F.; Stanfield, D.L. Near-infrared spectroscopy of biomaterials. In: Handbook of Vibrational Spectroscopy; Chalmers, J.M and Griffiths, P.R., Eds.; John Wiley & Sons Ltd: Chichester, 2002; Vol.1, pp.1-17

77 Law, D.P; Thachuk, R. Near infrared diffuse reflectance spectra of wheat and wheat components. Cereal Chem. 1**977**, *54(2),* 256-265.

Appendix A

Near-IR Analysis for Sprout Damage Test

Near-IR analysis has also been used for prediction of mechanical starch damage by some researchers. Finney et al. (1988) measured starch damage of ground whole wheat by enzymatic method and near-IR reflectance analysis and correlated them. High correlations (0.91-0.94) were observed between two methods. In another study (Morgan and Williams,1995) for the starch damage in wheat flour, correlation coefficient was found 0.90 between laboratory values and near-infrared predicted values. Juhasz et al. (2005) studied the relationship between near-infrared and RVA parameters during wheat germination with Partial least squares (PLS). The high linear correlation (0.95-0.98) between RVA rheological parameters and near-IR predicted values. Maximum correlation was observed gelatinization period of RVA measurement. In this study it was suggested that near-IR spectra of dry samples were evaluated more easily than wet samples which had water peaks. Dried samples (oven 120ºC 2 hrs) had higher correlation coefficients compared to wet samples. Juhasz et al. (2007) attempted to analyze germinated maize samples nondestructively immediately after germination while wet. They observed that correlation is poor in this case due to variation in spectra caused by water and morphological character of seed. Shashikumar et al. (1993) found a fair to good correlation (0.75-0.87) between near-IR and falling number and RVA results.

Appendix B

Spectroscopic effect of drying and treatment optimization

Baseline correction was performed as polynomial either second or third order by selecting valleys in the spectrum as shown in figure.

Figure B.1 Baseline correction of a spectrum

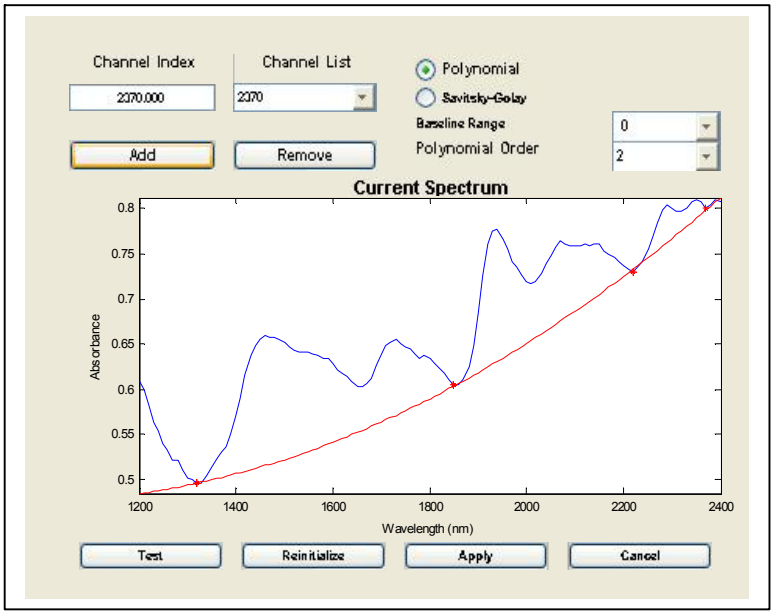

The average peak height at 1940 nm of minimum 100 spectra extracted from germ side of the kernels was calculated for control, 36 hr germinated kernel and germinated and dried kernel. Average peak heights were reported below.

Figure B.2 Baseline corrected spectra averaged for control (blue), sprouted wet (red), sprouted dry (green). Note the water peak in red spectra.

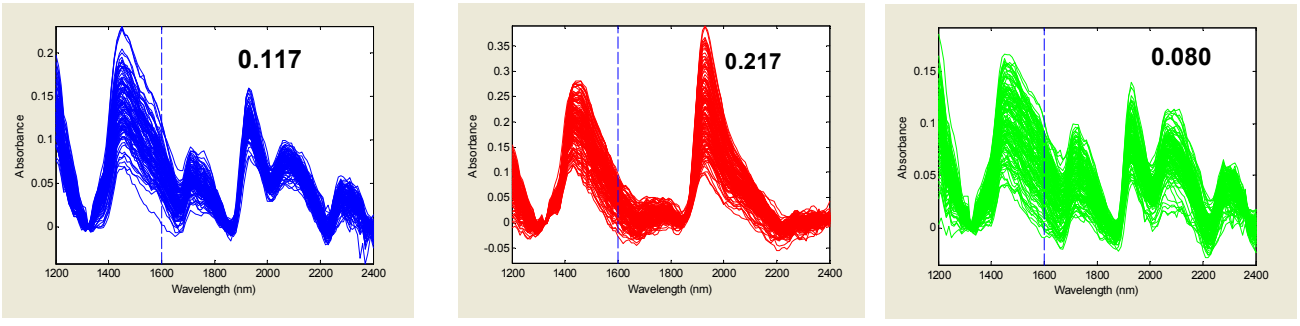

Table B.1 the peak height comparison at 1940 nm for different drying methods.

Drying	**Control (0 hr)**	**36 hr germinated-wet**	**36 hr-germinated dry**
Freeze drying	0.111	0.177	0.091
Forced air (tangent air flow)	0.126	0.192	0.170
Vacuum oven(55ºC 3hr)	0.117	0.217	0.080